Microscale polymeric-based technologies for controlled vaccine delivery

by

Morteza Sarmadi

M.S. in Mechanical Engineering
Sharif University of Technology, 2017

Submitted to the Department of Mechanical Engineering
in partial fulfillment of the requirements for the degree of
Doctor of Philosophy in Mechanical Engineering

at the

MASSACHUSETTS INSTITUTE OF TECHNOLOGY

February 2022

Author……………………………………………………………………………
Department of Mechanical Engineering
Oct 29, 2021

Certified by………………………………………………………………………
Robert S Langer
Institute Professor, MIT
Thesis Supervisor

Accepted by……..…………………………………………………………………
Nicolas Hadjiconstantinou
Professor of Mechanical Engineering
Chairman, Department Committee on Graduate Theses

Microscale polymeric-based technologies for controlled vaccine delivery

by

Morteza Sarmadi

Submitted to the Department of Mechanical Engineering
in February 2022, in Partial Fulfillment of the
Requirements for the Degree of Doctor of Philosophy in
Mechanical Engineering

ABSTRACT

Outbreak of infectious diseases such as COIVD-19 is one of the most critical challenges threatening global health and economy, particularly in developing world. Technologies that can improve delivery, access, effectiveness, and stability of vaccination, as a promising tool against outbreaks, would be strategic tools to potentially save lives and avoid trillions of dollars in financial losses. Our group has been developing such platform technologies for controlled delivery and tracking of vaccines. This thesis investigates further development of these technologies toward clinical translation. In the first part, we investigate a locally injectable microparticle system with a core-shell microstructure made from a novel 3D printing process compatible with biodegradable polymers. These microparticles can be used for delayed, pulsatile release of vaccines, therefore reducing the number of administrations to a single one. We study two translational aspects of core-shell microparticles, namely, injectability, and mechanism of pulsatile release. To study injectability, we use a wide range of tools, namely, multiphysics simulation, experiments, machine learning, and 3D printing to establish a framework for optimal injection of microparticle-based drugs. To study the mechanism of pulsatile release, we integrate various experimental tools with multiphysics simulations to form a model describing the mechanism of degradation and pulsatile release from core-shell particles. In the next phase of this thesis we move forward to a transdermal dissolvable microneedle patch without the need for injections. These microneedle patches can be used to track medical record on patient without the need for expensive healthcare infrastructure--a challenge in developing world. Using extensive computational modeling, we establish a design framework for microneedle devices, widely applicable to any microneedle system. Best trade-off design is then selected for administrations in vivo. We further develop a machine learning algorithm coupled with image processing tools to provide long-term pattern classification capability for encoding information transferred by microneedles to the patient, in an automated and robust fashion. Results of this thesis could be of great interest to development of next generation biomedical devices for controlled vaccine delivery and other applications.

Thesis Supervisor: Robert S. Langer
Title: Institute Professor
Thesis co-Advisor: Ana Jaklenec
Title: Research Scientist

ACKNOWLEDGEMENTS

I would like to thank my thesis advisor and role model Prof. Robert Langer, and my mentor and co-advisor, Dr. Ana Jaklenec for their support, trust, inspiration, patience, and guidance over my PhD studies. I would like to especially thank them for being open-mined and extra supportive, allowing me to pursue areas beyond engineering (e. g. entrepreneurship, business, and medicine) along with my thesis at MIT. I would like to thank all members of Langer lab and Jaklenec group. I have had the opportunity to be guided by several brilliant mentors during my PhD studies, namely, Dr. Adam Behrens, Dr. Kevin McHugh, Dr. Ilin Sadeghi, Dr. Alex Schudel, Dr. Daniel Vlasic, Dr. Robert Farra, and many others. It was a pleasure working with outstanding undergraduate students during my PhD studies, including, Christina Ta, Dominique De Fiesta, Abigail VanLonkhuyzen, Elissa Ito, and Hannah Contreras. Further, I'd like to thank the thesis committee members for continuous feedback and excellent inputs regarding this thesis, namely, Prof. Giovani Traverso and Prof. Rohit Karnik.

I would further like to appreciate all the efforts and dedications by the MIT Department of Mechanical Engineering faculty, staff, and peers for providing such a rigorous and outstanding education. Leslie Regan, Janice McCarthy, Una Sheehan, Saana McDaniel for being always responsive and supportive, from admission to thesis defense. I want to thank all the staff at Langer lab, particularly, Connie Beal, Ilda Thompson, Tracy Hernandez, Schallum Dorleans, and others. I want to thank MIT Division of Comparative Medicine (DCM) facility and staff for support of animal studies in this work. MIT Microsystems Technology Laboratories (MTL) for support of microfabrications in this study along with Harvard Center for Nanosystems (CNS). I want to thank the Biotechnology Resource Center Imaging Facility at Cornell University and Dr. Teresa Porri for supporting and helping with nano-CT imaging studies in this thesis.

I would also like to thank MIT Sloan School of Management, Harvard-MIT Health Sciences and Technology (HST), and Harvard Medical School for allowing me to take courses there. Particularly, I would like to thank the Business Analytics certificate group at MIT Sloan, Healthcare certificate group at MIT Sloan, and graduate education for medical sciences program (GEMS) at HST, for allowing me to enroll and earn graduate certificates along with my PhD program. I would like to thank Gates Foundation for sponsoring the studies performed in this thesis. My former advisors before MIT, Prof. Amir Shamloo (Sharif University of Technology) and Prof. Abolfazl Khalkhali (Iran University of Science and Technology), along with my pre-university teachers.

Most importantly, I would like to thank my family, back in Iran, especially my hero and role model, my mom, Fatemeh Shaaker-Haghighi, my sister, Leila Sarmadi, and my brother, Mahdi Sarmadi for their love, support, and teaching me to constantly fight challenges and never give up.

CONTENTS

FIGURES

TABLES

CHAPTER1

1

INTRODUCTION

1.1 Overview

Despite significant advances in biomedical technologies and access to medical resources worldwide, underimmunization takes the lives of over 1.5 each with majority of them being infants, primarily in developing world [1]. Most notably, recent outbreak of COVID-19 pandemic as a deadly viral infection has tremendously challenged, not only the global healthcare system but also global economy. According to United Nations, it is estimated that the global economy will lose $8.5 trillion in output by mid-2022 due to the COVID-19 pandemic [2]. World Health Organization (WHO) reported that, in 2020, more than 3 million people died globally due to the pandemic [3]. Technologies that can improve delivery, efficacy, and access to immunization, particularly at low-resource settings, therefore play a vitally important role in decreasing human and financial losses caused by infectious diseases and outbreaks. A key aspect of such technologies can be achieved through improved vaccination [4].

Vaccines have been a crucial part in fighting against infectious diseases and outbreaks by training the immune system against viral infections, saving 2-3 million lives annually [6]. Next-generation vaccines such as mRNA vaccines delivered by lipid nanoparticles (LNPs) can be used as a broad platform to provide immunity against variants of viral outbreaks [6]. Despite promising outcomes, storage, delivery, and administration of vaccines suffer from multiple technical complexities, especially in developing world [4-7]. Many vaccines require a specific dosing regimen, and must be administered multiple times (prime and boost shots) to provide adequate immunity [4]. It is reported that over millions of patients, especially in remote areas, do not receive a second dose. As a result, each year about 19.5 million infants remain under-immunized due to lack of access to subsequent vaccination doses [4]. This becomes an even more critical issue in developing countries with poor healthcare infrastructure and databases unable to track patients' medical records, leading to a 30% drop in vaccinations in some cases [8].

This thesis investigates two platform technologies for improved vaccine delivery. Both platforms leverage advanced microfabrication techniques with advanced polymer science, to manufacture microscale tools for a broad range of applications. Both technologies are based on safe and biocompatible polymers. These technologies include 1) injectable core-shell microparticles and 2) transdermal microneedle patches. In the following, a brief summary of each technology and its primary use case is provided.

Core-shell microparticles are hollow microstructure made from biodegradable polymer poly(lactic-co-glycolic acid) [9]. They can be fabricated thanks to a novel 3D printing technology recently developed in our group at our lab [9]. The method termed stamped assembly of StampEd Assembly of polymer Layers (SEAL) enables microfabrication of arrays fabricated from multi-layered microstructures such as core-shell microparticles encapsulating a therapeutic cargo inside the core (**Figure 1.1**) [9]. A key application of these particles is providing single injection vaccine delivery based on a delayed, pulsatile release kinetics (**Figure 1.2**). By fine-tuning the polymer used in fabrication of microparticles, it would be feasible to achieve a wide range of release timepoints (in order of days to months). As a result, by simultaneously injecting multiple types of these particles each mimicking (releasing) a therapeutic dose at subsequent shots, one could provide a single injection vaccine delivery system to simplify multiple shots into a single one. While the platform was originally developed for single-injection pulsatile vaccine, we also demonstrated that the technology could also have applications in cancer immunotherapy [10] while other researchers have demonstrated feasibility of using SEAL to fabricate core-shell microneedles for transdermal vaccine delivery [11]. Unlike traditional emulsion-based microparticles for vaccine delivery (e. g. the work of [12] introducing a single-injection PLGA microsphere system for polio virus vaccine delivery) these particles have a unique microfabricated 3D microstructure allowing the vaccine to be encapsulated inside a cavity called core [9-11]. The core is protected by a polymeric shell which provides the interface with the environment. Despite promising animal data based on this technology [9-11], clinical translation of this technology still faced with challenges. This thesis in particular explores two key aspects of core-shell microparticles, 1) design for injectability and 2) mechanism of pulsatile release.

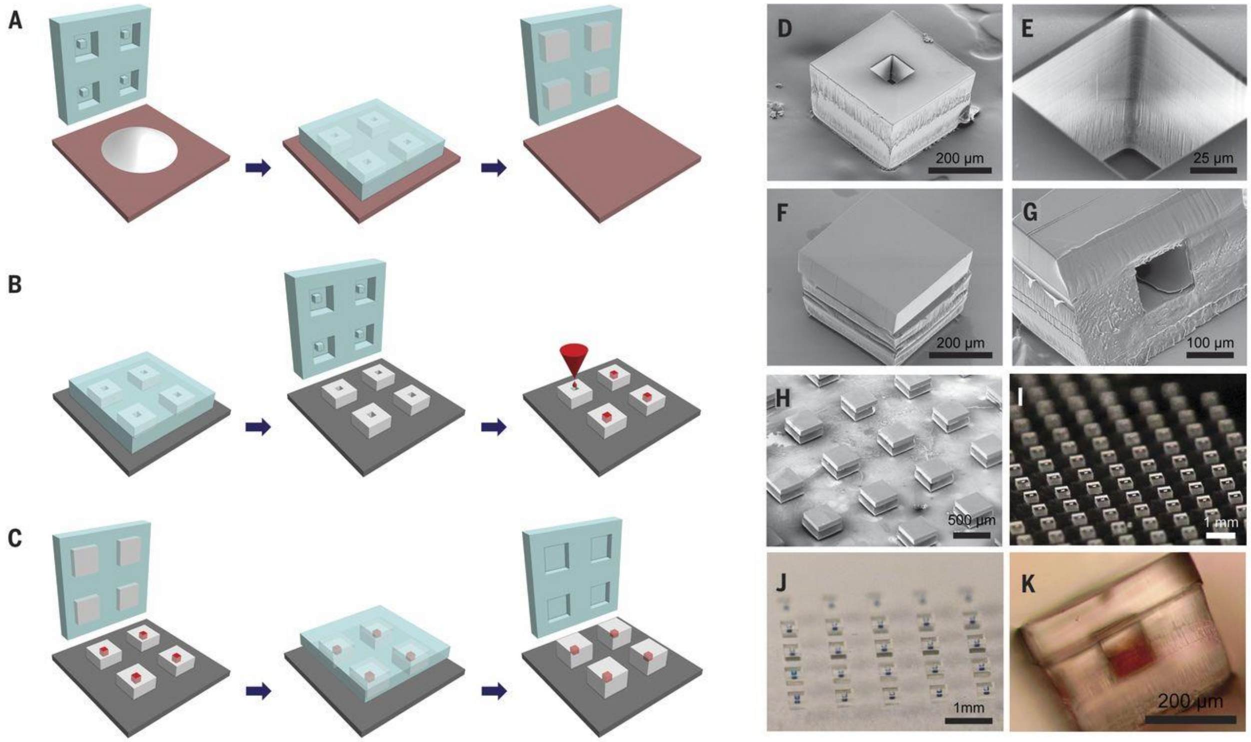

Figure 1.1. SEAL-fabricated controlled-release microparticles. Reprinted from [9]

Particles are fabricated by (A) heating and pressing polymer between a patterned PDMS base mold and a Teflon surface, (B) transferring these bases to a new substrate and filling them with a model drug of interest, then (C) aligning an array of particle caps with drug-filled bases and briefly applying a low amount of heat to sinter the two layers. SEM images of (D) a single particle, (E) the core of a particle, and (F) a sealed particle. (G) A cross section of a single particle and (H) an array of sealed particles. Optical images of (I) an array of bases, (J) an array of filled particles, and (K) a side view of a single filled particle. Reprinted from [9].

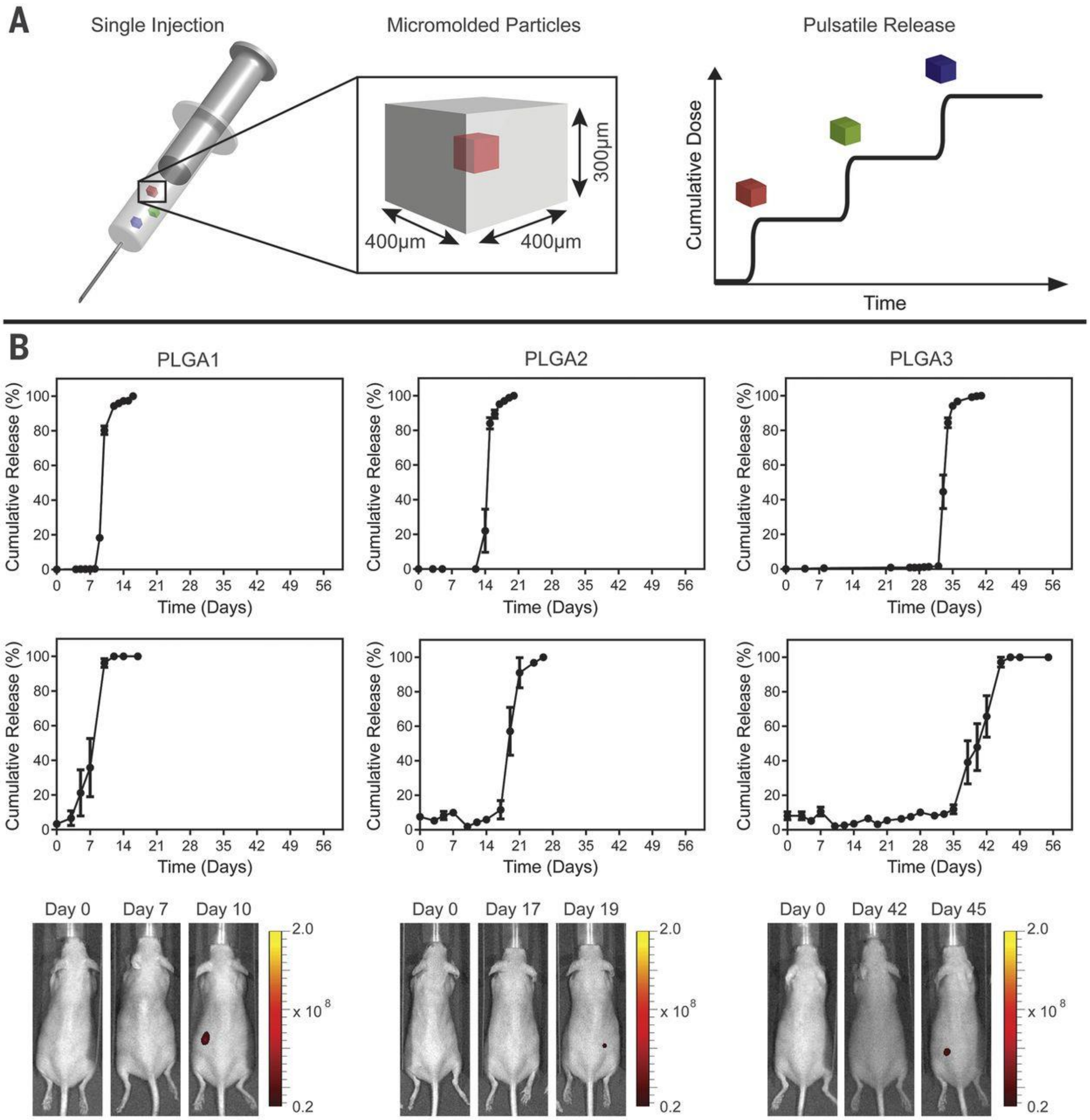

Figure 1.2. Single-injection vaccination concept and release from SEAL-fabricated PLGA microparticles. Reprinted from [9]

(A) Schematic of a syringe containing multiple micromolded particles sufficiently small to pass through an 18-gauge needle that each produce a discrete, delayed pulse of antigen release to mimic current bolus vaccination regimens. (B) In vitro and in vivo pulsatile release of encapsulated Alexa Fluor 680–labeled 10-kD dextran from SEAL-fabricated particles composed of PLGA1, PLGA2, and PLGA3, respectively, from left to right. The top row shows the in vitro cumulative release of fluorescently labeled dextran at 37°C (normalized average, n = 10 particles). Graphs in the second row depict the in vivo cumulative release (normalized average, n = 7 to 10 particles). Note that this yields a broader release curve even though each particle exhibits a sharp pulse because the onset of release can differ slightly in each animal. Error bars indicate the standard error of the mean. The third row shows representative images of mice collected with an in vivo imaging system after injection of a single SEAL-fabricated PLGA particle containing fluorescently labeled dextran. Adapted from [9].

Injectability is a key aspect of design of microparticles. In this thesis, we utilize a wide range of tools namely multiphysics CFD simulations, design of experiment, machine learning, and 3D printing to establish a broad framework for optimal design of not only cubic core-shell particles, but also cylindrical and spherical microparticles. I also introduce a novel syringe geometry that can improve delivery of hard-to-inject particles (including core-shell particles) in vitro and in vivo. I study a wide range of morphology and dimensions and demonstrate that injectability can be predicted by using two dimensionless parameters capturing the effect of material properties as well as geometry.

In the next part of the thesis, the mechanism of release from core-shell microparticles upon degradation at physiological conditions is investigated. Unlike conventional polymeric microspheres, SEAL-fabricated core-shell microparticles represent a unique pulsatile release kinetics (as opposed to sustained). I study the mechanism of release from four perspectives, 1) microstructural evolution, 2) design-function interdependency, 3) evolution in the matrix pH, and 4) computational modeling of deformations. These four aspects enable studying the evolution of microparticles from various perspectives to form a unified model justifying the pulsatile release in view of the polymer degradation. In each section, I utilize extensive experiments based on existing and state-of-the-art tools to characterize the behavior of microparticles over time.

Second part of this thesis explores a transdermal microneedle patch for simultaneous on-patient medical recording and vaccine delivery applications [13]. These microneedle patches can be used to transfer various dye-loaded arrays into the vaccine receiver. Each pattern therefore could work as an invisible barcode providing information on vaccination status (e. g. date of administration, type of vaccine, etc.). I specifically study two aspects, namely: 1) computational modeling and optimization, and 2) development of an image processing algorithm for classification of various microneedle patterns. To model mechanical behavior of microneedles, a computational model based on finite element methods (FEM) is employed to study six objective functions to improve penetration of microneedle to the skin but also maximize deliverable volume to the patient.

Next, I developed an image processing/classification algorithm using machine learning for automated pattern detection. Three patterns were selected for in vivo experiments for delivery of vaccines, at the same time, capturing patterns specific to separate vaccines. The algorithm was used for classification of in vivo images in rats providing an automated method for classification of microneedle patterns that can outperform human detection by naked eyes. The machine-learning based classification technique provided 100% detection accuracy over 6 months, providing a reliable approach toward classification of complicated patterns for long-term medical record tracking [13].

Structure of this thesis is as follows: detailed description for each part is provided in corresponding chapters. The first two chapters study injectability and mechanism of pulsatile release from core-shell microparticles, while the third chapter investigates the modeling and image classification algorithm constructed for vaccine-tracking microneedle patches. Finally, the thesis concludes by providing concluding remarks and proposing future areas of work as the next steps.

CHAPTER

2

INJECTABILITY

This chapter summarizes a key aspect of microparticles used for drug delivery, namely, injectability through hypodermic needles. In this chapter, various computational and experimental tools are used to form a comprehensive framework for design and understating of microparticle injectability. Results of this section can be applied not only to next generation microparticles systems fabricated by SEAL, but also conventional systems such as emulsion-based microspheres. This chapter is reprinted from publication “Modeling, design, and machine learning-based framework for optimal injectability of microparticle-based drug formulations” cited in [14].

2.1 Abstract

Inefficient injection of microparticles through conventional hypodermic needles can impose serious challenges on clinical translation of biopharmaceutical drugs and microparticle-based drug formulations. This study aims to determine the important factors affecting microparticle injectability and establish a predictive framework utilizing computational fluid dynamics, design of experiments and machine learning. A numerical multiphysics model was developed to examine microparticle flow and needle blockage in a syringe-needle system. Using experimental data, a simple empirical mathematical model was introduced. Results from injection experiments were subsequently incorporated into an artificial neural network (ANN) to establish a predictive framework for injectability. Finally, simulations and experimental results contributed to the design of a syringe that maximizes injectability in vitro and in vivo. The custom injection system enabled a six-fold increase in injectability of large microparticles compared to a commercial

syringe. This study highlights the importance of the proposed framework for optimal injection of microparticle-based drugs by parenteral routes.

2.2 Introduction

Microencapsulation-based drug delivery has the potential to dramatically improve drug efficacy, reduce toxicity, contribute to patient compliance and convenience, and even enable new therapies that may otherwise be infeasible to implement [15-17]. Multiple designs and manufacturing techniques have been employed to fabricate microparticles with a range of sizes and functionality (*5-9*), and various release kinetics can be obtained by modulating morphology, material composition, or active perturbation of the drug carrier [9, 18-23]. However, administration of microparticles and biomaterials via an injection holds several challenges [24-30]. Depending on the application, the design of drug delivery systems may prioritize release kinetics, biocompatibility or other factors that may conflict with optimal parameters used in parenteral injection, especially in subcutaneous administration (i.e. needle gauge, particle size, shape, concentration) [24-35]. Injectable microparticle formulations have been translated to the clinic for several controlled release drug applications [35, 36]. There are currently 11 FDA-approved microparticle-based drug formulations on the US market [36]. Additionally, between 1980- 2017, there have been 92 clinical trials globally and 45 clinical trials in the US based on injectable microparticle formulations with a size ranging from 1 to 300 µm [36]. High efficiency transfer of microparticles through injection can play a key factor in delivering the correct dose to the patient and enable successful clinical translation of particulate drug delivery systems [35, 36]. As a result, there is a serious need for development of models and techniques providing insights into injection efficacy of any arbitrary microparticle system [33-37].

Despite significant advances in drug encapsulation, there have been few reports on the investigation of injection efficacy. Hypodermic needles are the most accessible option for injection but can present a challenge for microparticle-based drug delivery, as they can clog or retain particles in the syringe after injection is completed (**Figure 2.1**) [14]. This study aims to establish a comprehensive framework for evaluating the delivery of a broad range of microparticles. We hypothesized that the percentage of microparticles that could be successfully transferred or injected to the patient would be a function of several different design elements (i.e.

microparticle size, needle size, and viscosity of the injection solution). We then demonstrate the use of an integrated approach based on computational fluid dynamics (CFD), data science, and microfabrication techniques to address the issues related to microparticle administration.

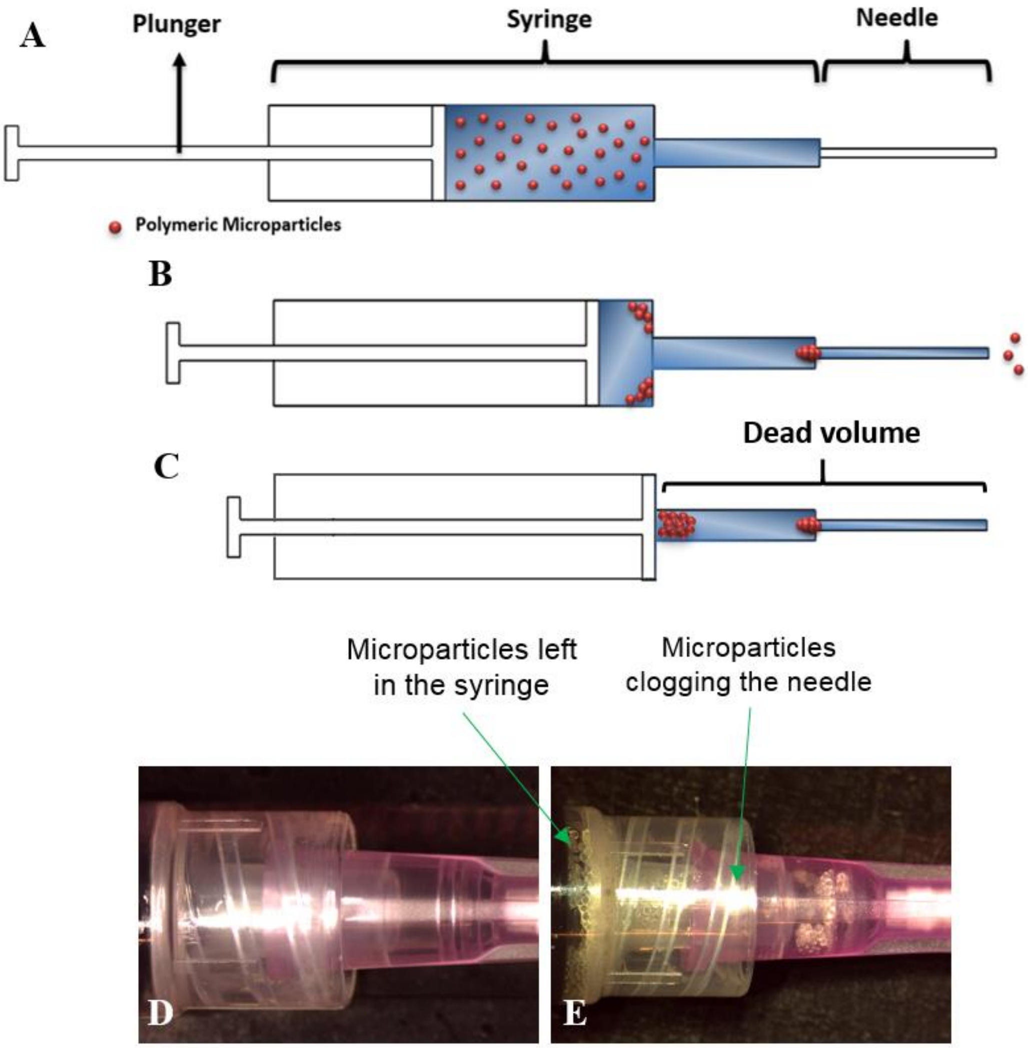

Figure 2.1: Microparticle clog formation as a significant barrier to administration of particulate biopharmaceutical formulations.

Schematic illustration of a typical syringe attached to a hypodermic needle containing a homogenous mixture of polymeric microparticles A) before injection, B) during injection, and C) after injection. The remaining volume of injection solution after full course of plunger in the syringe-needle is called dead space or dead volume. Depending on different design elements, particles are not entirely transferred into the patient through the needle, and they are prone to accumulate in the syringe or clog the needle. An experimental case of microparticle accumulation in the syringe and needle inlet, in D) empty syringe and E) after the full course of plunger displacement. The system illustrated herein is a 3 mL-sized BD® luer lock syringe attached to an 18 G BD® hypodermic needle filled with mixture of water/PLGA. The microparticles are PLGA microspheres with average diameter of 325 μm. Adapted from [14].

To this end, we developed a multiphysics model, coupling CFD with microparticle transport to numerically analyze microparticle injectability in a syringe-needle system. This model was then used to explore the effect of different design elements such as microparticle shape, size, concentration, initial distribution, needle gauge (inner diameter), as well as viscosity of the injection solution on microparticle injectability. Experiments were then conducted to validate the numerical model. Two cycles of testing were performed using design of experiments (DOE) principles to study microparticle injectability and identify the importance of each design parameter. Results were then utilized to perform Taguchi analysis along with variance (ANOVA) to statistically identify the relative contribution of each design parameter. Subsequently, we demonstrated that two dimensionless parameters that utilize variables pertaining to properties of the microparticles, needle and injection solution enable accurate prediction of injectability. An artificial neural network (ANN) was also trained and tested to further predict the injectability results along with the proposed formula. Next, using the resulting numerical and experimental understanding, a custom syringe was designed, manufactured, and tested in-vitro and in-vivo to improve injectability. Results of this study can aid in designing specific delivery systems, predict and prevent microparticle clog formation and potentially improve delivery of microencapsulated drugs and injectable biomaterials.

2.3 Results

2.3.1 Numerical simulations

To gain a numerical perspective on the effect of design parameters (i.e. particle size, shape, concentration, distribution, needle gauge, and solution viscosity) on injectability, computational simulations were performed on a model 3mL-size syringe containing 2mL of the injection solution. These simulations revealed that the maximum flow velocity magnitude reached 5.7 mm/s in the syringe body (barrel) and increased almost 12 times in the syringe tip (70.5 mm/s), and 110 times (627 mm/s) inside the 18G needle (**Figures 2.2 & 2.3**). The velocity magnitude was equal to zero on the wall of syringe-needle as expected for the no slip boundary conditions. The resulting pressure contours also indicated that the syringe wall and plunger experienced the highest pressure value equal to 89 kPa. The pressure gradient generated at the flow inlet (plunger) was the driver for the Poiseuille flow throughout the syringe-needle system, leading to a parabolic velocity profile reaching its maximum value at the centerline. The gauge pressure decreased from its highest value (89 kPa) at the plunger to zero at the needle exit opening to atmosphere (**Figure 2.3**).

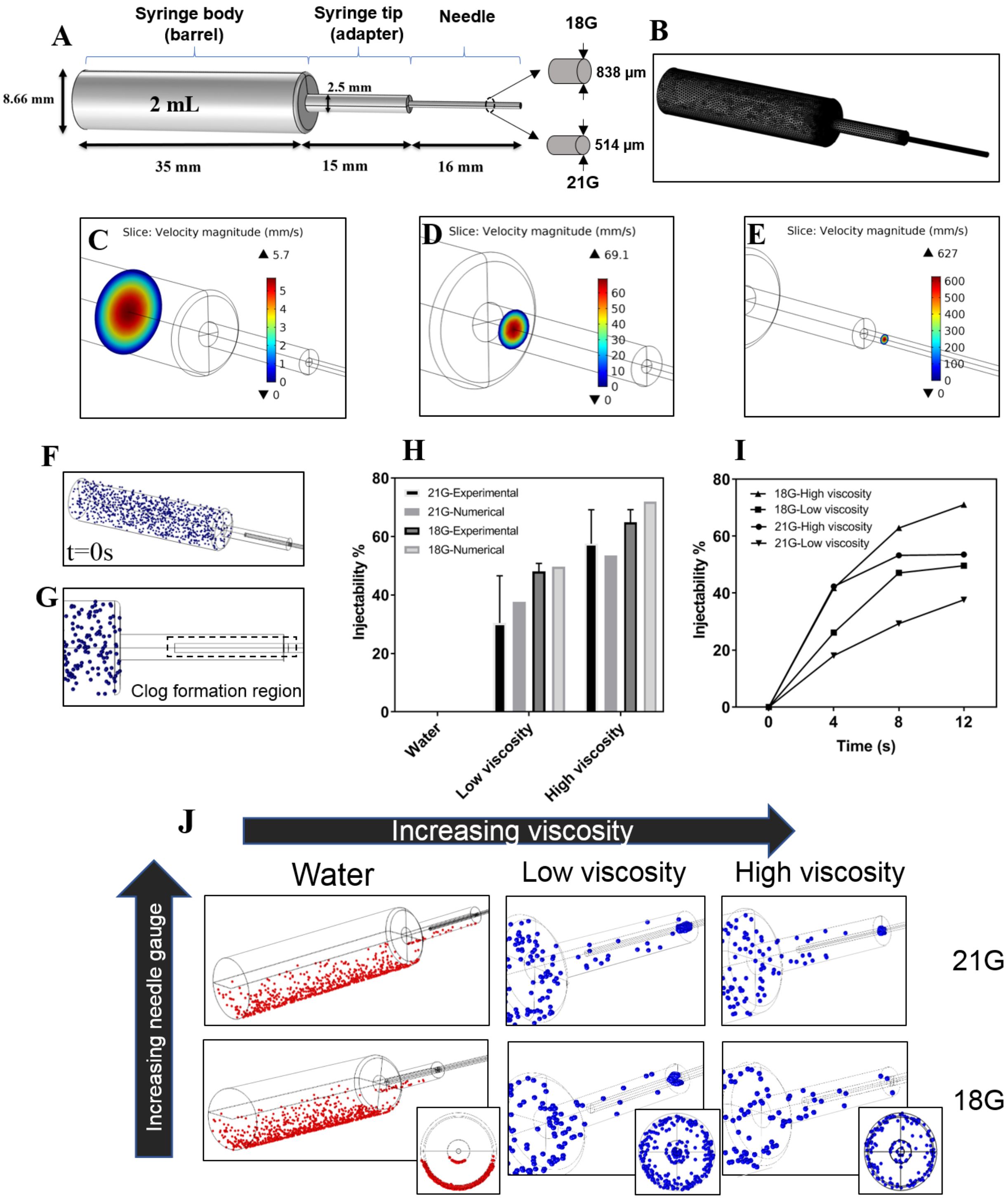

Figure 2.2: Numerical modeling of clog formation in hypodermic syringe-needles.

A) Illustration of the multiphysics numerical model used for simulations corresponding to geometry of a 3mL-sized BD® syringe containing 2 mL of particle-solution mixture. **B)** Meshed geometry, and velocity contours within different locations including **C)** syringe body (barrel), **D)** syringe tip (adapter), and **E)** needle. **F)** Initial position of particles in syringe barrel following random spatial distribution. **G)** Critical location in the syringe-needle defined before the needle inlet to incorporate clog formation domain in the numerical model. **H)** A comparison between numerical and experimental values of injectability. **I)** Injectability decreased over time as the microparticles clogged the needle. **J)** Illustration of particles clogging the needle in the model for different needle gauges and injection solutions. microspheres with an average diameter of 202±6 μm and various concentrations were used in these simulations. Reprinted from [14].

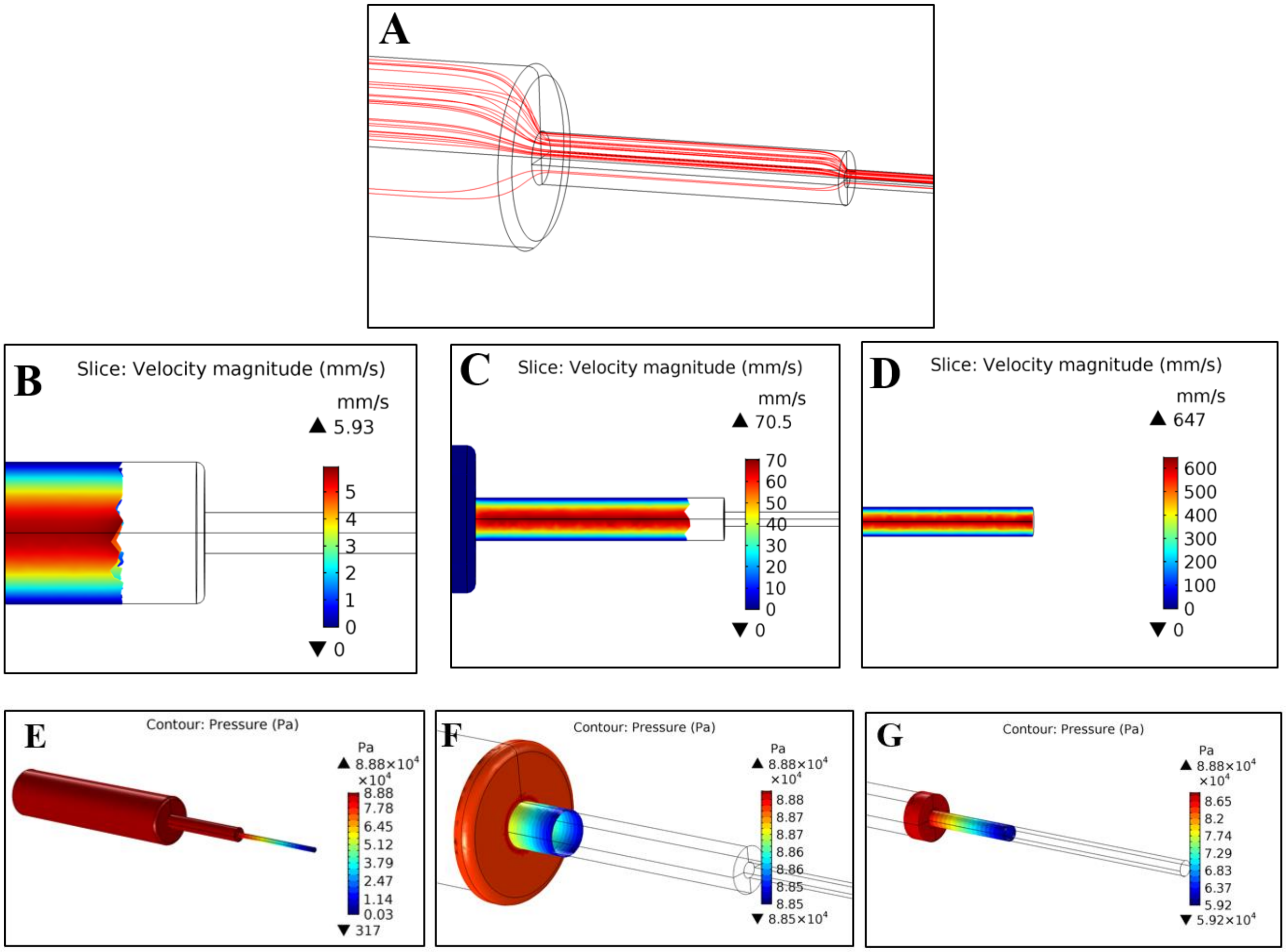

Figure 2.3: Numerical simulations of flow field (velocity and pressure) in a syringe-needle system.

A) Illustration of a set of 50 lines of streamlines in the top half of the syringe geometry. Velocity magnitude profile along different longitudinal cross sections of the syringe-needle geometry in B) barrel, C) transition region from syringe to needle, and D) needle (18G). As the diameter of the model shrinks, velocity magnitude increases by a factor of around ten between each two adjacent regions. Demonstration of pressure contours within different regions of the syringe-needle system in E) syringe body (barrel), F) syringe tip, and G) syringe-needle interface. Pressure is maximum at the plunger and reaches to atmospheric pressure at needle outlet. This pressure gradient serves as the driver for the Poiseuille flow inside the syringe. Adapted from [14].

When using water as the injection solution, particle weight overcame the lateral drag force and the entire particle population sedimented, leading to zero injectability. Within the range studied, viscosity was found to have a major impact on injectability. Injection with the low-viscosity solution (1%MC, μ=0.37 Pa.s at inlet velocity of 2.88 mm/s) significantly enhanced particle transport compared to water, by close to 50% and 40% in 18G, and 21G needles, respectively. Nevertheless, further 2.5 fold increase in concentration of MC in the solution (2.5%MC, μ=5.33 Pa.s at inlet velocity of 2.88 mm/s) led to approximately only 20% of increase in injectability in both needles compared to 1%MC. A solution at even a higher viscosity (5%MC) was found hard to be transferred to the syringe and impractical for injections.

The effects of other parameters (i.e. microparticle concentration, shape and size) on injectability were then evaluated in the context of our model (**Figures 2.4 & 2.5**). Increasing concentration of particles in the solution decreased injectability in both needles (18G and 21G). Injectability of the smaller needle (21G) dropped almost twice the larger needle. Increasing particle concentration was found to be effective only after exceeding a certain concentration threshold (i. e. going from 500 to 800 particles per injection volume). Injectability of solutions loaded with 250 and 500 particles was almost identical, and so was injectability of 800- and 1000-loaded particle solutions.

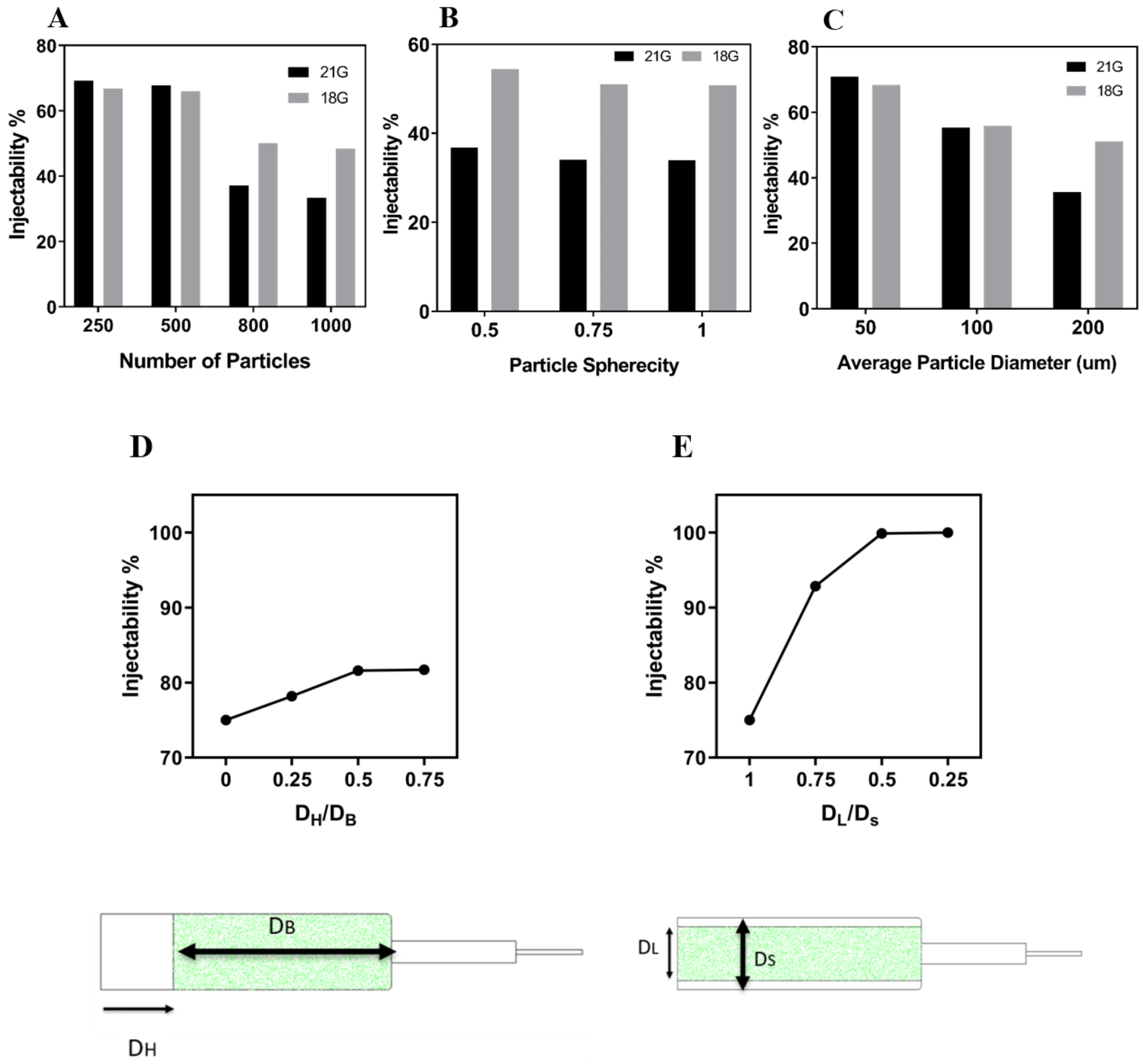

Figure 2.4: Numerical results demonstrating the effect of design parameters important in drug delivery on microparticle injectability.

A) The effect of particle concentration (200 μm in diameter, spherical) on microparticle injectability. B) Effect of particle sphericity (shape) on injectability. C) Injectability of microspheres (1000 particles) as a function of particle size. Effect of initial particle offset (10,000 particles) from D) the plunger, and E) the syringe inner wall on injectability. Particles are illustrated as green dots in the syringe from [14].

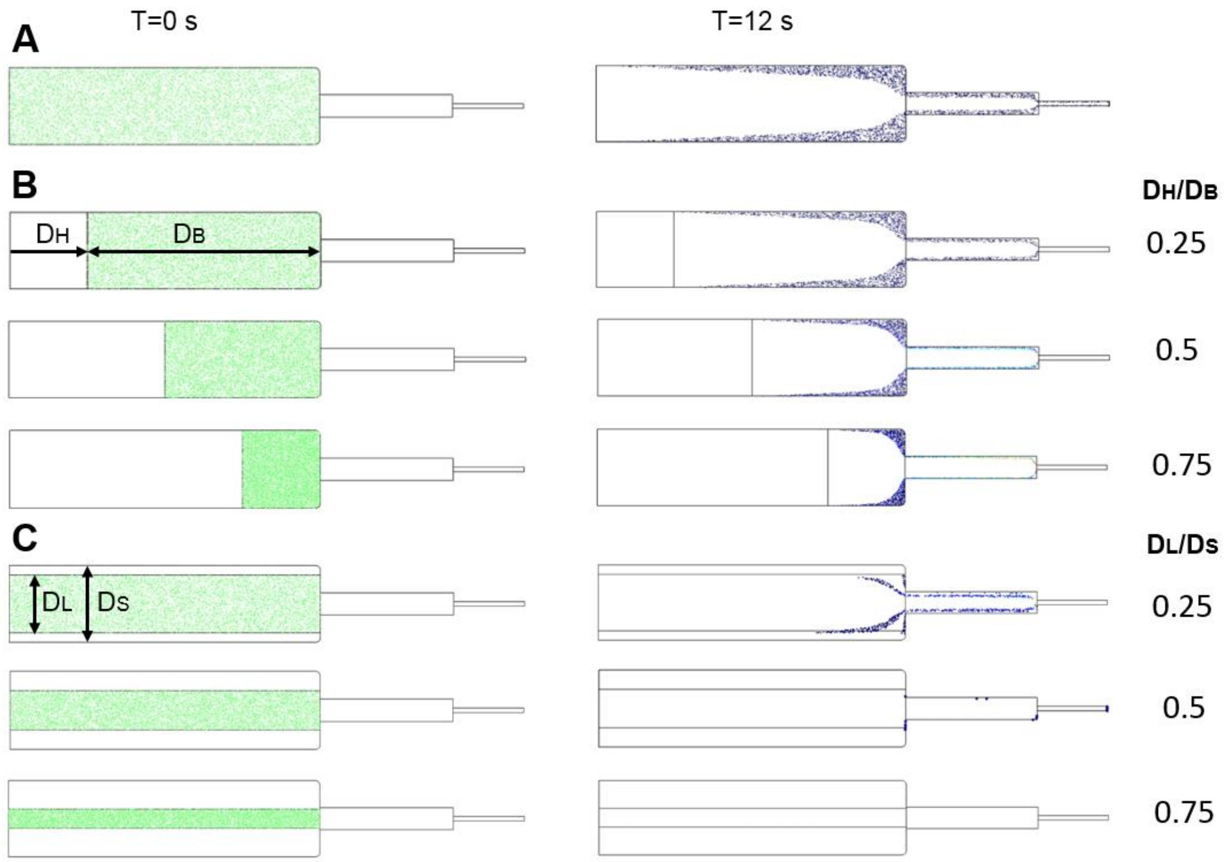

Figure 2.5: Various configurations used to study the effect of initial particle distribution on injectability.

Effect of initial particle position was investigated using 10,000 microspheres with diameter 100±5 µm in a 2D model of the same 3mL-sized BD® syringe already described attached to an 18G needle. Comparison between initial (t=0 s) and final (t=12 s) particle distribution in the system. A) reference configurations are illustrated. Effect of particle initial offset from B) the inlet (plunger) and from C) the inner walls was investigated. Longitudinal offset from the plunger shown in B can be achieved by handling the syringe vertically and letting the particles slightly sediment toward the needle. Transverse offset proposed in *C* can potentially be achieved by lubricating the inner walls with a fluid immiscible with the injection solution. Adapted from [14].

As expected, injectability decreased when larger microparticles were used, and a sharper decrease was observed in a 21G as compared to a 18G needle. In the 21G needle, increasing average particle diameter decreased injectability, such that 200 µm particles yielded an injectability of just 35% compared to 71% for 50 µm particles. However, in the 18G needle, an increase in the average particle diameter from 50 to 200 µm, decreased injectability slightly, from 69% to 52%. These simulations further revealed that injectability depended on the needle size such that 18G needle in most cases had higher particle delivery than 21G needle.

Conversely, particle shape within the range studied did not independently influence the overall injectability.

The results of these simulations also demonstrated that concentrating particles in the centerline of the syringe body (smaller D_L/D_S), closer to the regions with higher velocity magnitude, could enhance injectability (Figs. 3 & S2). Shifting initial position of the particles toward the needle outlet (greater D_H/D_B) also increased injectability, reaching a plateau at D_H/D_B=0.5. In agreement with the 3D model, microparticles were found more likely to accumulate in the stagnation area located in the sharp corners of the syringe body which deviates from streamlines and represent recirculation of the velocity field away from the needle outlet. It was also observed that an offset distance from the wall, captured as the ratio D_L/D_S, represented a more pronounced effect on injectability than the offset distance from the plunger captured by D_H/D_B (**Figures 2.4 & 2.5**)

2.3.2 Experimental evaluation

Words and words and words and Words and words and words and Words and words and words and Words and words and words and Words and words and words and Words and words and words. After implementing a numerical approach, we then sought to experimentally study injectability using a design of experiment (DOE) approach. Injectability of a library of nine different micromolded particles with an approximate size range between 80 to 325 µm was studied with various shapes including cube, cylinder, and sphere (**Figure 2.6 & Table 2.1**). To this end, two sets of experiments based on L_{18} Taguchi orthogonal array were designed and conducted for a 1mL and 3mL syringe with different design factors/levels (**Tables 2.2 & 2.3**).

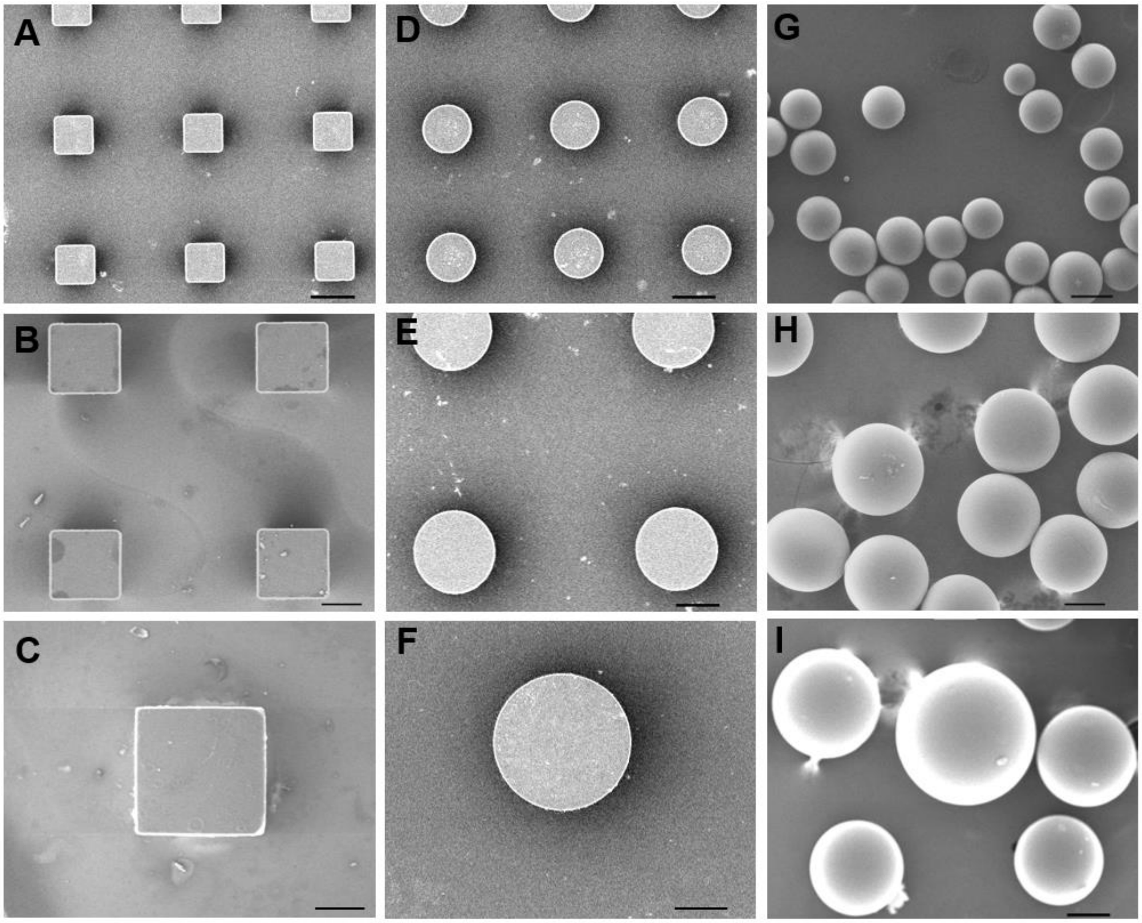

Figure 2.6: SEM Images of microparticles studied in the experiments.

Nine different types of microparticles grouped into different classes of shape and sizes studied in the experiments including **A)** small, **B)** medium, and **C)** large cubic microparticles. Similarly, SEM images of **D)** small, **E)** medium, and **F)** large cylindrical microparticles, and different sizes of spherical microparticles including **G)** small, **H)** medium, and **I)** large microparticles are presented. Scale bar shows 100 µm. Adapted from [14].

Particle shape	**Particle size**					
	Small		**Medium**		**Large**	
	D (μm)	**Volume (μm^3)**	**D (μm)**	**Volume (μm^3)**	**D (μm)**	**Volume (μm^3)**
Cylinder	87	5.2e5	174	4.1e6	261	1.4e7
Cube	81	5.3e5	162	4.3e6	241	1.4e7
Sphere	100	5.2e5	202	4.2e6	325	1.8e7

Table 2.1: Details of the particle dimensions used in the experiments.

All particles were made from PLGA (Resomer® RG 502H, L:G=50:50). Cylindrical particles have an aspect ratio of 1. Parameter *D* represents diameter of the cylinders, diameter of spheres and the edge of the cubes. Numbers represent the average dimensions. Particle dimensions were selected to yield an identical volume for different shapes belonging to a given size.

Design parameter	**DOE1 design levels**	**DOE2 design levels**
Solution viscosity	Water, Low, High	Low (not a variable)
Particle size	Small, Medium, Large	Small, Medium, Large
Needle gauge	16G, 18G, 21G	22G, 25G, 30G
Particle concentration	Low, High	Low, High
Particle shape	Sphere, Cylinder, Cube	Sphere, Cylinder, Cube

Table 2.2: Description of the design levels for each design factor in the DOEs.

Low and high concentration levels refer to an average of approximately 35, and 120 particles per 0.3 mL of the injection solution, respectively. Low, and high viscosity injection solutions correspond to 1%MC, and 2.5% MC solutions, respectively. Adapted from [14].

DOE #	Exp. #	Design factors					1 mL syringe		3 mL syringe	
		Particle number concentration	Viscosity (solution)	Needle gauge	Particle shape	Particle size	Particle concentration	Injectability (%)	Particle concentration	Injectability (%)
1	1	Low	Water	21G	Sphere	Small	36 ± 9	0 ± 0.00	34 ± 5	0 ± 0.00
	2	Low	Water	18G	Cube	Medium	34 ± 4	0 ± 0.00	33± 8	0 ± 0.00
	3	Low	Water	16G	Cylinder	Large	44 ± 4	0 ± 0.00	42 ± 11	0 ± 0.00
	4	Low	Low	21G	Sphere	Medium	33 ± 4	85.25 ± 34.66	21 ± 13	75.93 ± 13.34
	5	Low	Low	18G	Cube	Large	37 ± 8	73.59 ± 8.00	38 ±11	35.36 ± 3.29
	6	Low	Low	16G	Cylinder	Small	31 ± 5	79.69 ± 8.40	33 ± 3	87.55 ± 6.97
	7	Low	High	21G	Cube	Small	45 ± 9	81.72± 2.12	32 ± 6	90.44 ± 1.61
	8	Low	High	18G	Cylinder	Medium	34 ± 13	82.46 ± 1.40	33 ± 9	69.30 ± 9.07
	9	Low	High	16G	Sphere	Large	40 ± 9	72.40 ± 14.46	40 ± 9	79.29 ± 16.82
	10	High	Water	21G	Cylinder	Large	103 ± 8	0 ± 0.00	115 ± 14	0 ± 0.00
	11	High	Water	18G	Sphere	Small	114 ± 40	0 ± 0.00	116 ± 20	0 ± 0.00
	12	High	Water	16G	Cube	Medium	110 ± 33	0 ± 0.00	118 ± 17	0 ± 0.00
	13	High	Low	21G	Cube	Large	113 ± 64	51.56 ± 13.58	113 ± 29	21.47 ± 6.60
	14	High	Low	18G	Cylinder	Small	172 ± 40	95.66 ± 2.87	147 ± 10	87.56 ± 34.66
	15	High	Low	16G	Sphere	Medium	170 ± 33	73.80 ± 4.69	159 ± 16	50.85 ± 7.14
	16	High	High	21G	Cylinder	Medium	157 ± 19	88.75 ± 5.51	105 ± 15	67.82 ± 5.77
	17	High	High	18G	Sphere	Large	130 ± 18	77.40 ± 9.05	100 ± 13	64.36 ± 12.06
	18	High	High	16G	Cube	Small	163 ± 54	81.33 ± 7.55	150 ± 28	82.76 ± 7.50
2	1	Low	Low	22G	Cube	Small	39 ± 4	86.91 ± 7.37	38 ± 14	86.19 ± 7.37
	2	Low	Low	25G	Cube	Medium	39 ± 3	46.57 ± 2.60	23 ± 7	20.85 ± 2.95
	3	Low	Low	30G	Cube	Large	29 ± 2	5.35 ± 4.18	29 ± 6	0.00 ± 0.00
	4	Low	Low	22G	Cylinder	Small	37 ± 5	91.17 ± 1.73	31 ± 7	73.24 ± 12.61
	5	Low	Low	25G	Cylinder	Medium	31 ± 3	74.80 ± 1.66	25 ± 12	71.13 ± 8.16
	6	Low	Low	30G	Cylinder	Large	35 ± 7	0.00 ± 0.00	40 ± 7	0.00 ± 0.00
	7	Low	Low	25G	Sphere	Small	32 ± 7	75.09 ± 13.62	42 ± 7	88.07 ± 5.77
	8	Low	Low	30G	Sphere	Medium	35 ± 12	2.40 ± 2.15	31 ± 8	0.00 ± 0.00
	9	Low	Low	22G	Sphere	Large	43 ± 4	63.49 ± 11.18	30 ± 6	50.39 ± 9.80
	10	High	Low	30G	Cube	Small	102 ± 13	1.09 ± 1.88	109 ± 12	0.00 ± 0.00
	11	High	Low	22G	Cube	Medium	107 ± 4	72.81 ± 6.28	115 ± 32	80.90 ± 6.95
	12	High	Low	25G	Cube	Large	99 ± 3	24.47 ± 5.30	96 ± 31	1.47 ± 2.55
	13	High	Low	25G	Cylinder	Small	123 ± 14	84.27 ± 8.94	136 ± 20	87.59 ± 2.62
	14	High	Low	30G	Cylinder	Medium	118 ± 21	0.61 ± 0.54	115 ± 32	0.00 ± 0.00

	15	High	Low	22G	Cylinder	Large	105 ± 19	37.83 ± 19.63	143 ± 26	7.48 ± 3.82
	16	High	Low	30G	Sphere	Small	118 ± 21	80.38 ± 10.40	106 ± 17	28.17 ± 22.64
	17	High	Low	22G	Sphere	Medium	106 ± 20	82.79 ± 4.63	119 ± 46	78.76 ± 8.97
	18	High	Low	25G	Sphere	Large	125 ± 12	3.89 ± 2.91	122 ± 13	0.00 ± 0.00

Table 2.3: Detailed information of experiments.

In total, 72 different type of injection experiments (n=3 or 4) were performed to study microparticle injectability through different hypodermic-needle systems. Particle concentration represents the number of particles per 300 µL of the injection solution, from [14].

The injectability values obtained from the DOEs are presented in **Figure 2.7** and **Table 2.3**. In DOE1, the mean of injectability reached an approximate plateau at the low viscosity level (1%MC). Further, while injection using a low viscosity solution instead of water improved injectability by more than 50%, the difference between result of low and high viscosity solutions (1%MC, and 2.5%MC) was considerably less pronounced (less than 10%). In accordance with simulation results, increasing size of the microparticles decreased injectability for both syringe sizes studied. As also predicted by the simulations, the effect of microparticle size was notably more influential in injections using smaller needles (i. e. DOE2), as evident by a sharper decrease in injectability as a function of particle size.

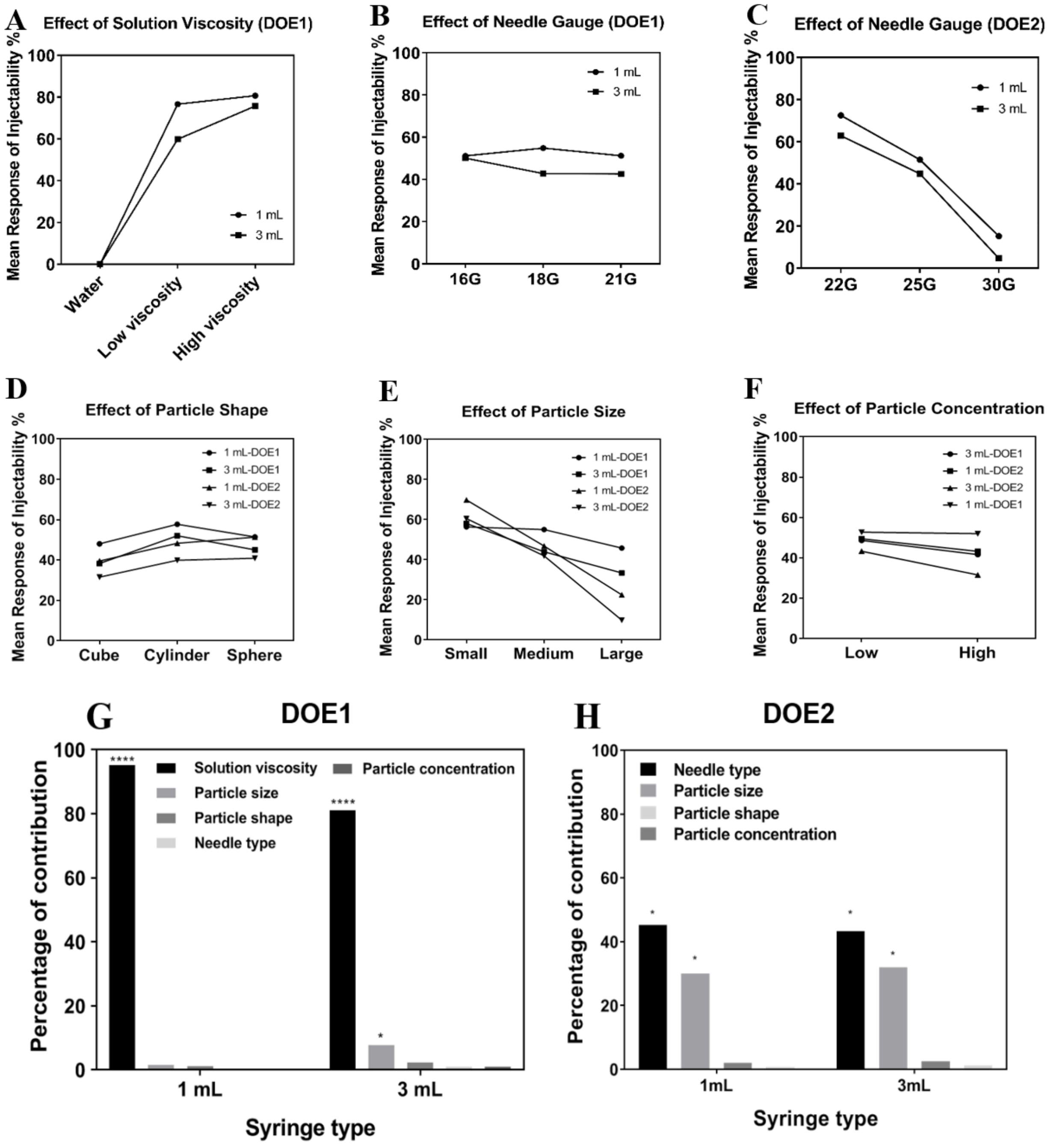

Figure 2.7: Experimental study on effect of different parameters on injectability.

Mean response of injectability obtained from Taguchi analysis indicating the effect of the design parameters including A) viscosity, B) needle gauge (DOE1), C) needle gauge (DOE2), D) particle shape, E) particle size, and F) particle concentration. ANOVA results demonstrating the comparative significance and ranking of each of the design parameters studied for 1 mL and 3 mL syringes. (**** $p<0.0001$ & * $p<0.05$). G) From DOE1, solution viscosity was identified as the most important factor, and H) in DOE2, needle size and particle size were the two dominant design parameters. Adapted from [14].

A similar trend was observed for the effect of needle size, such that decreasing needle size decreased injectability in agreement with the numerical results. Similar to particle size, the effect of the needle size was more pronounced in the context of the narrower needles employed in DOE2 (needle inner diameters from 0.1 to 0.5 mm) compared to DOE1 (needle inner dimeters from 0.5 to 1 mm). It was also observed that increasing particle concentration did not have a statistically significant effect within the range studied (approximately 30 to 150 particles in 300 μL). As predicted by the simulations, particle shape did not have a major effect on injectability. These trends were consistent between both syringe sizes.

Next, we employed ANOVA based on a general linear model to identify the relative importance of each design factor on injectability (**Figure 2.7**). Viscosity was found to be the most important parameter based on DOE1, offering a contribution percentage as high as 90% ($P<0.0001$). By excluding viscosity as a variable and using narrower needles in DOE2, particle size and needle gauge became the two dominant design factors ($p<0.05$), whereas the effect of particle concentration and shape was comparatively negligible.

2.3.3 Model development

Two dimensionless parameters (π_1 and π_2) were found to successfully predict the chance and range of injectability for various syringe-needle systems. The first dimensionless parameter (π_1) was based on material properties and concentration of the particles, and viscosity of the injection solution. The second dimensionless parameter represented the ratio of the needle diameter divided by the greatest dimension of the particle (π_2). The calculated injectability as a function of π_1 and π_2 was plotted to capture the parameter space necessary to yield high injectability region (**Figure 2.8**).

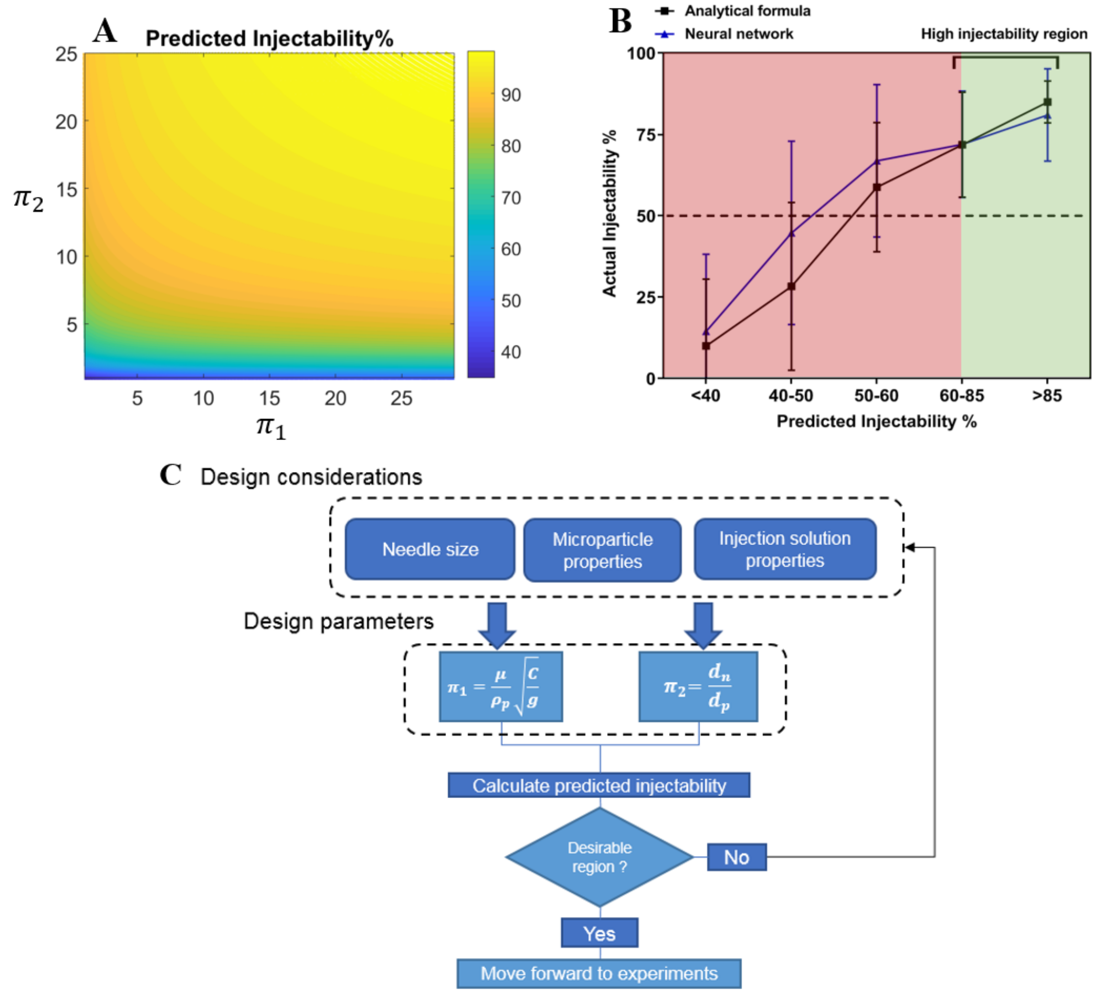

Figure 2.8: Prediction of injectability for various syringe-needle systems.

A) The plot contour demonstrates predicted injectability as a function of the two non-dimensional parameters calculated by Eq. 2-4. B) The relationship between actual microparticle injectability from the experiments, and the predicted injectability calculated by the formula and ANN. High injectability region was assumed where the lowest bound of actual injectability (average subtracted by standard deviation) was greater than 50%. Error bars show standard deviation. C) Proposed flowchart demonstrating potential application of the proposed predictive tools for design of high injectability drug delivery microparticles. Adapted from [14].

A predicted injectability (denoted by *f*) of more than 60%, as the critical threshold, provided an actual injectability of at least 50%. The high injectability margin was further divided to two regions based on the predicted injectability. Accordingly, the first case corresponded to a value of *f* equal to 60-85% yielding an actual injectability of 72% on average. Second, an *f* value of 85% provided an average actual injectability of 85%. The criteria for choosing the high injectability margin was based on the needle dead volume (or dead-space). Based on the reported values in the literature, we considered the dead volume to be approximately between 25-30% for the injected volume in this study [34]. An additional 22 experiments (n=3) including both 1 mL and 3 mL syringes using microspheres made from polystyrene, PMMA, and PLGA (**Table 2.4**) were also performed to further validate the prediction formula. A comparison of actual injectability versus predicted injectability, *f*, is also presented in **Figure 2.8**. Pearson correlation coefficients of 0.84 and 0.79 were found between predicted and actual injectability in the sets of the DOEs and validation experiments, respectively. This finding suggests strong correlation between the predicted and actual injectability values.

Exp. #	**Syringe size**	**Needle type**	**Particle material**	**Average nominal particle diameter (μm)**	**Particle concentration**	**Predicted injectability (%)**	**Actual injectability (%)**
1	1 mL	25G	PLGA	100	333 ± 42	67.42	55.07 ± 9.89
2	1 mL	31G	PLGA	100	302 ± 45	45.52	53.50 ± 2.39
3	1 mL	33G	PLGA	100	328 ± 40	37.02	0.00 ± 0.00
4	1 mL	26G	Polystyrene	100	415 ± 23	68.16	71.52 ± 2.43
5	1 mL	31G	Polystyrene	100	473 ± 40	45.83	54.79 ±3.36
6	1 mL	33G	Polystyrene	100	350 ± 30	37.11	0.00 ± 0.00
7	1 mL	18G	PMMA	400	70 ± 30	59.65	67.38 ± 15.86
8	1 mL	19G	PMMA	400	78 ± 21	53.65	41.71 ± 25.87
9	1 mL	20G	PMMA	400	40 ± 12	48.48	27.26 ± 14.59
10	1 mL	33G	PLGA	50	413 ± 153	62.39	68.89 ± 13.91
11	3 mL	33G	PLGA	50	7773 ± 1379	63.62	64.36 ± 5.21
12	3 mL	25G	PLGA	100	920 ± 288	68.45	54.99 ± 3.95
13	3 mL	31G	PLGA	100	153 ± 31	45.10	16.90 ± 5.12
14	3 mL	33G	PLGA	100	794 ± 282	37.11	0.52 ± 49
15	3 mL	33G	Polystyrene	100	638 ± 51	37.09	0.00 ± 0.00
16	3 mL	26G	Polystyrene	100	1868 ± 51	69.20	73.91 ± 7.53
17	3 mL	26G	Polystyrene	100	6577 ± 1877	69.50	81.90 ± 6.42
18	3 mL	21G	PLGA	400	115 ± 12	43.56	41.82 ± 26.26
19	3 mL	19G	PLGA	500	77 ± 9	45.64	80.79 ± 13.30
20	3 mL	22G	PLGA	500	31 ± 9	23.81	5.46 ± 1.48
21	3 mL	20G	PLGA	500	23 ± 1	39.41	12.63 ± 8.14
22	3 mL	22G	PLGA	400	128 ± 41	34.72	40.73 ± 11.92

Table 2.4: Details of validation experiments.

Results of the 22 validation experiments (n=3) conducted to evaluate predication accuracy of the formula in Eq. 2-4. All particles in these experiments are spherical. Particle concentration refers to the number of particles in 300 µL of the injection solution.

Along with the proposed formula, an ANN was also trained for predicting microparticle injectability. The best training result corresponding to the lowest mean square error between predicted and actual injectability values was achieved at epoch 63 (**Figure 2.9**). The trained ANN improved the overall R^2 value to 0.88 for entire data population and to 0.90 for the testing data subset (**Figure 2.9**). Mapping of actual injectability to the predicted values obtained from the ANN predictions was also compared with the values from the formula (**Figure 2.8**). As shown, the simplified formula can provide reasonable accuracy resembling the results provided by the ANN. Both methods suggested that a predicted value of greater than 60% could be used as a high injectability margin, yielding an actual injectability of at least 50%. The workflow for using the proposed predictive injectability tools is also illustrated in **Figure 2.8**. A combined utilization of the proposed ANN and the formula can be used to predict injectability for a given microparticle morphology, and only proceed to experiments where the predicted injectability falls within high injectability region ($f \geq 60\%$).

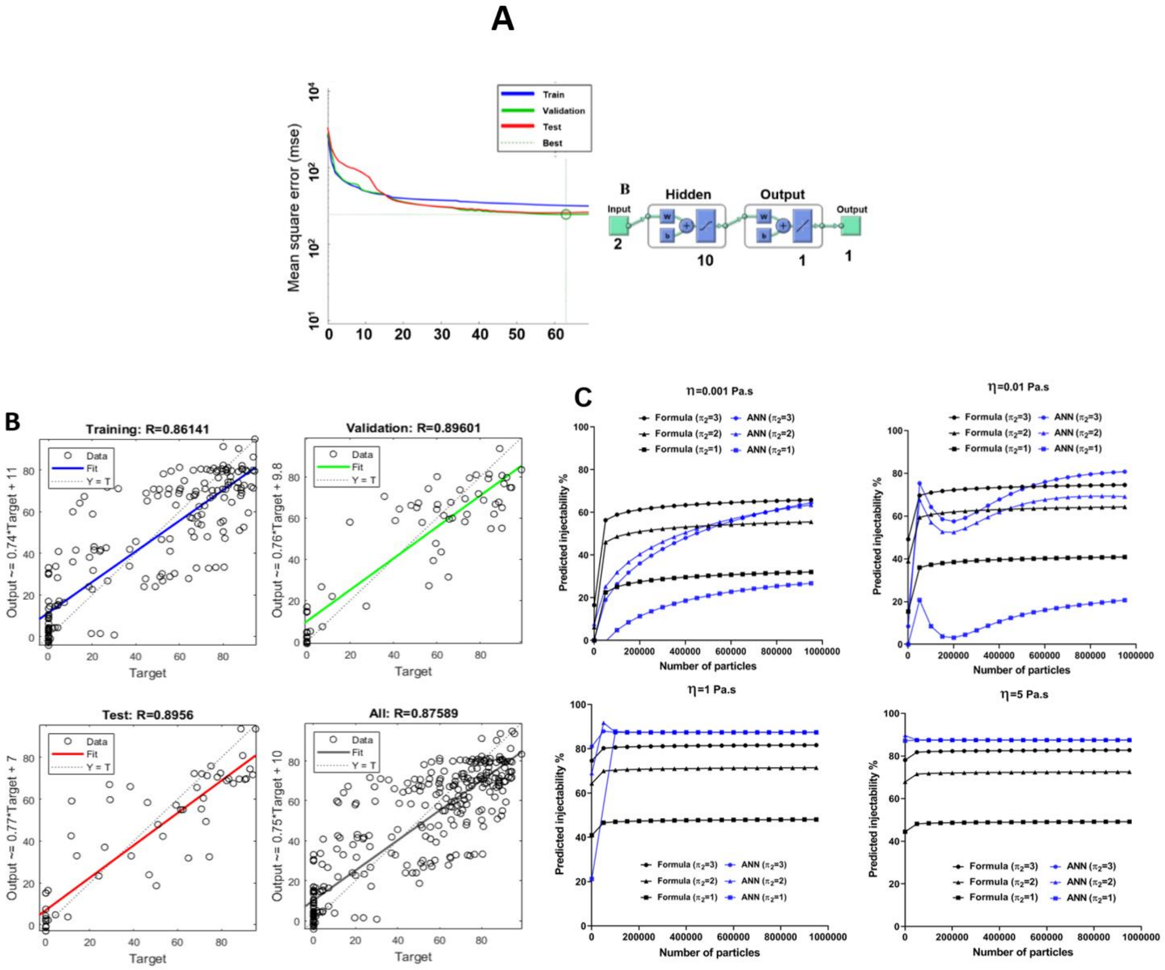

Figure 2.9. Detailed graphs on the training and testing of the predictive neural network.

A) Mean square error plot of predicted injectability obtained by the neural network as a function of epoch number. The best performance was achieved at epoch 63. Structure of the network was composed of 10 hidden layers, incorporating the two dimensionless parameters introduced as the input and predicted injectability as the output. Training was performed using Levenberg-Marquardt backpropagation algorithm in MATLAB® Deep Learning Toolbox. B) Regression fit results for training, validation and testing data subsets. C) Effect of different design parameters on predicted injectability calculated from the developed ANN and the formula. In some cases, before convergence, ANN provided injectability values above 100% that were modified to 100. Adapted from [14].

In line with numerical and experimental results, increasing viscosity from 0.001 to 1 Pa.s, considerably improved predicted injectability in both proposed formula and the ANN. Interestingly, increasing viscosity from 1 to 5 Pa.s did not have the same impact which was also observed in the simulations and experiments. After converging to a certain value, particle concentration was found not to impose any major effect on predicted injectability for the present laminar regime. Further, as expected, increasing the ratio of needle size to particle size (i. e. greater π_2) served to increase the predicted injectability.

2.3.4 Design of a new syringe for improved injectability

We sought to employ the resulting understanding of microparticle injectability to design and test a customized syringe design optimized for enhanced microparticle injectability. We studied injectability of cubic hollow and solid microparticles recently introduced as a promising platform for single-injection vaccine delivery, as the focus of this thesis [9]. The results of the optimization and manufacturing of the proposed syringe, as well as the workflow summarizing these steps including numerical optimization are provided in **Figures 2.10** & **2.11**.

In view of manufacturability and needle attachment considerations, a design ranked in the top 35% out of 500 designs, numerically studied, was selected for a more comprehensive detailed design in Solid Works ® and manufacturing (see supplemental file for more details regarding optimization procedure). In the detailed design step, we modified the typical geometry of a syringe and adopted a nozzle-shaped geometry in the syringe tip. This design was based on two interconnected nozzle geometries to increase velocity magnitude (hence drag force on particles) at each nozzle outlet throughout the syringe tip. It was found that two design parameters had a major impact on microparticle transport: slope of the syringe wall recapitulated by the angle θ and the distance between barrel and syringe exit denoted as L. The optimized syringe design provided a statistically significant improvement in the microparticle injectability, compared to a similar 3 mL BD® syringe as the control group. The custom syringe increased average injectability by 10-36% showing greater improvement in injectability of particles with larger dimensions compared to a commercial syringe. A 1 mL version of the optimum 3 mL custom syringe was further manufactured and employed for subcutaneous in vivo injection of cubic microparticles, as an example, to be covered next.

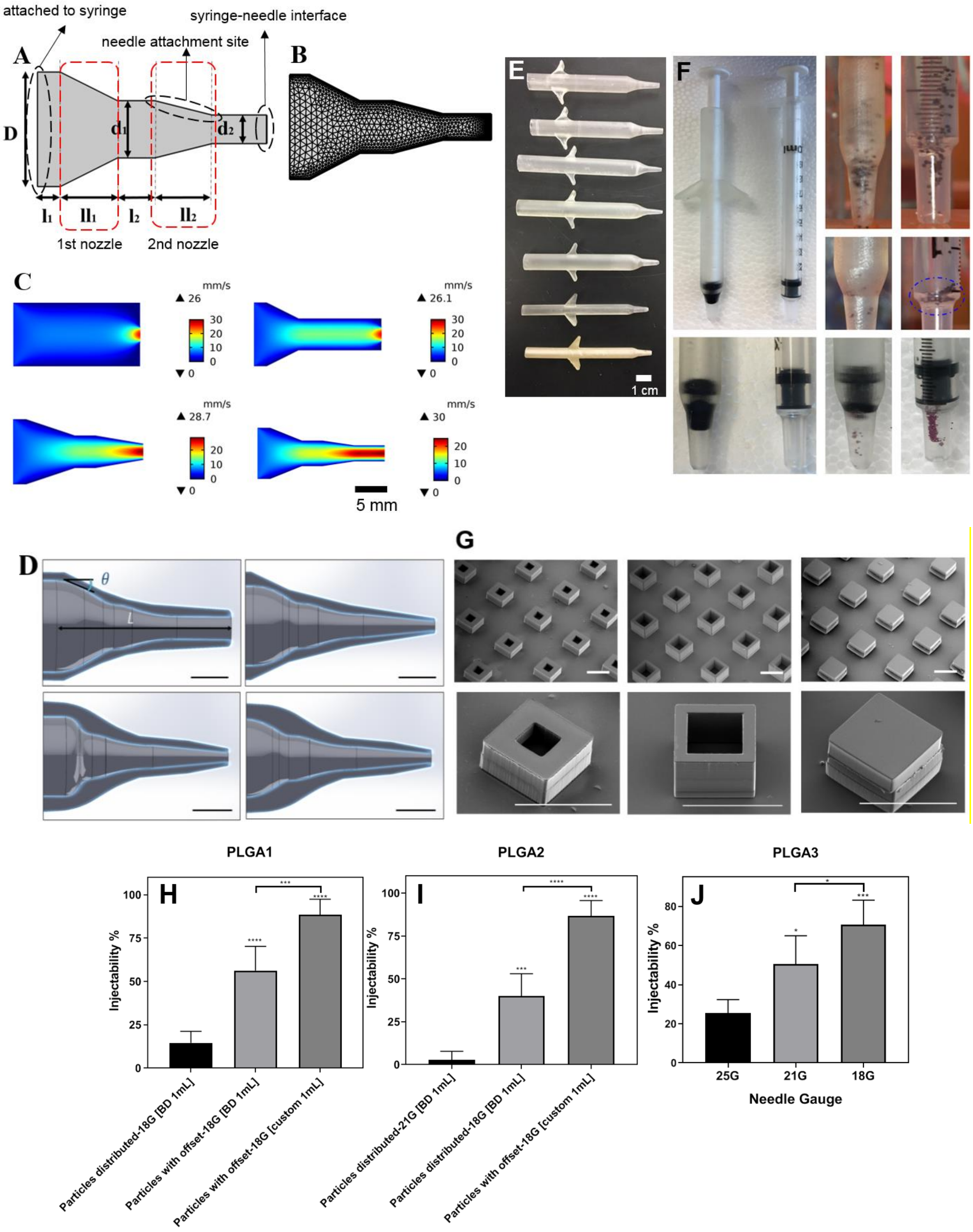
A
attached to syringe
needle attachment site
syringe-needle interface
D
d1
d2
l1
ll1
l2
ll2
1st nozzle
2nd nozzle
B
C
mm/s
▲ 26
▼ 0
▲ 26.1
▲ 28.7
▲ 30
30
20
10
0
5 mm
E
1 cm
F
D
θ
L
G
PLGA1
PLGA2
PLGA3
H
I
J
Injectability %
100
75
50
25
0
80
60
40
20
***
****
*
Particles distributed-18G [BD 1mL]
Particles with offset-18G [BD 1mL]
Particles with offset-18G [custom 1mL]
Particles distributed-21G [BD 1mL]
Particles distributed-18G [BD 1mL]
Particles with offset-18G [custom 1mL]
25G
21G
18G
Needle Gauge

Figure 2.10: Design, optimization, manufacturing, and in vivo testing of a customized syringe made for high injectability applications.

A) Design parameters considered in the numerical modeling and optimization of the syringe tip (adapter) based on two interconnected nozzles. B) Meshed geometry of the syringe tip C) Velocity magnitude contour in some of the designs as the criterion for optimization. D) Examples of detailed design of the syringe tip profile in Solid Works ® based on different design parameters such as θ and L. Scale bar shows 5 mm. E) Different 3mL size syringes (top five syringes) were manufactured by SLA 3D printing to optimize needle attachment, decrease dead volume, and improve injectability in vitro. A 1 mL version of the optimum design ($\theta \sim 25°$) based on in vitro injections was further manufactured for in vivo injections (two bottom designs). F) Comparison between 1mL version of the proposed syringe and a comparable commercial syringe. Unlike in the proposed design, particles were observed to accumulate in sharp corners in the barrel of the commercial syringe. The proposed design also demonstrated less dead volume accompanied by less particle waste. More details can be found in the supplemental file. G) SEM images of PLGA1-fabricated core-shell microparticles, a recently developed platform for single-injection vaccination. Different core geometries but the same exterior size (400×400×300 um) can be achieved by modifying the manufacturing steps. Different configurations of the sealed and unsealed base layer in high and low magnifications are demonstrated. Scale bar shows 500 µm. A full description of the manufacturing steps can be found in (*5*). H-J) In vivo subcutaneous injection results (n=5) using different strategies to enhance microparticle injectability (* $p<0.05$, ***$p<0.001$, **** $p< 0.0001$). Particles were initially loaded into the syringe either randomly distributed (noted as “distributed”) or with a certain offset from the plunger (noted as “with offset”). The term inside the brackets indicates type of the syringe, either the commercial or the proposed syringe. PLGA1, PLGA2, and PLGA3 refer to cubic particles with a dimension of 400×400×300 μm^3, 350×350×330 μm^3, and 162×162×162 μm^3 made from PLGA (Resomer® 502H), respectively. PLGA1 has a cubic internal core of 200×200×100 μm^3, while PLGA 2 and PLGA 3 are solid (i.e. non-hollow). Adapted from [14].

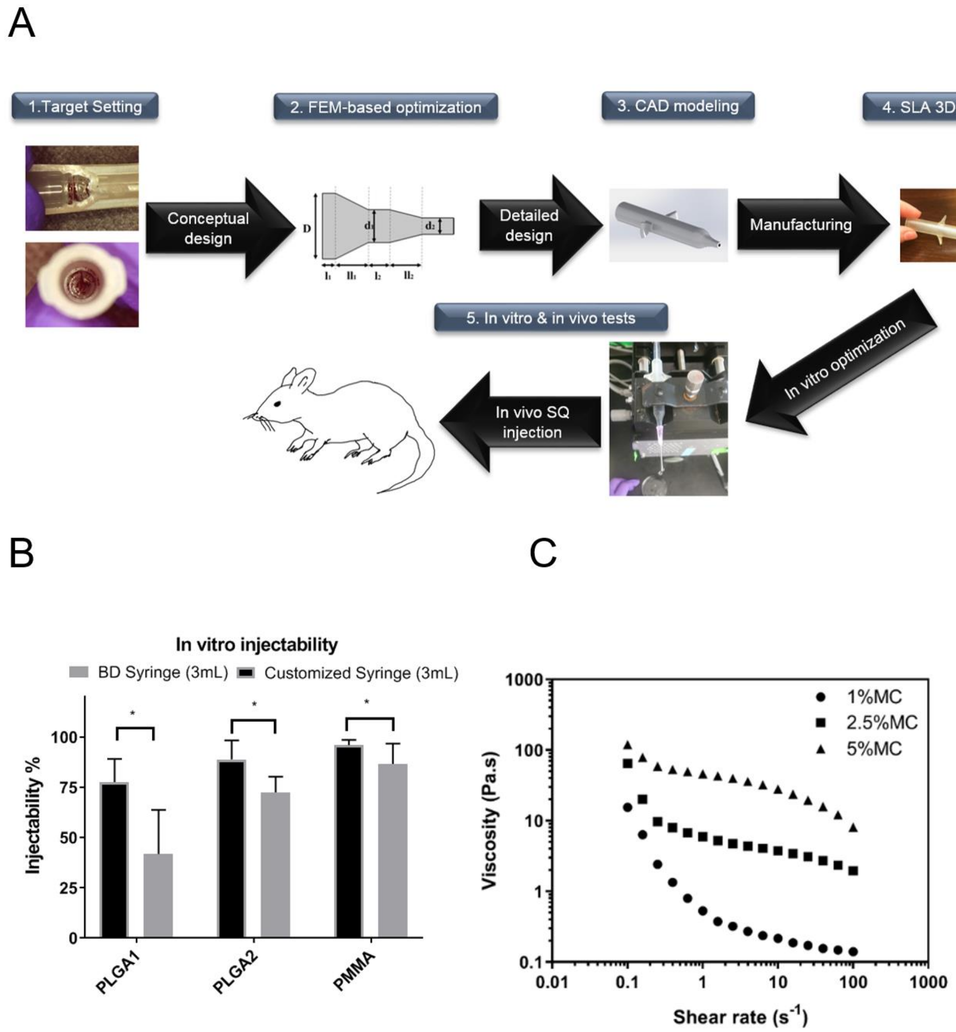

Figure 2.11: Additional information on the design and in vitro test of the customized syringe.

A) Flowchart showing steps considered in design, development, and testing of a prototype customized syringe for high injectability applications. B) In vitro injectability results of three different large (> 300 µm) microparticles using the selected custom syringe (3 mL version) compared with a commercial 3mL syringe. Full description of particle dimensions is presented in Table S1. As observed, the proposed syringe design outperformed a 3mL BD® syringe in all experiments (n=4-7). Injections were performed using 2 mL of 1%MC, an 18G needle, at zero angle relative to the horizon, lasting for ~ 10 s (* $p<0.05$). PLGA1 and PLGA2 refer to cubic particles with a dimension of 400×400×300 μm^3, and 350×350×330 μm^3, made from PLGA (Resomer® RG502H), respectively. PLGA1 has an internal cubic core of 200×200×100 μm^3 while PLGA 2 has a solid microstructure. PMMA refers to PMMA microspheres with an average diameter of 400 µm. C) The rheometric characteristics of different MC concentrations used as model viscosity enhancer as a function of shear rate.

Injection of particles in vivo can be more challenging due to less control over parenteral injection parameters, in particular, in subcutaneous injection (e. g. angle of injection, flow rate, position of syringe, etc.) High injectability in vivo plays an important step toward clinical translation of particle-based systems and drug delivery devices. In order to test our novel syringe design, we performed injectability experiments in vivo in five animal models. We also evaluated different injection strategies, including modification to the initial distribution of particles before injection, inspired by the numerical results. The injection technique based on combined use of the novel syringe design and modified particle distribution provided the best result and significantly enhanced injectability of PLGA1 and PLGA2. In case of PLGA1, it resulted in an approximately 6-fold increase in injectability compared to injection using a conventional 1 mL syringe with homogeneously distributed particles. Moreover, a 2-fold increase was observed in injectability of PLGA2 using a combination of this combined approach compared to injecting particles with initial offset but without the proposed custom syringe.

As predicted by simulations, modifying particle distribution even without using the optimized syringe was found to be another method to increase injectability. Injections with particles positioned with an initial offset distance from the plunger increased injectability of PLGA1 by a factor of 3.7 compared with homogenously distributed particles. Fabricating smaller microparticles (PLGA3) with the same cubic geometry also enhanced microparticle injectability. While injectability of PLGA3 dropped as the needle size decreased, a maximum injectability of 70% was achieved with an 18G needle (**Figure 2.10**). Further, going from a 25G needle to an 18G needle led to 2.8-fold increase in injectability of PLGA3 particles.

2.4 Discussion

While significant effort has gone towards the development of controlled release microparticle formulations, more resources are needed to better understand clinically viable administration using standard injectable methods. As the final step in administration of controlled release formulations, injection of microparticles could be a major hurdle toward clinical translation of microparticle-based (bio)pharmaceutical products [35]. Numerical models coupled with statistical approaches have been widely implemented in design optimization of various engineering systems [38-40], and more recently used for biomedical applications [41-48]. The employed modeling approach of the clog formation criterion provided a novel method to address the barrier in current numerical software for simulation of adhesion of solid bodies, which could lead to numerical instabilities in conventional finite element software. It also enabled simulation of transport of a large number of solid particles interacting with the fluid which could have been otherwise very difficult using a fluid-solid interaction (FSI) approach.

Motivated by challenges associate with injection of microparticles, especially large microparticles, we aimed to systematically study microparticle transport through hypodermic needles. To this end, we initially developed a multipyhics finite-element model coupling a CFD model of injection solution to transport of solid microparticles. Important design parameters affecting microparticle injectability were investigated using the developed model. We then proceeded with experiments to empirically examine the effect and significance of these design parameters on injectability. Based on the numerical and experimental findings, we proposed a model to predict chance of successful injection with a typical syringe-hypodermic device. Given poor performance of conventional syringe-needle devices for microparticle delivery, we finally proposed a novel syringe design that provided significantly higher injectability for a vaccine delivery platform microparticle in vitro and in vivo.

Results showed that the particle size, needle size, and solution viscosity are the three most important design parameters. Initial particle positioning in the syringe was another factor playing a major role in injectability. While the role of particle concentration was found to be negligible, large polydispersity in particle size could potentially increase the chance of needle blockage for highly concentrated and polydisperse mixtures. Since transport of larger particles require greater drag force, and these particles have faster sedimentation velocity, they are more likely to get stuck in the syringe or clog the needle during injection. A more reliable approach in such cases could be considering the greatest dimension of the microparticle population as parameter d_p and selecting the needle gauge (d_n) accordingly. Increasing needle size will not always improve injectability and the microparticle size relative to size of the needle should also be considered. From a clinical perspective, this approach is useful for obtaining an application-specific balance between allowable particle transfer and pain perception. It would therefore be important to find the minimum needle size that can provide highest injectability for a given drug delivery application.

Solution viscosity was found to be a pivotal parameter for microparticle transport, consistent with the fact that increasing viscosity of a solution could substantially increase viscous drag forces on microparticles. Notably, in case of water, due to insufficient viscous drag forces (μ=0.001 Pa.s) the density differential between polymer and water caused particles to sediment and zero injectability was observed. Two types of viscous drag force were therefore found to be essential for efficient microparticle injectability, longitudinal drag force, caused by the pressure-driven (Poiseuille) flow pushing particles toward the needle outlet, and lateral drag force resisting particle sedimentation. In more viscous solutions, both types of drag force increased, thus higher driving forces were exerted on the particles along and across the syringe. The longitudinal viscous drag force contributed to particle transport toward the needle outlet, while the transverse drag force resisted particle sedimentation.

In a laminar regime, longitudinal viscous drag forces exerted on the particles are proportional to velocity magnitude, and thus will decrease in locations where flow slows down. This can explain the reason for increased particle accumulation adjacent to syringe wall, as a result of no-slip boundary conditions, and sharp corners of the syringe corresponding to stagnation area. Viscous drag forces pushing particles forward in longitudinal direction would decrease in these areas. Moreover, in transition regions from barrel to syringe tip, and from the syringe tip to needle inlet, a sharp decrease in the diameter could limit the number of particles that can effectively flow through a given cross section. As a result, locations associated with a decrease in diameter can be another critical domain with high risk of particle accumulation.

Importantly, and somewhat unexpected, increasing viscosity did not always improve injectability. Increasing viscosity is accompanied by a decrease in Reynolds number, hence, an increase in Darcy’s friction factor. As a result, increasing viscosity can also lead to higher head loss caused by increased viscous energy losses making the flow of the injection solution through the syringe more difficult. Highly viscous solutions are also hard to be transferred to the syringe. Increasing polymer concentration in solution beyond an optimum level will not always be productive. According to current study, a solution as viscous as 1% MC therefore can provide enough viscous drag forces to both transfer particles toward the needle outlet and prevent particle sedimentation. It can also be easily transferred and aspirated to the syringe. Furthermore, while high viscosity solutions have been associated with less pain perception [28], they require higher injection pressure, and larger needle gauges to accommodate syringability requirements [27, 28].

The downside of using larger needle diameters (smaller needle gauges) is greater pain perception at the injection site [25, 26]. It should also be noted that at a certain viscosity, negative influence of the increased viscous head loss could potentially outweigh improved drag force on the particles, preventing particle transport to the needle outlet.

Results further revealed that microparticle size rather than concentration and shape, would play a major role in determining injectability. Injecting a high number of small particles would impose lower risk of needle blockage compared to lower concentration of large particles. This finding also suggests that as long as particle size (more specifically the greatest dimension of the microparticle) is conserved, various morphologies can essentially provide comparable injectability. As a result, by changing particle morphology but retaining particle size, a comparable injectability accompanied with a programmable release kinetics can be achieved. In this study, spherical particles with average dimeter of 50 µm, within the particle concentrations studied, were found easily injectable even with a 33G needle (d_n~108 µm). As such, we recommend this size as a good safety margin for injection of microencapsulated therapeutics through hypodermic needles.

The machine learning approach was further supported the findings in injectability predictions and the DOE experiments (**Figure 2.10**). Both machine learning and Taguchi based design of experiments have been widely used in pharmaceutics, healthcare, and biotechnology [49, 50]. The proposed ANN could be a more sophisticated tool for predicting injection efficacy. Notably, development of mathematical models as predictive tools for drug delivery efficacy has emerged as an area of active research [15, 23]. The trained machine learning script outputs a predicted injectability value for given values of π_1 and π_2 as the inputs. Specific conditions should be met for the proposed ANN and formula to be applicable. In general, we suggest these tools when π_2 is greater than 1 (preferably more than 2). Also, particle size distribution is another factor that might elevate risk of particle clogging. We suggest considering the greatest particle size and dimension in a population of polydisperse particles when using these tools to consider a higher level of safety. Also, it is recommended to calculate predicted injectability from both tools, find the converged values and consider the lower one. The proposed framework refers to injections performed at a zero-degree angle of injection with particles randomly distributed in barrel. At this angle, the entire component of the particle weight is perpendicular to the syringe axis and no additional component of particle weight can push particles toward the needle outlet.

Based on the proposed formula, the negative effect of using a solution with lower viscosity or particles with higher density (smaller π_1), can be partly compensated by using a greater d_n/d_p (higher π_2) (**Figure 2.10**). Increasing dimensions of the particles could be detrimental in two ways: 1) increasing sedimentation velocity and 2) increasing risk of needle blockage. While injecting smaller particles could substantially increase microparticle injectability, manufacturing smaller microparticles might not always be feasible due to process challenges or release kinetics requirements. Notably, the plateau in the 2D contour demonstrates that for a defined set of microparticle morphology and material properties (i. e. given π_1 and π_2) there would be a certain needle size at which maximum injectability could be attained. Increasing needle size beyond that level would not necessarily improve injectability, but it could adversely increase injection pain.

Finally, the presented framework was adapted to facilitate microparticle delivery of a recently developed injectable biomaterial with a complex 3D structure as the focus of this thesis (Figs. 6) [9]. Although modifying initial distribution of particles loaded in the syringe was found as an easy method for improving injectability, it might not always be feasible in clinical settings. Variations in initial particle distribution may make it challenging to control distribution of particles before the injections. Slow sedimentation velocity of small particles (<100 µm) can also make repositioning of particles a time-consuming process and hard for clinical translation.

As the second approach, we introduced design and manufacturing of a cost-effective fully mechanical syringe with an optimized profile at the tip inspired by pattern of streamlines and design of nozzles. Specially designed syringe tip profile led to less dead volume, as a major driver of cost associated with medication waste [51], compared to the commercial syringe, and decreased particle loss. Streamline-inspired syringe tip profile based on two interconnected nozzles contributed to enhanced flow of microparticles in the custom syringe and less particle accumulation in the corners. The proposed approach for design of the customized syringe based on conceptual and multi-objective optimization can be applicable to design of similar drug delivery devices such as needle-free injectors.

In this study, we used transparent resin (Formlabs® Clear Resin) for SLA 3D printing to better visualize flow of microparticles inside the syringe. While current 3D-printing technologies can provide high-quality resolution and surface smoothness, for large scale manufacturing, we envision those standard materials (e.g. polypropylene) and fabrication methods such as injection molding would be used. We further believe that the effect of material properties would be limited within a few Debye lengths away from the inner wall (a few nanometers). As such, material properties would not be expected to be of significance to the work presented here.

In summary, this study aimed to provide a comprehensive framework for microparticle injectability through hypodermic syringe-needles, and the techniques that can contribute to efficient microparticle delivery. Within the range of parameters studied, solution viscosity was found to be the statistically dominant factor followed by particle size and needle size. Increasing viscosity within the proposed range increased injectability. Increasing size of the particles and decreasing size of the needle in general decreased injectability. It was also found that concentrating particles in the centerline of the syringe, or with some offset from plunger can improve injectability. A mathematical formula was proposed to predict the chance of successful injection based on two non-dimensional parameters, capturing properties of syringe, needle, and particles. The formula was further supplemented with an ANN, both indicating that a predicted injectability of 60% can be associated with actual injectability of more than 50%. A design framework based on numerical and experimental understanding helped manufacture a cost-effective syringe tailor-made for high injectability. The syringe provided higher delivery of microparticles as compared to a commercial syringe when administered subcutaneously to mice. Results of this study can potentially be utilized in a wide range of applications for parenteral injection of advanced drug delivery carriers and injectable biomaterials, especially subcutaneously, through conventional hypodermic needles, or design of novel drug delivery devices. Future efforts can be directed toward developing scalable, cost-effective microparticle-based drug delivery devices. Future follow-up studies could also be directed toward utilization of the proposed design platform to more deeply investigate how injectability could influence the therapeutic efficacy for different indications. A potential application of the current platform could be to decrease the frequency of injections by increasing deliverable payload per injection.

2.5 Materials and methods

2.5.1 Simulations

A multiphyics model was constructed in COMSOL Multiphysics® V5.2 (Burlington, MA) to numerically study particle transport in a syringe-needle system. The model coupled CFD with particle transport flow. Additional modification was applied to consider multi-particle clog formation at the needle inlet. Accordingly, particles within needle inlet would stick together and form a multi-particle clog if they were closer than a predefined distance R_c. The model was subsequently calibrated based on experiments with similar boundary conditions to find the optimum R_c value for each needle size. In all simulations, solid microparticles were assigned a density of 1340 $\mathrm{Kg/m^3}$ to represent poly(lactic-co-glycolic acid) (PLGA; L:G=50:50). Particle transport simulations lasted for 12 s, equivalent to the time for complete plunger displacement in the corresponding experiments. The developed model was used to examine the effect of different design parameters on injectability including particle size, shape, concentration, initial distribution, needle size, and solution viscosity. Details of the modeling approach are provided in the supplemental file.

2.5.2 Experiments

2.5.2.1 Rheometric test

Different viscosities were achieved by making different concentrations of methylcellulose (MC) (viscosity: 1,500 cP, Sigma-Aldrich® USA) in water. Rheometric tests were performed at 20° C using a cup and bob geometry. The strain was held constant within the linear viscoelastic range. Subsequently, 16 data points were achieved by changing shear rate from 0.1 $\mathrm{s^{-1}}$ to 100 $\mathrm{s^{-1}}$. Three different concentrations (w/v) of MC, including 1% MC (1% w/v MC), 2.5%MC, and 5%MC were studied. In this study, low and high viscosity solutions refer to 1%MC, and 2.5%MC, respectively. Shear rate ($\dot{\gamma}$) was estimated using the following formula (*38*):

$$\dot{\gamma} = \frac{8v}{D} \quad (2\text{-}1)$$

Where *D* is the inner diameter of the syringe, and *v* is the plunger velocity (2.88 mm/s). The resulting shear rates for 1 mL and 3 mL syringes were within the same order of magnitude and therefore almost the same value of viscosity was resulted for both syringes (**Figure 2.11**). The inner diameter (*d*) for 1 mL and 3 mL syringes were measured as 4.78, and 8.66 mm, respectively.

2.5.2.2 In vitro injection experiments

To conduct injection experiments in vitro, microparticles were collected and added to a 1.5 mL plastic tube containing about 300 µL of water. In vitro injection experiments were performed using an infusion syringe pump (Harvard Apparatus PHD Ultra ®, USA) at a constant velocity of 2.88 mm/s. To retain a consistent plunger velocity identical for both syringes, different flow rates were used for each syringe size. Transferred particles were collected in a Petri dish, and then counted multiple times using an optical microscope. Similarly, non-transferred microparticles, remaining in the syringe/needle were counted at least three times under an optical microscope. The microparticle injectability percentage was calculated as the ratio of the number of transferred microparticles to Petri dish, to the total number of microparticles initially loaded in the syringe. Hypodermic needles were purchased from BD®, USA, and TSK ®, Japan. All in vitro experiments were performed at least in triplicate. Highly concentrated microparticles were counted by image analysis using software ImageJ®.

2.5.2.3 Design of experiments (DOE)

We implemented a design of experiment approach to conduct the optimum number of required experiments necessary to systematically study and compare the statistical significance of each design parameter. The statistical package Minitab ® was used to design the set of experiments based on a Taguchi L_{18} orthogonal array. Design parameters studied included solution viscosity (i. e. polymer concentration), microparticle size, shape, concentration, and needle gauge. Different levels were considered for each parameter as tabulated in **Tables 2.2** & **2.3**.

Subsequently, two different sets of DOEs were designed, namely DOE1, and DOE2. In DOE1, viscosity was a variable, based on making different concentrations of MC in water, including 0% (pure water), 1% (w/v), and 2.5 % (w/v), and 16G, 18G, and 21G needles were considered. In DOE2, viscosity was constant at 1% MC, and needle sizes included 22G, 25G, and 30G. All experiments were performed for both a 1 mL and 3 mL Luer lock syringe (18 experiments for each, n=3-4), as a model syringe-needle system. A library of nine different microparticles was studied with full descriptions provided in Table S1. Particles were classified into three size categories, namely, small, medium, and large. Statistical analysis was subsequently performed using Minitab ® statistical package. Results were analyzed using Taguchi mean of response, and analysis of variance (ANOVA) to shed light on the relative ranking and significance of each design parameter on overall microparticle injectability.

2.5.2.4 Microfabrication and micromolding

To evaluate the effect of microparticle shape, spherical, cubic and cylindrical microparticles were explored in this study. Spherical particles were purchased form Degradex, Phosphorex®, USA, while non-spherical particles were manufactured using a micromolding technique fully described in [9]. Unless otherwise stated, microparticles were made from poly(lactic-co-glycolic acid) (PLGA Resomer® RG 502H, L:G 50:50). Poly(methyl methacrylate) (PMMA), and polystyrene microspheres were additionally investigated in some experiments. To compare microparticles with different shapes but similar size, microparticle volume was considered as the reference criterion for size. Full details of the microparticle used in the DOEs is provided in **Table 2.1**. Scanning electron microscopy was used to image particles. Samples were initially coated by a thin layer of Au/Pd using a Hummer 6.2 Sputtering System (Anatech, Battle Creek, MI) and then imaged using a JSM-5600LV SEM (JEOL, Tokyo, Japan) with an acceleration voltage of 5-10 kV.

2.5.2.5 Statistical analysis

Pair-wise statistical comparisons for in vitro and in vivo injection experiments were performed in GraphPad Prism (GraphPad Software, La Jolla, CA) using an ordinary one-way analysis of variance (ANOVA) with a Tukey multiple comparison test. Multi-variable ANOVA in experimental section was performed in statistical package Minitab ®, USA. Statistical significance was considered for $p \leq 0.05$.

2.5.3 Predicting injectability and risk of needle blockage

2.5.3.1 Mathematical formulation

To predict the effects of other parameter combinations on particle injectability, we aimed to model likely outcomes. A mathematical model based on a closed-form analytical solution can be extremely complicated due to the difficulty of solving hundreds of coupled temporospatial partial differential equations defining pathlines for each particle. Inspired by Buckingham π theorem and the method of dimensional analysis we proposed a model that uses two non-dimensional parameters accounting for material properties and geometrical features to predict the chance of successful microparticle injection.

Based on finite element analysis and empirical studies, two types of forces were found to be highly decisive in microparticle injectability: particle density and viscous drag forces. To capture these effects, the following non-dimensional parameter was introduced, representing particle and solution material properties defined as:

$$\pi_1 = \frac{\mu}{\rho_p}\sqrt{\frac{C}{g}} \qquad (2\text{-}2)$$

Where μ is viscosity of the solution at a given injection flow rate, and C and ρ_p correspond to particle number concentration, and particle density, respectively, while g is the gravitational acceleration. Furthermore, because of the strong effect of particle size and needle gauge on injectability, the ratio of the needle inner dimeter (d_n) to the particle greatest dimension (d_p) was also incorporated into the model, yielding the second non-dimensional parameter:

$$\pi_2 = \frac{d_n}{d_p} \qquad (2\text{-}3)$$

Subsequently, a general formula was proposed as follows:

$$f(\pi_1, \pi_2) = a{\pi_1}^b + c{\pi_2}^d + e{\pi_1}^f{\pi_2}^g \qquad (2\text{-}4)$$

In which the first two terms represent individual contribution, and the last term represents interactive contributions of the two parameters, respectively. Curve fitting was performed using the Curve Fitting toolbox in MATLAB to find the numerical constants noted as *a-g* in the proposed formula based on the results of DEOs. The resulting numerical coefficients *a-g* are tabulated in **Table 2.5** derived from curve fitting of the above equations to the results of the experiments. This modeling approach provided an adjusted R^2 value of 0.74. An additional 22 validation experiments (n=3) were also performed with at least one parameter deviating from the range investigated in the DOEs to further investigate prediction capability of the formula. The calculated predicted injectability values were subsequently compared and correlated with the actual experimental results (**Table 2.4**).

Parameter	Numerical value
a	-15.81
b	-0.2923
c	-374
d	-0.2736
e	423.4
f	0.0003463
g	-0.1475

Table 2.5: Numerical coefficient of the predictive formula for injectability.

Values for the numerical coefficients (a-g) providing insight into chance of successful injectability. These values were obtained from curve-fitting of the injectability prediction formula, adapted from [14].

2.5.3.2 Artificial neural network

An ANN was also employed to provide a more sophisticated tool in addition to the proposed formula for predicting injectability based on the two dimensionless parameters previously described. The network structure was based on 10 hidden layers (**Figure 2.9**). Experiments, including both DOEs and validation sets, were incorporated into the network each representing a single datapoint. As a result, 319 data points were incorporated into the network, 60% of which was specified to training, 20% to validation, and 20% to testing. The training was performed using Levenberg-Marquardt backpropagation algorithm using MATLAB Deep Learning® toolbox.

2.5.4 Design and manufacturing of a customized syringe

In this study, a new syringe was designed and manufactured to achieve high microparticle injectability with good cost-effectiveness. Several steps were then taken toward design, optimization, manufacturing and testing of the proposed model in vitro and in vivo. Briefly, a parametric numerical model was first developed to enhance average and maximum magnitude of the flow velocity at the syringe tip. A few prototypes were then manufactured based on the optimized geometry out of around 500 designs. Injectability of microparticles was then compared to a commercial model and the syringe with sufficient needle attachment and superior injectability in vitro was selected for in vivo SQ injections to a mouse model. Detailed description of each step can be found in the supplemental file.

2.5.5 Multiphysics simulations

2.5.5.1 Flow field

A 3D geometry based on a 3 mL-sized BD® syringe attached to a hypodermic needle was modeled using COMSOL Multiphysics® V5.2 (Burlington, MA). The model coupled flow of the injection solution, using the CFD module, and microparticle transport, using Particle Tracing module. The current approach enabled efficient simulation of hundreds of solid microparticles flowing through the injection solution.

CFD simulations were performed under assumption of steady state, incompressible flow of a Newtonian fluid in laminar regime. All simulations were performed for both 18G and 21G needles. A physically controlled normal-sized mesh, automatically optimized for a CFD model, was selected to discretize the solution domain. Boundary conditions were considered according to equivalent experimental parameters (see experiments section for more details). As such, a constant inlet velocity of 2.88 mm/s was imposed on the syringe inlet, modeling plunger displacement, while the needle outlet was open to atmospheric pressure. Moreover, a no-slip boundary condition was imposed on the walls. Flow field was obtained based on discretized solution of Navier-Stokes equation representing continuity of linear momentum (Eq. 2-4) in conjunction with continuity of mass (Eq. 2-5) as follows [52]:

$$\rho \frac{\partial \bar{u}}{\partial t} = -\bar{\nabla} p + \mu \bar{\nabla}^2 u + \rho \bar{g} \qquad (2\text{-}4)$$

$$\rho \cdot \nabla \bar{u} = 0 \qquad (2\text{-}5)$$

where ρ is fluid density, $\bar{u}$ is fluid velocity vector, μ is fluid viscosity, *t* represents time, g refers to gravitational acceleration, and p is pressure. After performing CFD simulations, the resulting velocity field and pressure distribution were entered as the initial conditions (input at t=0s) for the subsequent particle transport simulations.

2.5.5.2 Particle transport

After obtaining velocity field and pressure distribution in the model, solid microparticles were randomly distributed throughout the syringe body (barrel) as the initial position. Microparticle transport through the syringe-needle system was then simulated by incorporating viscous drag force as well as gravity force. Buoyancy forces were also considered by taking into account the gravity forces. Transport of the particles was captured using the following formula based on Newton's second law [52]:

$$\frac{d(m_p\bar{v})}{dt} = \bar{F}_D + \bar{F}_G + \bar{F}_{Ext} \qquad (2\text{-}6)$$

Where m_p is the mass, and $\bar{v}$ is the velocity vector of a particle, respectively. The right-hand side in Eq. 2-6 represents the summation of forces acting on a particle, including drag force, gravity, and external forces, denoted by $\bar{F}_D$, $\bar{F}_G$, and $\bar{F}_{Ext}$, respectively. Eq. 2-6 describes net total force acting on the particle is equal to rate of change in its linear momentum. As the minimum particle size simulated was 50µm, no additional van der Waals or Brownian forces was taken into consideration. The drag force is calculated as:

$$\bar{F}_D = (\frac{1}{T_p})m_p(\bar{u} - \bar{v}) \qquad (2\text{-}7)$$

In which, T_p represents particle velocity response time. We used Schiller-Naumann drag force model to capture the effect of particle shape [33]. This model enabled incorporation of different microparticle shapes independent of size based on a dimensionless parameter called sphericity (ψ) defined as follows [53]:

$$S_p = \frac{\pi^{\frac{1}{3}}(6V_p)^{\frac{2}{3}}}{A_p} \qquad (2\text{-}8)$$

Where V_p, and A_p are the volume and surface area of the particle, respectively. A sphericity of 1, as a result, represents a perfect spherical morphology [53]. Cubic, cylindrical, and spherical microparticles simulated in this study had a sphericity of 0.806, 0.874, and 1, respectively. T_p in Schiller-Naumann model is calculated by [33]:

$$T_p = \frac{4\rho_p d_p^2}{3\ \mu C_D Re_r} \qquad (2\text{-}9)$$

Where d_p is the particle diameter. Parameters C_D and Re_r are calculated from Eqs. 7 & 8 as:

$$C_D = \frac{24}{Re_r}\left(1 + A(S_p)\ {Re_r}^{B(S_p)}\right) + \frac{C(S_p)}{1+D(S_p)/\ Re_r} \qquad (2\text{-}10)$$

$$Re_r = \frac{\rho||\bar{u}-\bar{v}||d_p}{\mu} \qquad (2\text{-}11)$$

In Eqs. 8 & 7 the following holds:

$$A(S_p) = e^{2.3288-6.4581S_p+2.4486S_p^2} \qquad (2\text{-}12)$$

$$B(S_p) = 0.0964 + 0.5565S_p \qquad (2\text{-}13)$$

$$C(S_p) = e^{4.0905-13.8944S_p+18.4222S_p^2-10.2599S_p^3} \qquad (2\text{-}14)$$

$$D(S_p) = e^{1.4681+12.2584S_p-20.7322S_p^2+15.8855S_p^3} \qquad (2\text{-}15)$$

2.5.5.3 Multi-particle clog formation

From preliminary experimental observations, particle accumulation was primarily present in the syringe corners and close to needle inlet, with the latter leading to catastrophic failure in drug delivery. Because clogging was not an inherent property of the model, we developed a criterion referring to microparticle clog formation at the needle inlet. A condition was developed such that if the distance between each pair of microparticles was shorter than a predefined value, called R_c, and close to the inlet, particles would stick together and form a multi-particle clog. We then conducted experiments to empirically find the best value of R_c representing the closest match between microparticle injectability in simulations and the experiments with identical boundary conditions. An R_c value of 100 µm and 120 µm for 18 and 21 G needles, respectively, represented the best match between the numerical model and actual injection experiments performed under identical boundary conditions. Different viscosity levels were attained by adding different concentrations of a model FDA-approved viscosity enhancer polymer, methylcellulose (MC), to water. Three levels of viscosities studied were water (0%MC), 1% w/v of MC in water (1%MC), and 2.5%MC. A solution of 5% MC was found extremely viscous to be transferred to the syringe and therefore was excluded from the experiments.

The effect of initial particle distribution on injectability was also studied using a 2D version of the same 3mL syringe attached to an 18G needle. For these simulations, as many as 10,000 PLGA solid microspheres with a dimeter of 100±5 µm was randomly distributed in the syringe body (barrel) as the initial condition. The same boundary conditions and mesh settings previously used in the 3D model were enforced in this model. Since no needle blockage was observed in the experiments for this system, the clog formation criterion was excluded in these simulations.

2.5.5.4 Effect of viscosity on particle size during injection

To further study the effect of flow-induced viscous shear stress on the particle size, we performed additional simulations to find the maximum shear stress among all systems studied in the DOEs. Results of simulations revealed that the maximum shear stress occurs in the smallest needle (30G) injecting 1%MC. The maximum shear stress before the needle inlet and inside the needle were found to be 0.07 MPa, and 0.19 MPa, respectively. When compared to reported stress-strain data for various PLGA materials, the estimated elongation is less than 1%, and 5%, for the 0.07 MPa, and 0.19 MPa cases, respectively [54-56]. Further, our numerical model, supported by experimental observations, indicated that clog formation occurs mostly before the needle inlet, which has a much lower maximum shear stress compared to inside the needle. As such, we assumed the effect of viscosity on the particle deformation and size to be negligible during parenteral injection.

2.5.6 A platform approach for design of a customized syringe

In summary, the following three considerations were used to facilitate the design for microparticle transport through syringe:

1) Replacing sharp wall corners in the syringe tip with a more gradual, curved profile that mimics the same curvature of the flow streamlines

2) Incorporating two nozzle designs in the syringe tip. Nozzles can increase the velocity magnitude of the flow at the outlet thus provide greater drag force on microparticles. This could decrease the risk that microparticle get stuck in the syringe-needle interface

3) Optimizing the needle tip profile for enhanced needle attachment during injections. Needle disengagement could hamper injection, and lead to tissue damage

The following steps were taken for design and development of the proposed prototype syringe

2.5.6.1 Numerical design and optimization

Numerical simulations were performed using a 2D parametric CFD model of the syringe tip to optimize the geometry. 500 simulations were performed to rank each design and find the optimum combination of different design parameters (see results section) which could optimize three objective functions simultaneously. As such, it was sought to simultaneously: 1) maximize average velocity magnitude in the syringe tip, 2) maximize highest velocity magnitude in the syringe tip, and 3) minimize syringe surface area. The goal was to minimize the surface area to reduce the dead space volume of the solution in the syringe tip which would not be transferred into the patient and could impose additional cost per injection [51]. The trade-off designs optimizing all three objective functions were then ranked using Duckstein's method [57]. Briefly, first, a hypothetic ideal design point was defined possessing the best performance in terms of all three objective functions. Then, the normalized distance of each actual design point (L_p) was calculated from this ideal point using the following formula:

$$L_p(x) = \sum_{i=1}^{k} [w_i^P \left[\frac{f_i(x)-f_i{}^0}{f_{i,max}-f_i{}^0}\right]^p]^{1/p} \quad (13 \text{ -> } 2\text{-}16)$$

Where k is the total number of objective functions, w_i is the weight for the ith objective function, f_i is the value of objective function for a given design point, $f_{i,max}$ is the maximum value of objective function in the design space , and f_i^0 is the optimum (maximum or minimum) value for the ith objective function. In this study, these values were selected as 2, and 1, respectively. As such, a design located closer to the ideal point (smaller L_p) will have a higher score, and thus will be more favorable.

2.5.6.2 Detailed design and rapid prototyping

In order to address manufacturability limitations, which cannot be incorporated using a numerical approach, we employed rapid prototyping to further optimize the selected optimum design from the simulations for real case injection applications. In the detailed design step, we used computer-aided design (CAD) software Solid Works ® to further optimize the syringe model. Accordingly, sharp corner angles associated with a conventional syringe, were replaced with a curved profile mimicking the pattern of streamlines. Also, the syringe tip profile was modified such that it could fit within a typical hypodermic needle geometry (18G), providing enough needle attachment to the syringe during injection. Accordingly, five different design candidates were manufactured using stereolithography (SLA) 3D printing with a resolution of 50 µm, made from an optically transparent resin (Formlabs® Clear Resin). Selected designs were tested for in-vitro and in-vivo injections and compared against a commercial syringe as the control group.

During the detailed design, two profiles were optimized simultaneously. First, the profile determining the interface between the needle and the syringe (i.e. external wall), and second, the profile determining the interface between the syringe and the flow (i.e. internal wall). Both were found to have pivotal influence on injectability. The first profile was optimized to provide a tapered shape facilitating needle attachment during injection. The external profile provided complete attachment to commercial needles BD® 16-25G, and only minor changes were found necessary for smaller needle sizes. Importantly, the second profile dictates the streamline pattern and was designed to not only minimize stagnation area (e. g. by removing sharp corners), but also increase the velocity magnitude at the syringe-needle interface (for enhanced viscous drag forces on the particles) by mimicking a nozzle geometry. Due to independent nature of the two above-mentioned profiles, one should be able to modify the exterior profile for any given needle without having to change the inner profile, thus eliminating any effect on the streamline pattern.

2.5.6.3 In vitro tests

The resulting optimum 3 mL version was examined based on injectability of the microparticles listed in **Table 2.3** (except PLGA3). The same type of plunger used in the 3 mL BD® syringe was also used for these experiments. Injections were performed using 2 mL of 1%MC solution, and an 18G needle attached to the syringe, while the syringe was held horizontally fixed during injections. As a result, all injections were performed at an injection angle of zero degree mimicking the same configuration in the DOEs. An approximate number of 200 PMMA microparticles, 20 PLGA1 microparticles, and 40 PLGA2 microparticles were used for in vitro experiments, and a 3 mL BD® syringe was used as the control group.

2.5.6.4 In vivo delivery of microparticles

In one group for PLGA1 and PLGA2, before injection, the syringe was held vertically for 10-20 s (longer for larger particles) with the tip facing downward, and microparticles were allowed to slightly sediment along the syringe axis. As a result, particle initial position was slightly (10-15 mm) shifted away from the plunger-solution interface, providing an offset distance from the plunger. In the other groups, particles were initially distributed homogenously in the syringe body. All injections were performed subcutaneously to a mouse using an 18G, 21G, or 25G hypodermic needle.

To calculate the injectability percentage, the number of particles in the syringe, before and after each injection were counted multiple times under an optical microscope. Three different cubic microparticles were studied in vivo. In each injection experiment, between 30-50 microparticles were injected using 200 µL of 1%MC solution. A 1mL BD® syringe was used as the control group. In vivo injections (n=5) were conducted subcutaneously on female SKH1-Elite mice (SKH1-Hrhr, Charles River Laboratories, Wilmington, MA) a hairless, but immunocompetent strain. All procedures were approved by the MIT Committee on Animal Care prior to starting experiments. On the day of injection, mice were anesthetized using continuous inhalation of 3% isoflurane and euthanized using CO_2.

2.6 Parametric study

The following section is reprinted from publication “A Multiphysics Model for Microparticle Transport through Hypodermic Needles." cited in [58].

2.6.1 Abstract

To better understand different design parameters affecting efficiency of syringes in delivery of microparticles, we have developed a multiphysics model using COMSOL Multiphysics ® V 5.3. The model couples two modules, namely, computational fluid dynamics (CFD), and particle tracing. The first module models flow of the injection solution through the syringe, also provides velocity field and pressure distribution for subsequent particle transport simulations. Next, particle tracing is considered to model transport of polymeric microparticles throughout syringe-needle. To quantify the efficacy of each design, we have quantified the number of microparticles successfully reached to the needle outlet, as the metric for delivery efficacy. Effect of a wide range of design parameters such as length and diameter of the syringe, density and size of the particles as well as overall pattern of the syringe tip are studied. Results of this study can aid in design and manufacturing of syringe/needle systems optimized for delivery of microparticles and injectable biomaterials.

2.6.2 Method

A 2D parametric model depicted in **Figure 2.12** was considered as a model medical syringe attached to a hypodermic needle [58]. Effect of different geometrical parameters were then evaluated about efficacy in delivery of microparticles to the needle outlet. The considered boundary conditions were based on a pressure-driven Poiseuille flow to mimic the pressure generated at plunger through the course of injection. Inlet velocity of 10 mm/s was considered in addition to atmospheric pressure at the needle outlet. Injection solution was considered as a model Newtonian fluid with density of 1000 kg/m3 and viscosity of 0.01 Pa.s. Flow of the injection solution was considered steady-state and stationary, and the resulting velocity field and pressure distribution were incorporated into the particle tracing as the initial condition. Simulations lasted to the time it would take the plunger to take a full course to displace through the entire barrel length (*L* in **Figure 2.12**). Two forces, including viscous drag forces and gravity were considered to model transport of particles. Syringe wall was assumed sticky, while the needle outlet had freezing properties. The number of particles frozen at the needle outlet was calculated as the number of particles transferred successfully at the end of each simulation. The barrel was initially loaded with 5000 spherical particles with density of 2200 Kg/m^3 distributed uniformly throughout the distance L. The mesh was considered physically-controlled with medium size as shown in **Figure 2.12**.

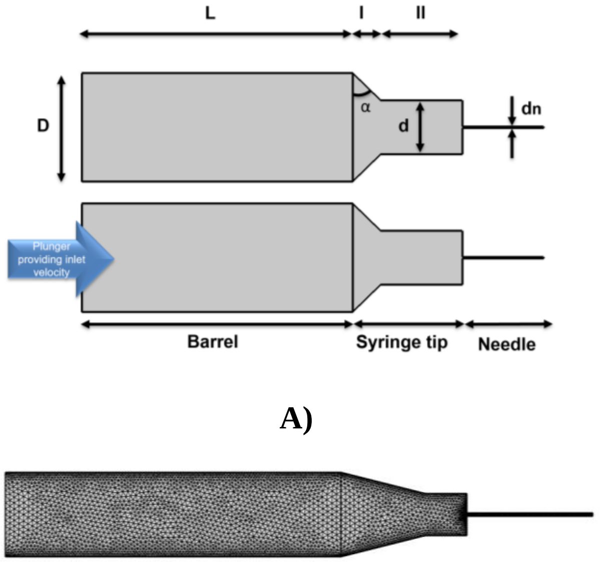

A)

B)

Figure 2.12: Overview of the 2D numerical model for parametric study of injection in a hypodermic syringe-needle system.

A) Parametric model of a medical syringe attached to a hypodermic needle used in the current study. B) Meshed geometry of a model syringe-needle used in simulations from [58].

2.6.3 Governing Equations

Fluid velocity filed and pressure distribution was obtained using CFD module based on Navier-Stokes and continuity equations as [33]:

$$\rho \frac{\partial \bar{u}}{\partial t} = -\bar{\nabla} p + \mu \bar{\nabla}^2 u + \rho \bar{g} \qquad (2\text{-}17)$$

$$\rho \cdot \nabla \bar{u} = 0 \qquad (2\text{-}18)$$

where ρ is fluid density, ū is fluid velocity vector, μ is fluid viscosity, *t* represents time, *g* refers to gravitational acceleration, and p is pressure. After, obtaining the velocity and pressure throughout the syringe under a Newtonian, Laminar, stationary flow, particle tracing module is employed. The following equations were used to model transport of particles in the syringe:

$$\frac{d(m_p\bar{v})}{dt} = \bar{F}_D + \bar{F}_G + \bar{F}_{Ext} \qquad (2\text{-}19)$$

where m_p is the mass, and $\bar{v}$ is the velocity vector of a particle, respectively. The right-hand side in Eq. 2-19 corresponds to the total forces exerted on a solid particle, including drag force, gravity, and external forces, denoted by $\bar{F}_D$, $\bar{F}_G$, and $\bar{F}_{Ext}$, respectively.

The drag force is calculated as:

$$\bar{F}_D = (\frac{1}{T_p})m_p(\bar{u} - \bar{v}) \qquad (2\text{-}20)$$

In which, T_p represents particle velocity response time. No external forces were considered in this study and the drag force was calculated based on Stokes equation.

2.6.4 Simulation Results

In the following simulations, only one geometrical parameter changed while the other were set based on a default design provided in **Table 2.6**.

Parameter	**Value**
D	10 mm
d	5 mm
d_n	0.4 mm
L	70 mm
l	5 mm
ll	5 mm
α	30°
Initial number of particles in the syringe	5000
Particle density	2200 kg/m^3
Particle diameter	10 µm

Table 2.6: Values used in the default syringe-needle design

In this regard, **Figure 2.13** demonstrates the effect of various geometrical parameters on the number of particles transported successfully to the needle outlet.

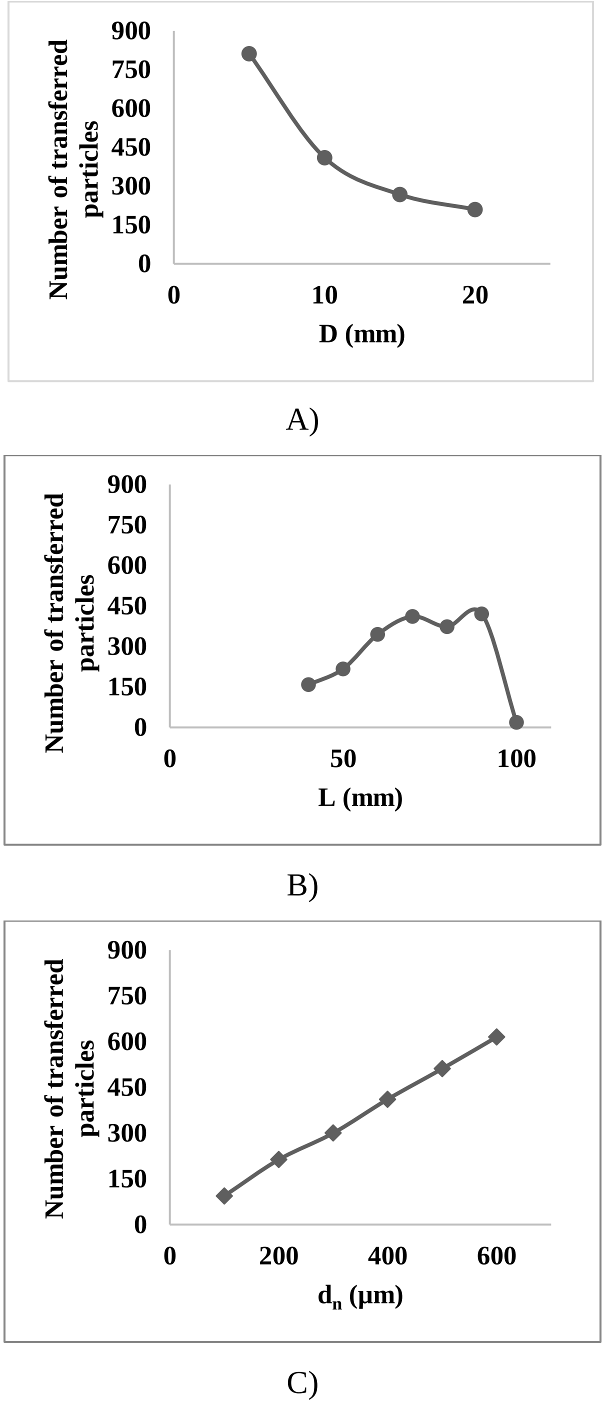

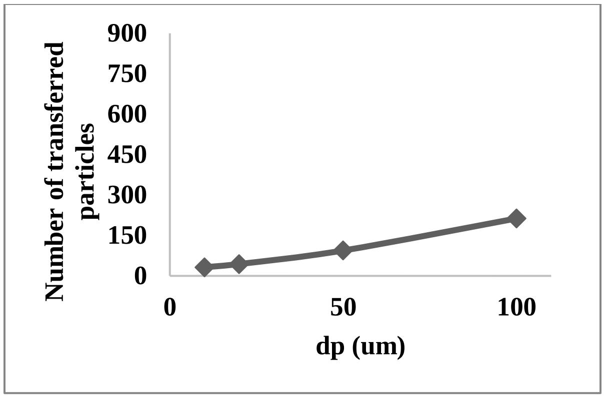

900
750
600
450
300
150
0
Number of transferred particles
0
50
100
dp (um)

D)

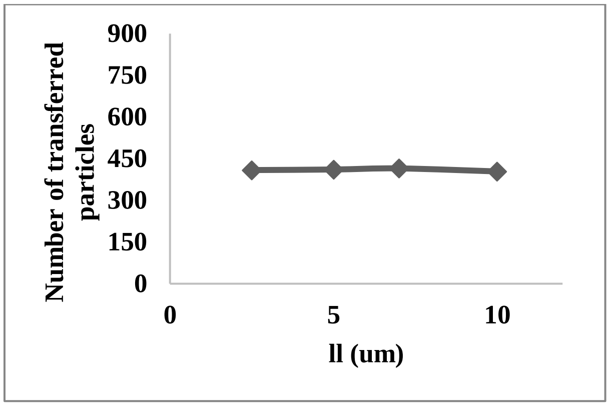

900
750
600
450
300
150
0
Number of transferred particles
0
5
10
ll (um)

E)

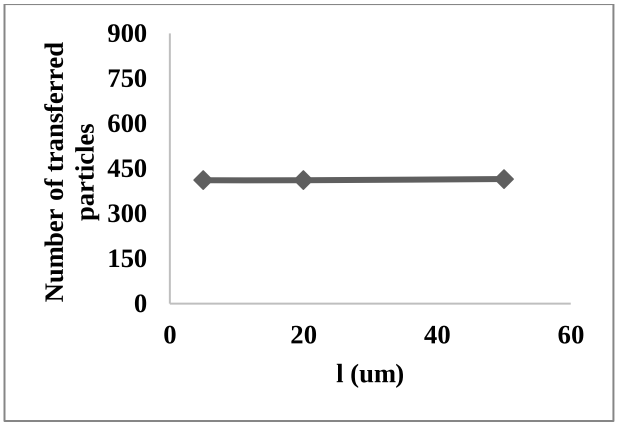

900
750
600
450
300
150
0
Number of transferred particles
0
20
40
60
l (um)

F)

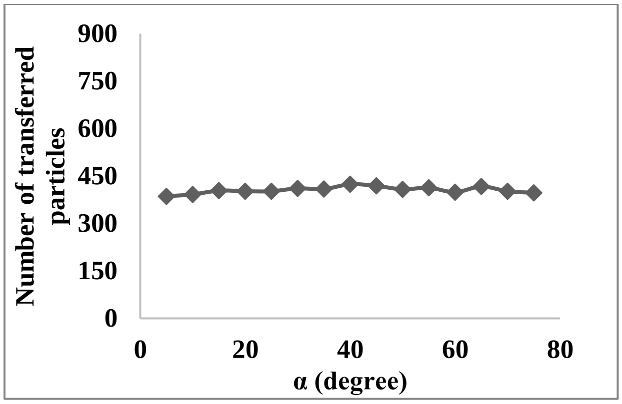

Number of transferred particles
900
750
600
450
300
150
0
0
20
40
60
80
α (degree)

G)

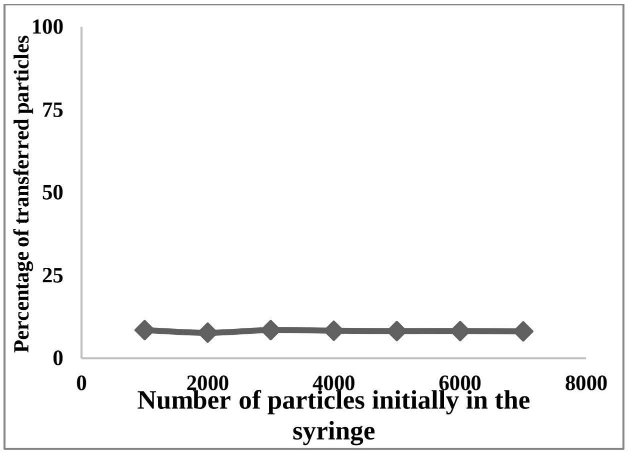

Percentage of transferred particles
100
75
50
25
0
0
2000
4000
6000
8000
Number of particles initially in the syringe

H)

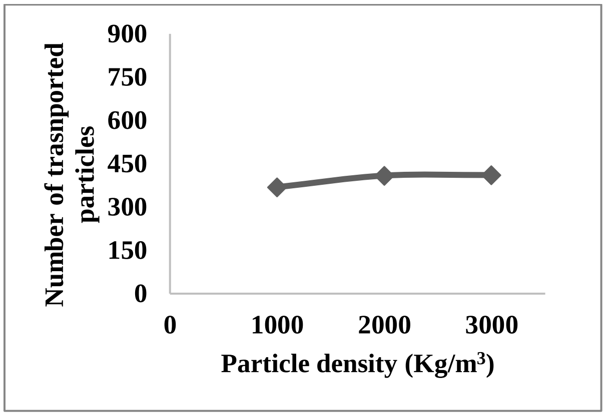

Number of trasnported particles
900
750
600
450
300
150
0
0
1000
2000
3000
Particle density (Kg/m3)

I)

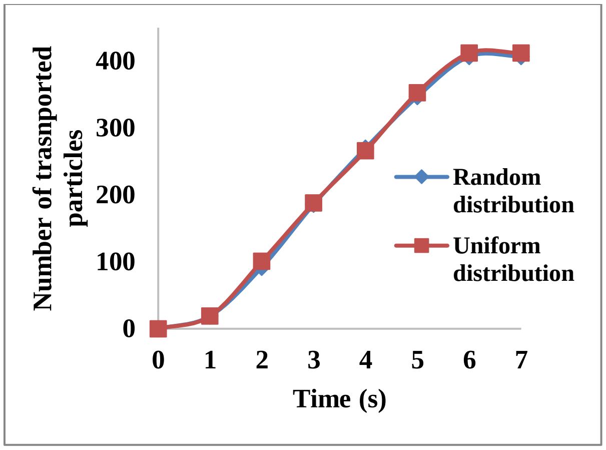

J)

Figure 2.13: Results of parametric numerical study of injection in a hypodermic syringe-needle system. A-I) Effect of different parameters on the number of particles successfully transported to the needle outlet equivalent to particles that could be delivered to the patient during injection. J) comparison between transport of delivered particles either distributed randomly or uniformly in the syringe from [58].

As observed, only a certain fraction (approximately between 2-20%) was transported successfully to the needle outlet. Not all the parameters were found equally important. For example, parameter α, *l*, and *ll* did not significantly impact transport of particles. Conversely, needle diameter, and particle size appeared as two major factors. The number of particles initially loaded in the syringe also did not have a major effect. This could be because of highly laminar nature of the flow. Two crucial design parameters were found to be diameter and length of the syringe. It was observed that only a specific range of *L* (70-80 mm) could provide optimum particle delivery. Increase in particle delivery, associated with a decreased *D*, could be attributed to higher velocity magnitudes under the same inlet flow as a result of decreased syringe diameter. Thus, potentially providing more drag force on the particles. Additionally, a linear relationship was observed between needle size and the number of transported particles. Increasing particle size also significantly decreased particle delivery. Particle density was not found as a significant factor within the range studied. In terms of initial distribution of particles, both uniformly distributed particles, and randomly distributed particles had a similar trend of transport toward the needle outlet.

These results suggest particle size, length and diameter of the syringe, and needle size could be four major components in design of syringe-needle systems. Furthermore, as depicted in Figure 4, most of the particles accumulated in the walls in the transition area from syringe to needle considered as sticky walls in this study. Most notably, they accumulated in the areas with diverging streamlines (**Figure 2.14**) with elevated pressure and lower velocity magnitude. This potentially suggests syringe designs that better mimic the pattern of flow streamlines could provide higher particle delivery.

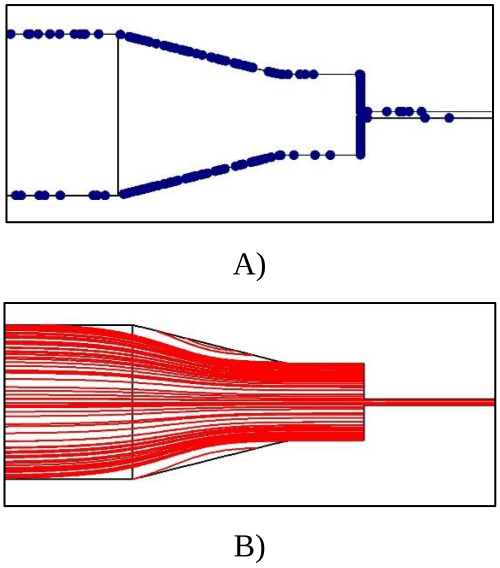

Figure 2.14: Streamlines in the parametric model.

A) Accumulation of particles on the sticky walls, B) pattern of streamlines on the corresponding design in A [58].

2.6.5 Discussion

This numerical study highlights the power of COMSOL Multiphyscis ® in preliminary design and optimization of biomedical systems. Although finite element approaches have been widely used in design optimization in micro- and macroscales [38-40, 58,59], more studies are required to address optimization of biomedical systems that directly interact with human body such as engineered drug delivery scaffolds, microneedles, or hypodermic needles [21, 60]. Hypodermic needles are widely used over the world, and as such, optimization with the aim of improving particle delivery could be of high importance. In this study, unique feature of COMOSL

Multiphysics ® enabled coupling of two different physics, namely, CFD, and particle transport. Results of this study pointed out that not all the design parameters in medical syringes are equivalently important and certain parameters should be taken more seriously such as length and diameter of the syringe. Also designs that could minimize stagnation area in transition region from syringe to needle could potentially provide better delivery performance. Using these simulations, we also demonstrated that conventional syringe-needle systems are not optimized for delivery of microencapsulated therapeutic products. This could highlight the importance of designing customized needles for delivery of large injectable scaffolds and microparticles.

2.6.6 Conclusions

This parametric study demonstrated a novel application of COMOSL Multiphsyics ® for modeling transport of microparticles in a medical syringe attached to a hypodermic needle. We investigated the effect of several parameters related to geometry of the system and particle properties. Certain parameters were found more dominant such as size of the particles and the needle. Future studies could be directed toward experimental studies and more complicated two-phase, or shear-thinning solutions. Results of this study could have applications in initial steps of design and manufacturing of novel medical syringes tailor-made for advanced drug delivery purposes based on microencapsulation.

CHAPTER

3

MECHANISM OF PULSATILE RELEASE

This chapter summarizes one of the fundamental aspects of core-shell microparticles, namely, mechanism of pulsatile release. The unique delayed-pulsatile release kinetics enables novel applications such as single injection vaccine delivery or extended release of small hydrophilic molecules. Various experimental and computational tools were used or developed to achieve a multi-faceted understanding of the degradation mechanism. Results in this chapter can not only be applied to understanding of mechanism of release in core-shell particles, but also more broadly in conventional PLGA-based biomaterials such as microspheres.

3.1 Abstract

Next-generation therapeutics require advanced drug delivery platforms with precise control over morphology and release kinetics, capable of delivery of a wide range of cargos such as vaccines and biologics. A recently developed multi-layer microfabrication technique enables fabrication of a new class of injectable microparticles with a hollow 3D core-shell structure that displays pulsatile release kinetics, providing such capabilities. To study the mechanism of pulsatile release in these particles, herein, we employed a combination of experimental and computational tools. We demonstrated that pulsatile release is governed by a sudden increase in porosity of the polymeric matrix leading to formation of a porous path connecting the core to the environment. Moreover, the release kinetics within the range studied remained primarily independent of cargo molecular size, particle geometry and size, but highly dependent on particle composition. A qualitative technique was developed to study the pattern of pH evolution in core-shell microparticles with heterogeneous microstructure. A computational model based on the

theory of poroelasticity successfully modeled deformations caused by pore-formation, indicating sudden expansion of the particle prior to onset of release. Results of this study can contribute to the understanding and design of advanced drug delivery systems.

3.2 Introduction

Biodegradable core-shell microparticles represent an extremely promising class of injectable biomaterials with applications that can improve efficacy and adherence. These applications include single injection vaccine delivery, transdermal vaccine delivery, cancer immunotherapy, and pH-triggerable oral drug delivery, all of which are otherwise infeasible with traditional drug delivery systems [9-11]. Controlled drug delivery technologies can particularly aid in the treatment of diseases that require multiple shots by improving patient adherence [14,15,17]. Patient adherence is reported to be as low as 50% globally, costing the US healthcare system alone more than $100 billion annually [61-63]. They can also potentially unlock new therapies by removing the need for multiple surgeries or difficult injections in the treatment of solid tumors [64-66]. Furthermore, by simplifying the dosing regimen and eliminating the need for multiple visits to healthcare providers, single administration systems can also be an effective tool in eradication of infectious disease outbreaks [13].

Sustained drug delivery microparticles have been widely studied in the literature [67-69]. However, the mechanism of pulsatile release from microparticles upon degradation is poorly understood. Pulsatile release devices have emerged as a new class of drug delivery systems utilized for a wide range of applications [71-72]. The mechanism of degradation in biodegradable drug delivery systems is perceived to be a complex phenomenon, caused by an interplay between multiple factors (e. g. pore formation, swelling, pH change, etc.) [67-69]. Understanding the mechanism of release from biodegradable microparticles with complex geometries is crucial for design of next-generation biomaterials [73,74]. It can also enhance our understanding of conventional drug delivery systems such as microspheres made from PLGA [67-69, 73,74]. Comprehensive studies have been conducted on conventional PLGA-based drug delivery systems (e. g. microspheres) [67-69, 73,74]. However, the underlying complexity of degradation mechanism requires independent studies for each novel class of PLGA-based biomaterials [74]. As such, degradation behavior of a certain class of PLGA-based biomaterials (e. g. microspheres, scaffolds, implants) cannot necessarily be expanded to other classes.

To provide insights into the pulsatile release mechanism from biodegradable core-shell microparticles, we perform a comprehensive study using various experimental and computational tools. Specifically, we focus on particles with a 3D microstructure which can be fabricated thanks to a recently developed multi-layer microfabrication technique termed StampEd Assembly of polymer Layers (SEAL) [9]. These 3D core-shell microparticles demonstrate a delayed pulsatile profile, which can be programmed from a few days up to several months [9,10]. This technique is a high-resolution, bottom-up approach compatible with medical grade materials such as PLGA [9]. In brief, core-shell microparticles are fabricated first by filling the aqueous solution of therapeutic cargo into the core inside the base layer. Subsequently, an additional layer of particle cap is aligned and sintered with the filled base, fully sealing the core, and forming a 3D core-shell microstructure (**Figure 3.1 A**) [9, 10]. These microparticles' unique tunability, in terms of release timepoint, morphology, and compatibility with biologics and hydrophilic small molecules, provides a wide range of opportunities for injectable pulsatile drug delivery [9, 10].

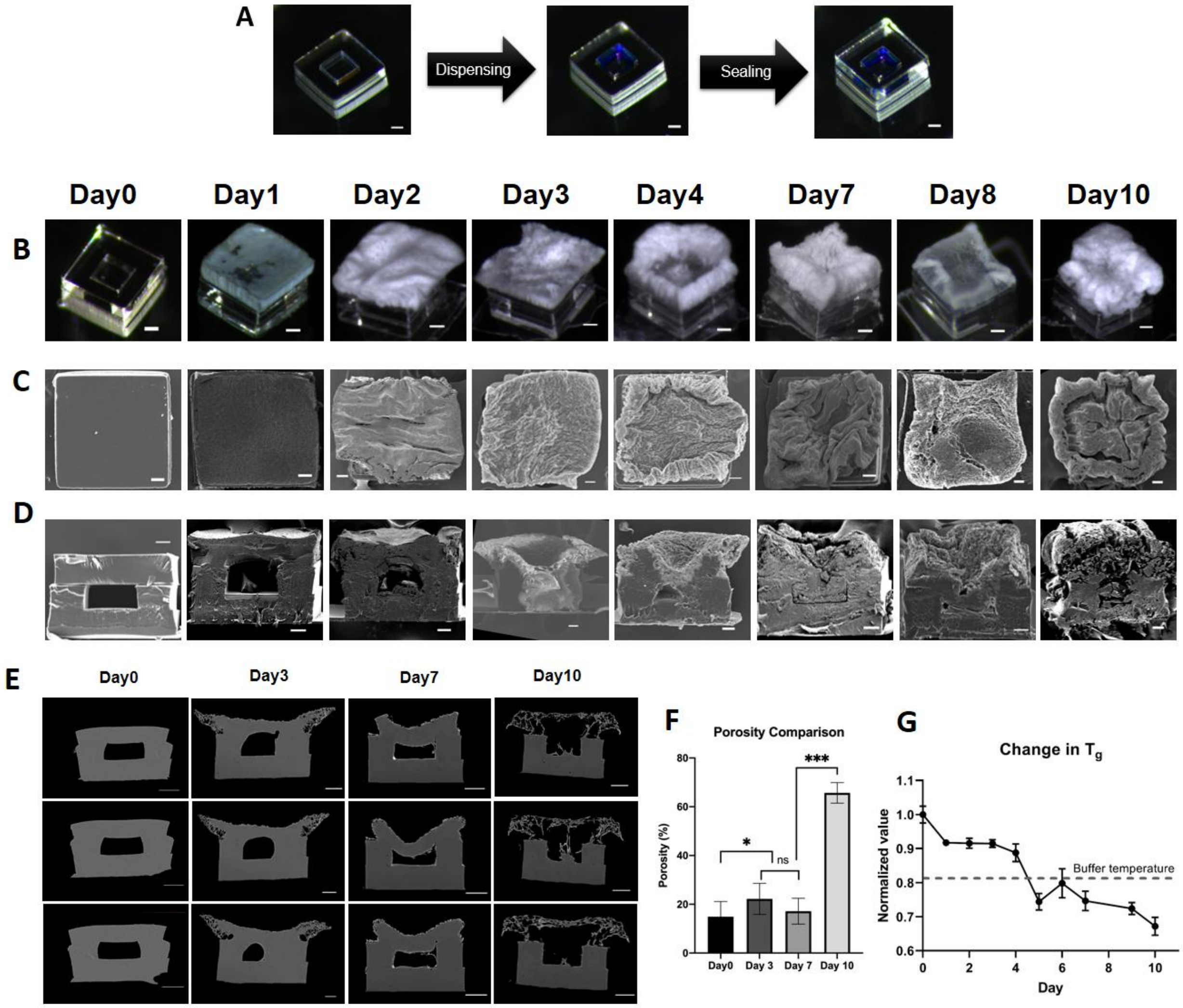

Figure 3.1: Visualization of deformation and pore formation in biodegradable core-shell microparticles. **(A)** Overview of the fabrication process of biodegradable core-shell microparticles. **(B)** Visualization of microstructural evolution in an empty core-shell microparticle with fast-degrading PLGA in the cap (RG 502H) and slow degrading PLGA in the base (RG 756S) at different time points obtained by B) optical microscopy, **(C)** surface SEM, **(D)** cross sectional SEM, and **(E)** nanoCT visualization between comparable cross sections across the cross section of particles. **(F)** Change in porosity of microparticle over time obtained from nanoCT analysis. **(G)** Change in glass transition temperature (normalized by day 0) of polymer films as a model for fast degrading cap (RG 502H). Scale bars in A-D show 50 µm, and in E 100 µm. Error bars show SEM.

In this study, we first investigate the microstructural evolution occurring on the surface and within the internal structure at a single microparticle level. We employ multiple tools including optical microscopy (OM), surface and cross-sectional scanning electron microscopy (SEM), energy dispersive X-ray spectroscopy (EDS) in conjunction with SEM, and state-of-the-art nano-resolution computed tomography (nanoCT). We also utilize differential scanning calorimetry (DSC), thermogravimetric analysis (TGA), and compression tests to study change in material properties of particles upon degradation. Next, using fluorescent-based labeling and nano-resolution 3D printing (NanoScribe), complementing the SEAL method, the effect of a wide range of size- and material-related parameters on release profile are directly studied. A qualitative method was developed to study pH change in various particle groups and examine parameters affecting deformation of particles. We also studied how addition of polyethylene glycol (PEG) to PLGA can be used to modulate the release timepoint and pH. To reinforce experimental understanding, a multiphysics finite element model is further constructed based on the theory of poroelasticity. The numerical model coupled with a design of experiment (DOE) approach allowed us to study the effect and importance of four dimensionless parameters on particle deformation, which would not be possible with experiments alone. Overall, these tools helped us form a model that elucidated the mechanism of pulsatile release from biodegradable core-shell microparticles, with a hollow microstructure, 3D printed or SEAL-fabricated.

3.3 Results

3.3.1 Investigating microstructural evolution upon degradation

To investigate the evolution of the internal structure upon hydrolysis-based degradation, various assays were performed on a model cubic core-shell microparticle with cap and base made from PLGAs of different molecular weights. The cap and base were fabricated from a fast degrading PLGA (RG 502H) and a slow degrading one (RG 756S), respectively. We used various tools, namely, optical microscopy (OM), cross-sectional and surface SEM, EDS-SEM, and nano-resolution computed tomography (nanoCT) to study mechanism of degradation (Figs. 1, 2). OM revealed that unlike the slow degrading base, which remains mostly transparent up to day 10, upon hydrolysis, the fast-degrading cap starts to turn opaque one day after incubation. This change in the transparency of the cap was accompanied by deformation and initial expansion, while the base maintained its transparency and cubic microstructure (**Figure 3.1 B**). Surface SEM indicated formation of deformation patterns on the cap, most notably two days after incubation which were more pronounced on the edges of the cap (**Figure 3.1 C**). Results of cross sectional SEM and nanoCT imaging demonstrated the creation of a pore-forming zone on the edge of the cap while the base remained fully non-porous (**Figure 3.1 D & E**). Networks of interconnected pores were observed at day 10, connecting the core to exterior buffer. Quantification of porosity (void in cap and core combined) based on nanoCT imaging for individual particles revealed that cap became significantly more porous at day 10 (~ 3 times more than at day 7), while having similar porosity at days 3 and 7. Observations made by OM and SEM were further confirmed in additional particles (**Figures 3.2-3.4**). The same observation regarding degradation of the cap, and pore progression was confirmed in another cubic core-shell microparticle with a similar composition (i. e. cap and base) but a larger core (18 nL vs 4 nL), and a thinner cap (50 µm vs 100 µm) (**Figure 3.4**).

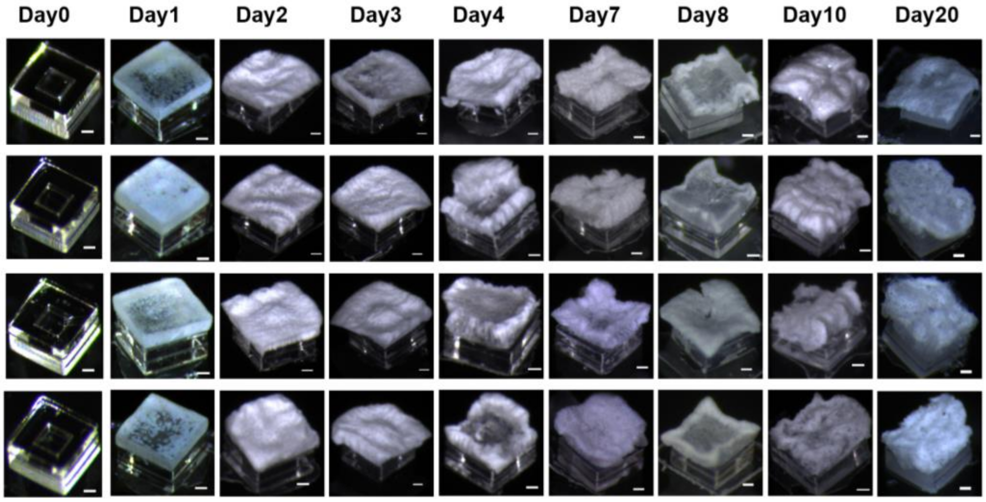

Figure 3.2: Optical images showing degradation of core-shell microparticles over time

Additional optical images demonstrating evolution of the microstructure in biodegradable core-shell microparticles (empty core) made from fast degrading cap (PLGA RG 502H) and slow degrading base (PLGA RG 756S) incubated at 37°C in PBS. Scale bars show 50 µm.

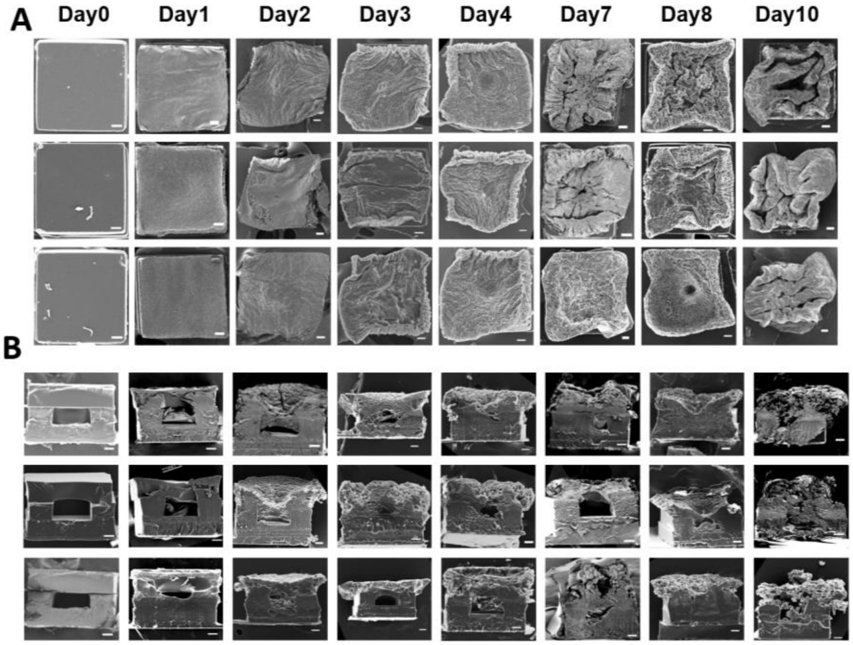

Figure 3.3: More comprehensive cross sectional SEM images showing degradation in additional population of particles.

Additional SEM images based on (A) surface SEM, and (B) cross sectional SEM, demonstrating degradation of microparticles with a 4nL (4X) core and 100 µm thick- cap upon degradation incubated in PBS at 37°C. Scale bars show 50 µm.

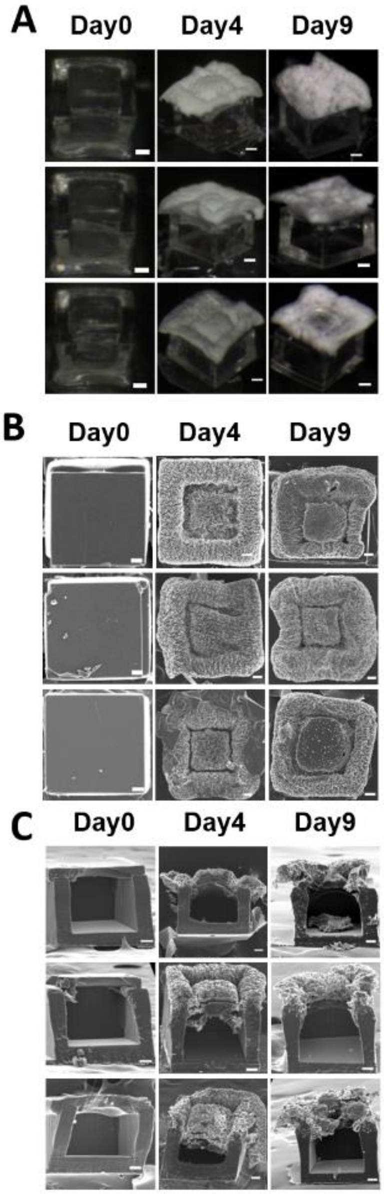

Figure 3.4: Additional optical and SEM images showing degradation in a core-shell particle with larger core and thinner cap

Additional (A) optical, (B) surface SEM, and (C) cross sectional SEM, illustrating degradation of empty core-shell particles with larger core (18nL, 18X) and thinner cap (50 µm), made from fast degrading cap (RG 502H) and slow degrading base (RG 756S). Scale bars show 50 µm.

To investigate the effect of degradation on material properties of SEAL-fabricated microparticles, we further performed DSC, TGA, and mechanical compressive tests. Tests involved studying the change in glass transition temperature (T_g), degradation temperature (T_d), and elastic modules (E) of the samples made from RG 502H over time (n=3-5). Results showed a decrease in all three properties upon degradation by hydrolysis, more significantly within days 9-10 (**Figures 3.1, 3.5, 3.6**). Notably, it was previously shown that day 10 was also associated with significantly higher porosity. The values of T_g, T_d , and *E* dropped by more than 30%, 10%, and two orders of magnitude from day 0 to day 10, respectively.

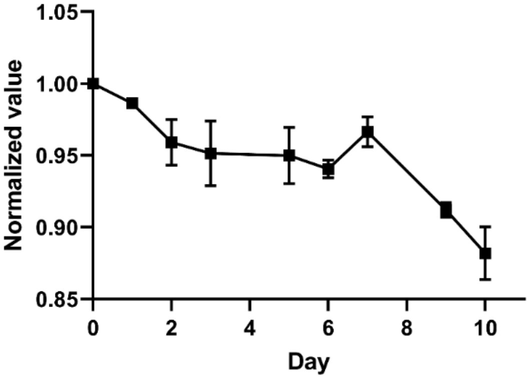

Figure 3.5: Change in degradation temperature (T_d) of polymeric particles upon incubation in vitro

TGA analysis of polymer films, as a model for particle cap, made from slow degrading PLGA (RG 502H) upon degradation, incubated in PBS at 37°C (buffer temperature). The graph shows change in degradation temperature (T_d) normalized by the non-degraded sample (day 0). Error bars show SEM.

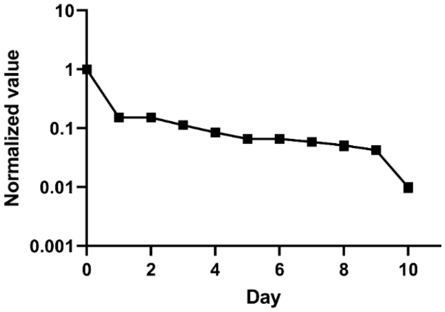

Figure 3.6: Change in the elastic module of polymeric particles over time.

Change in normalized elastic module (*E*) of cubic solid microparticles, as a model for the cap, made from fast-degrading PLGA (RG 502H) upon degradation over time, incubated in PBS at 37°C. The values are normalized by the non-degraded sample (day 0). Error bars show SEM.

To visualize release of the cargo, Alexa Flour (AF)-labeled 10kD dextran (10kD-dext), as a model biomacromolecule, was encapsulated in the core and OM was used to visualize its release from the core-shell microparticles at different time points (**Figure 3.7 A**). OM results revealed that cargo remained fully entrapped in the core, up to day 5, but started to leave the particle through the cap at day 6 (**Figure 3.7 A**). Notably, the cargo traveled through the networks formed within the thickness of the cap (**Figure 3.7 B**) previously identified. We then encapsulated Iron(II) sulfate heptahydrate ($FeSO_4.7H_2O$) in the core to further study mechanism of the release with EDS-SEM which can distinguish different elements (**Figure 3.7 C**). In agreement with previous observations, EDS-SEM also confirmed the entrapment of cargo at day 3 but formation of a network of Fe (red contour) in the cap, connecting the core to exterior buffer at day 10 (n=3).

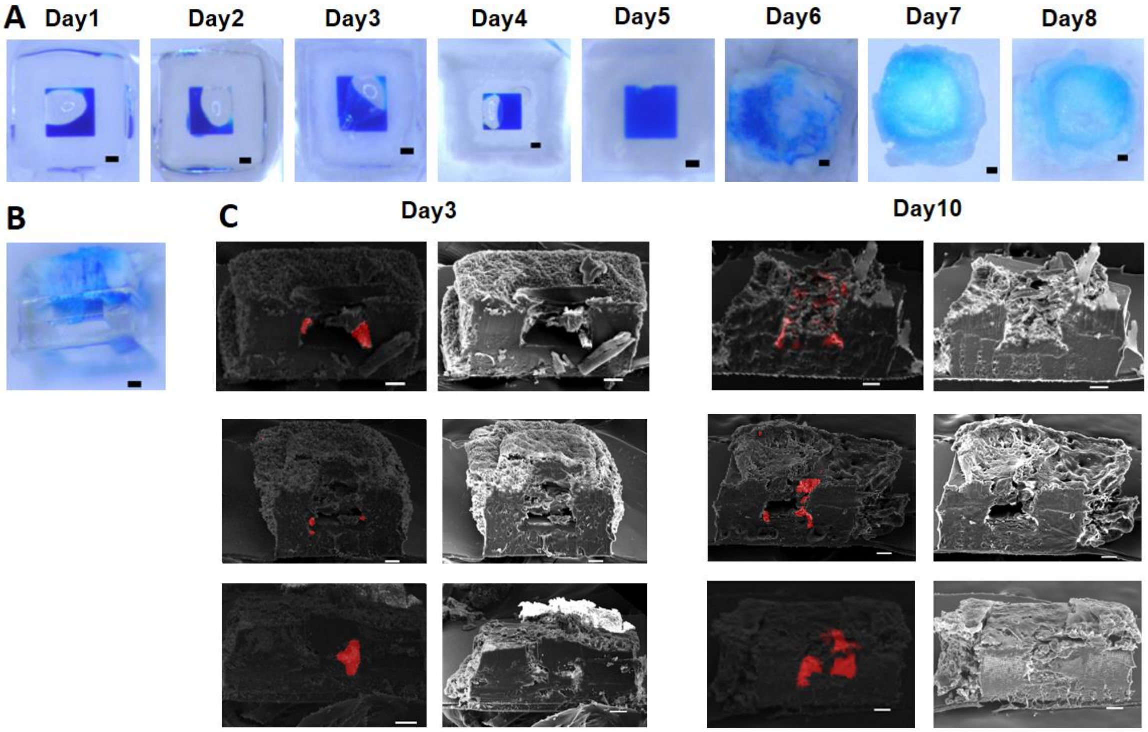

Figure 3.7: Path formation caused by interconnected pores in the cap leading to pulsatile release of the cargo. (A) Optical visualization of release of a model macromolecule, labeled with fluorescent dye (AF 647- 10kD dextran, blue color), from the core in a core-shell microparticle fabricated with fast-degrading cap (RG 502H) and slow-degrading base (RG 756S). (B) Optical visualization of patch formation in the cap connecting core to the environment, leading to pulsatile release of the cargo. (C) Elemental cross-sectional SEM (EDS-SEM) illustrating path formation in the cap connecting cargo (Fe), visualized in red, to the external environment at day 10, while encapsulating it at day 3. Scale bars show 50 μm.

3.3.2 Effect of design parameters on release kinetic

The effect of size-related and material-related design parameters on the release kinetics were studied (**Figure 3.8**). Size-related parameters included cap thickness, core size (volume), particle geometry, wall-thickness, and molecular size of the cargo. The range of cargo molecular weights included dextran-free AF647, and AF647 labeling three molecular weights of dextran, namely, 10kD, 70kD, and 2000kD (four groups total including dextran-free dye). Material-related parameters included PLGA molecular weight and end group (i. e. PLGA terminated with ester or acid end groups). We also studied release kinetics of hybrid caps, composed of a blend of two PLGAs with varied degradation rates. The release timepoint was defined as the earliest day at which at least 50% of the cargo is released.

As seen in **Figure 3.8**, the overall delayed-release pulsatile profile was maintained across all 25 cases of particle designs studied. Increasing the cap thickness twice, from 50 µm to 100 µm, but maintaining the particle composition, resulted in a maximum difference of only 2 days in release timepoint across the entire range of cargo molecular sizes studied (**Figure 3.8**). Same difference in release timepoint was observed when increasing the core size, 4.5 times, from 4 nL (4X) to 18 nL (18X) with identical particle composition. Similarly, among a given group of particle dimensions, various molecular weights of the cargo led to a maximum difference of 2 days across the range studied. Using Nano resolution 3D printing (NanoScribe), we further studied the effect of particle shape on the release kinetics of cylindrical and cubic microparticles. In agreement with previous observations, the maximum difference between the release timepoint of cylindrical and cubic core-shell particles with a 1nL (1X) core was found to be 2 days across two wall thicknesses (50 µm and 100 µm).

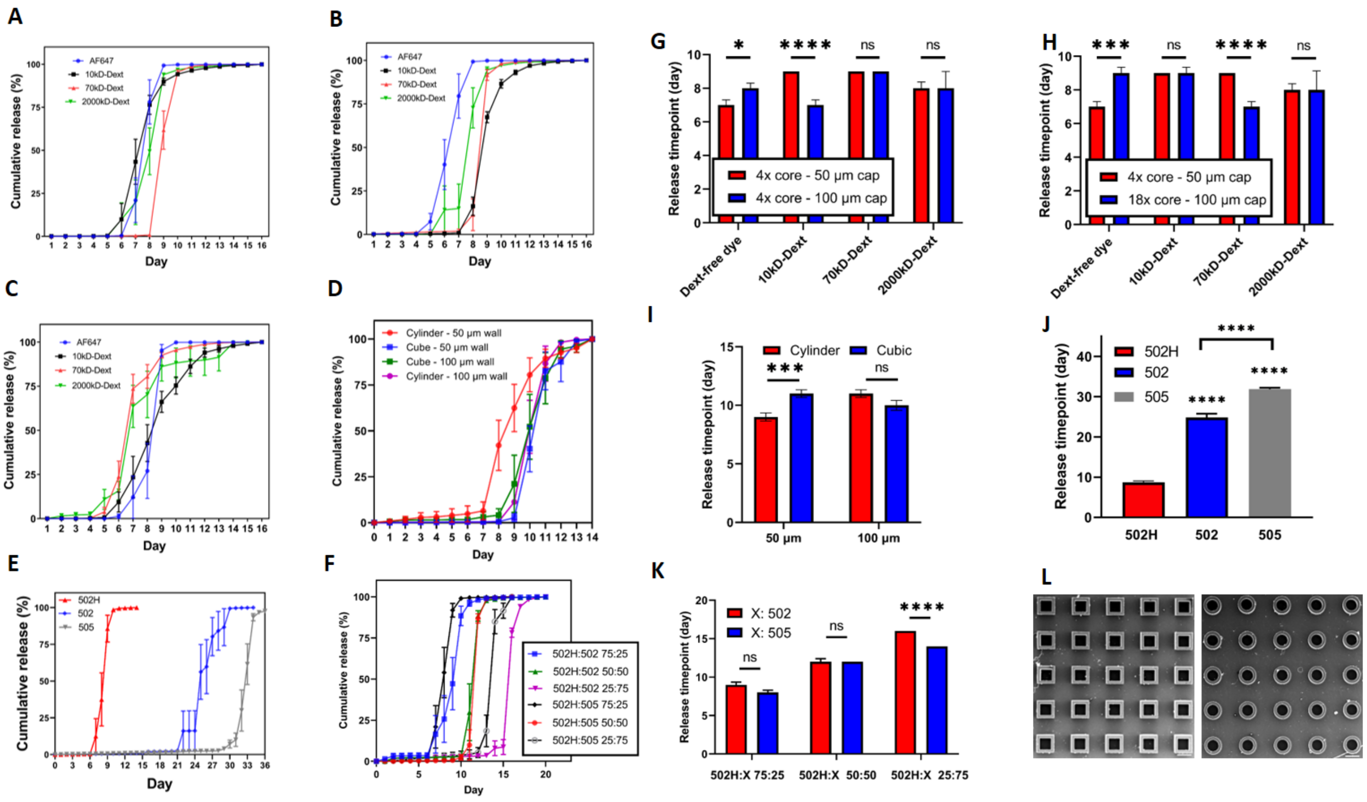

Figure 3.8: Investigating the effect of design parameters on release kinetics in biodegradable core-shell microparticles.

(A) Cumulative release profile of dextran-free AF647, and AF647-labeled 10kD, 70kD, and 2000kD dextran from core-shell microparticles with different geometries including (A) 4X-core, 100 µm thick cap, (B) 4X-core, 50 µm thick cap, and (C)18X-core, 50 µm thick cap. (D) Release profile of AF647-labeled 10 kD dextran from core-shell microparticles with different shapes and wall thicknesses. Particles in A-D are made from the same fast-degrading cap and slow-degrading base as in Figs. 1 & 2. Cumulative release profile of AF647-labeled 10 kD dextran from core-shell microparticles with caps made from (E) pure PLGAs or (F) a blend of two different PLGAs. Particle base in E & F are made from the same slow-degrading PLGA as rest of this study (RG 756S). Statistical analysis of release timepoint comparing the effect of (G) cap wall thickness, (H) core size, (I) shape, (J) cap molecular weight and end group, (K) different blends of PLGAs in the cap. (L) SEM images of the base in a group of cubic and cylindrical microparticles studied in D & I fabricated by NanoScribe 3D printing. All release profiles correspond to particles incubated in vitro (n=6-10). Release timepoint corresponds to the earliest day for average cumulative release of at least 50% of the cargo. Scale bars show 100 µm. Error bars show SEM.

Moving to material-related parameters, we investigated the effect of different cap compositions on the release timepoint of AF647-labeled 10 kD dextran in a cubic particle. The particle was made from 100 µm thick cap, and 4 nL core, (base was made from RG 756S). It was revealed that the difference between average release timepoints for microparticles capped with PLGA of 19 kD, either ester-terminated (RG 502) or with acidic end group (RG 502H), was as large as 16 days. The difference between the average release timepoint of two ester-terminated PLGAs with varied MWs (502 & 505, 19 and 53 kD, respectively) was found to be 7 days. We also studied the release kinetics in hybrid caps composed of different PLGA blends with varied MWs and/or end groups. The average release timepoint in hybrid caps composed of 502H and either 502 or 505 (X) was statistically insignificant for 502H:X 75:25 & 50:50. The difference was found to be significant when the ratio of 502H:X changed to 25:75. Collectively, these results pointed out to higher importance of PLGA molecular weight and end-group compared to particle size and shape in controlling the release timepoint.

We also compared the release kinetics in heterogeneous and homogenous core-shell particles. In the homogenous particles, both cap and base were fabricated from the fast-degrading PLGA (RG 502H). In the heterogeneous group, only the cap was made from 502H and the base was fabricated from the slow degrading PLGA (RG 756S). Aside from material composition, other design parameters were identical among the two groups. Interestingly, the release timepoint was similar among both groups, showing that degradation depended on the fastest degrading polymer (**Figure 3.9**). Moreover, the release timepoint could be controlled by only changing the cap composition (instead of changing the entire particle composition). Cross sectional SEM in the homogenous group revealed that pores started to progress from the edges of the particle toward the core, eventually making a patch of interconnected pores at day 10 (**Figure 3.9**). The pore progression starting from the edge of particle was found similar to degradation pattern in heterogeneous particles with only cap made from the fast degrading PLGA .

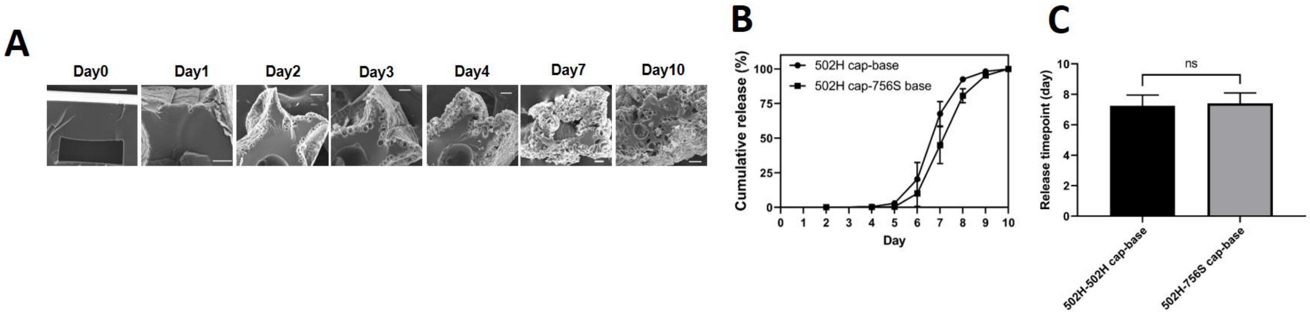

Figure 3.9. Degradation mechanism in a core-shell microparticle with homogeneous cap and base

(A) Cross sectional SEM images showing pattern of pore formation in core-shell microparticles with both cap and base fabricated from fast-degrading PLGA (RG 502H). Scale bars show 100 µm. (B) Cumulative release of a particle with both cap and base made from RG 502H compared to a particle with RG 502H cap and RG 756S base (slow-degrading PLGA). (C) Comparison of release timepoint between the above-mentioned particle groups. In B & C, n=6-10. Particles have a 4X core and 100 µm-thick cap. Error bars show SEM.

3.3.3 pH evolution upon degradation

To study dynamic pH changes in particles, we employed a qualitative colorimetric technique with the same particle design studied previously, (**Figures 3.10-3.12**). Initially, a universal pH indicator (pH 4.00-10.00) was dispensed into the core and change in the color was visualized over incubation in PBS at 37ºC (**Figures 3.10-3.12**). We observed that upon water permeation into the core, starting at day 1, the indicator changed color to a spectrum of yellow to red, demonstrating a minimum pH of 4 or less. The pH change in the cap was studied by OM in three groups: two groups loaded with another pH indicator, thymol-blue, namely, cap-only particles and full cap-base particles, and a control group. The control group was considered with a full cap-base structure and no indicator loaded. OM results demonstrated formation of a less acidic zone on the edge of the cap (yellow, $2.8 \leq pH \leq 8.0$), progressing towards the center of the particle while the center of the cap remained more acidic (pink, $pH \leq 1.2$). Comparison between cap-only and full cap-base particles indicated that acidic products, formed upon degradation, accumulated in the core, while the cap-only group turned entirely yellow (less acidic) at day 5. Next, the effect of PEG (2 kD, PEG:PLGA 50:500) in increasing the pH when doped in the cap was studied, making a blend of PEG/PLGA, with a full cap-base and a cap-only structure. We then hypothesized that addition of PEG could accelerate pore formation in the cap, leading to elevated pH level in the cap caused by improved clearance of acidic products. Both PEG-loaded PLGA caps remained pale yellow and without any highly acidic pink region, for up to day 6, at which point the pH indicator diffused out from the cap. Observations regarding pH evolution were further confirmed in an additional 3 particles per group/per timepoint (**Figure 3.12**).

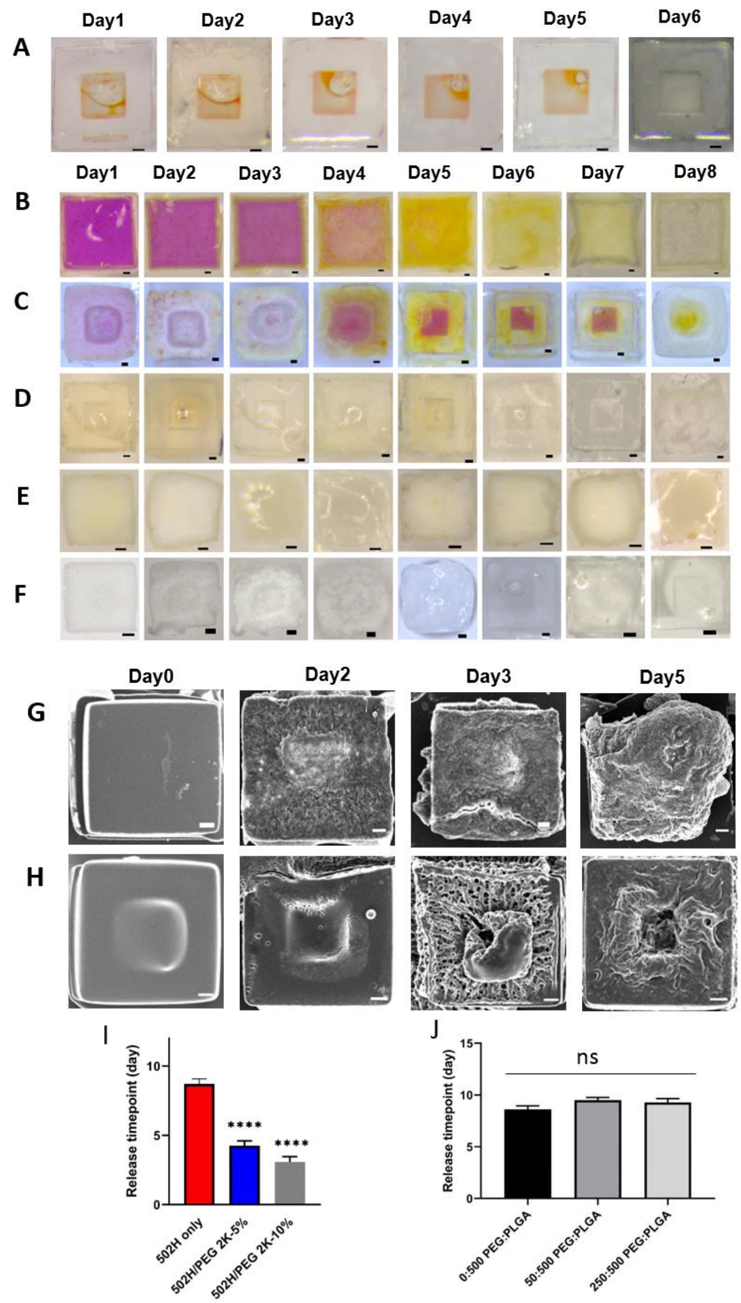

Figure 3.10: pH evolution in biodegradable core-shell microparticles.

(A) Water permeation into the core over time leading to change in the color of universal pH indicator loaded in the core. Color change over time in various groups, loaded with thymol blue (TB) in the cap, in (B) cap-only (pure PLGA) (C) full cap-base particles (pure PLGA cap) (D) full cap-base particles (PLGA/PEG cap) (E) cap-only (PLGA/PEG) and (F) full cap-base particles (no TB in cap), as the control group. Surface SEM comparison of change in the microstructure of core-shell microparticles with (G) PEG-free and (H) PEG-mixed (2kD PEG-5% (w/v)) caps upon incubation in buffer. Effect of addition of PEG to the PLGA in the cap on release timepoint in (I) PEG (2kD) physically doped into the cap PLGA or (J) PEG added through PEG-*b*-PLGA block to the cap PLGA

(PEG 2kD, PLGA 11 kD). Scale bars show 50 µm. Bases are made from slow-degrading PLGA (RG 756S), and except group A, the core is initially empty. PLGA used in the cap (not conjugated with PEG) is fast degrading (RG 502H). Error bars show SEM.

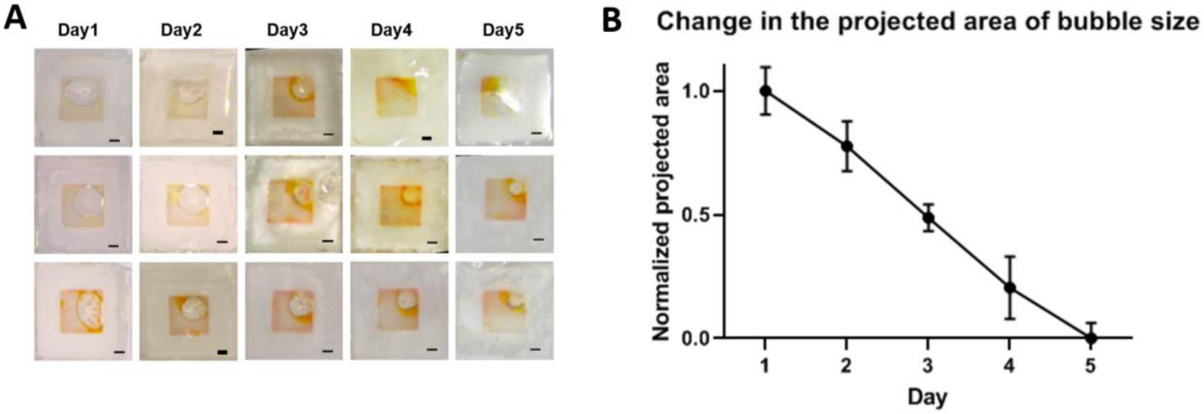

Figure 3.11. Diffusion of water into core-shell microparticles over the degradation

(A) Additional optical images showing permeation of water into the core-shell particles loaded with universal pH indicator in the core in three particles. (B) Quantification of projected area of the air bubble in particles over time (top view). Water partly permeates into the core even without the cap being fully porous. In the case of a cap made from RG 502H with a release timepoint of 8±1 day in vitro, water starts to fill the core at day 1 while completely filling the core at day 5. We observed the same behavior in high molecular weight PLGAs such that water starts to diffuse into the core days prior to the release timepoint. Permeation of water molecules into the core across the dense non-porous cap can be described using a solution-diffusion mechanism. Pronounced degradation of cap on the interface with water allows water molecules to diffuse to the core, but not the cargo to release out. Transport of water molecules into the core is further enhanced by higher internal osmotic pressure caused by accumulation of degradation products inside the core. Conversely, transport of cargo out into the buffer at the release timepoint can be facilitated mostly by formation of a network of interconnected pores across the cap as previously shown. Scale bars show 50 µm. Error bars show SEM (n=4-5).

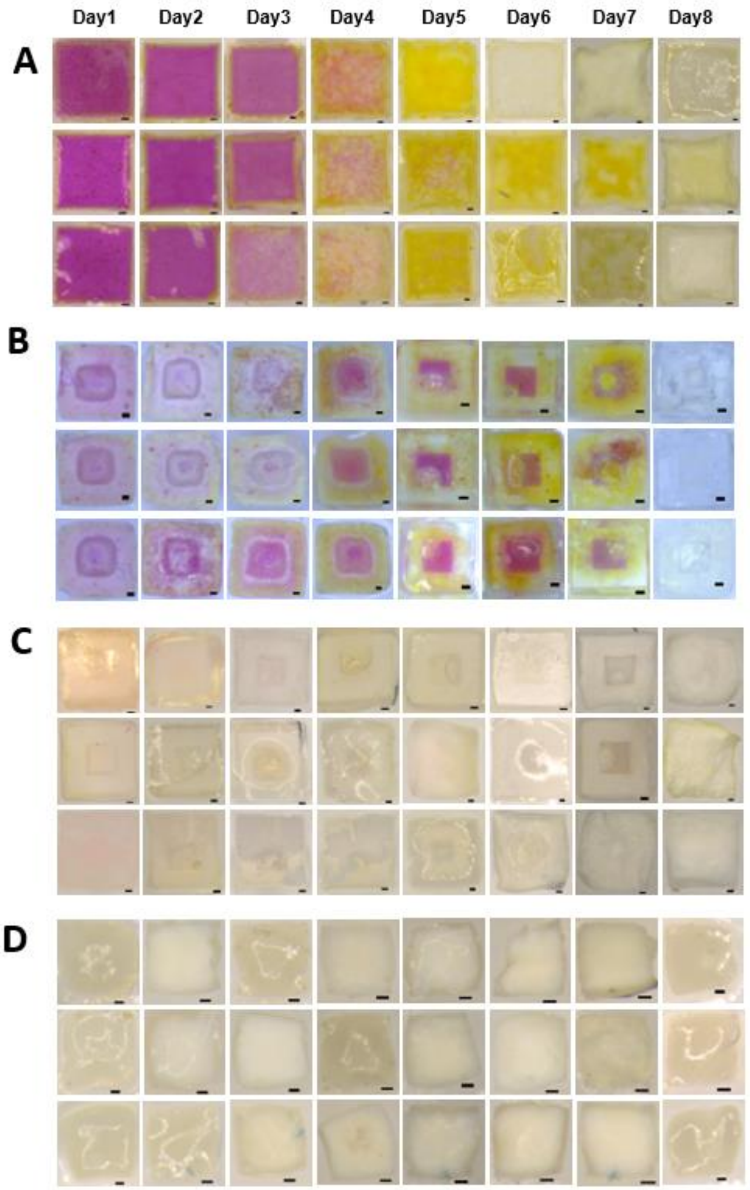

Figure 3.12: Additional optical imaging analysis of pH evolution in particles

Additional optical images illustrating color change upon degradation of different groups over time in (A) cap-only group loaded with thymol blue (caps made from pure PLGA), TB, (B) full cap-base particles (empty core) with TB mixed in the cap (PLGA), (C) full cap-base particles (empty core) with PLGA/PEG cap mixed with TB, and (D) PLGA/PEG caps mixed with TB. Scale bars show 50 µm.

We analyzed the normalized projected area (from the top view) of the cap in each group in the pH study (n=3-5) (**Figure 3.13**). The projected area (normalized by day 0) followed different trends, with PEG-free PLGA groups showing expansion, while caps containing PEG decreased in size over time. The extent of expansion or shrinkage was found to be a function of interfacial surface area between the cap and water (cap-base vs cap-only) and composition of the cap (PLGA vs PEG/PLGA). Full cap-base, PEG-free group demonstrated the highest expansion, reaching almost twice the initial size at day 7 & 8. The PEG-loaded cap-only group represented the most notable shrinkage by more than 50% of the initial size at day 4 onward.

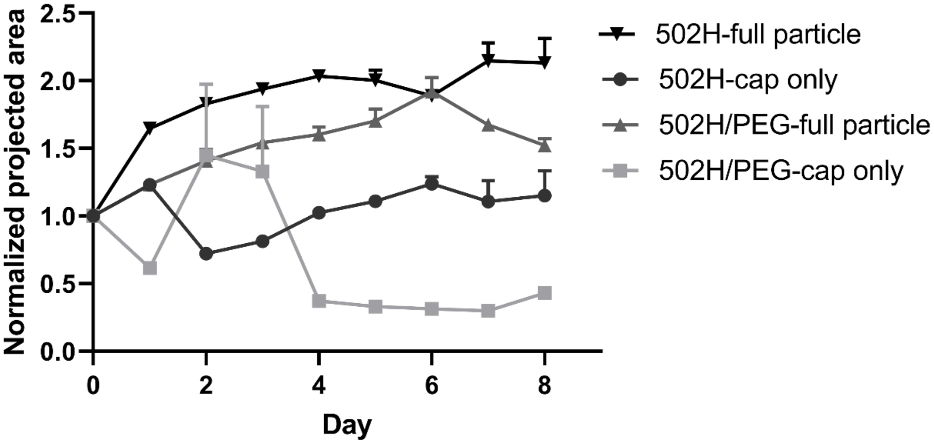

Figure 3.13: Evolution in the size of microparticle groups over time.

Change in the projected area of the cap (top view) in different groups in studying the pH change (n=3-5). Deformation of cap in different groups is dependent on boundary conditions (cap-only vs full cap-base) and hydrophobicity of the cap (presence or absence of PEG). Error bars show SEM.

To better understand the effect of PEG loading, surface SEM was used to visualize microstructural evolution of full cap-base particle with pure PLGA or PEG/PLGA caps in multiple particles (additional particles in **Figure 3.14**). As shown, the PEG-loaded group represented a more pronounced pore-formation on the surface combined with faster breakdown of the cap, being considerably peeled off the base at day 5. Conversely, the PEG-free group represented expansion with a less pronounced pore formation in comparison. We further realized that enhanced pore formation in particles with PEG-loaded cap led to earlier release of the cargo compared with particles with PEG-free cap (day 3 for 2kD and 4 for 20kD PEG/502H). But this observation held only when PEG was physically doped into the cap, not when a block copolymer PEG-b-PLGA with a PEG segment of similar MW (2kD) was used. Change in release timepoint in the latter was found statistically insignificant from the control group (PEG-free 502H).

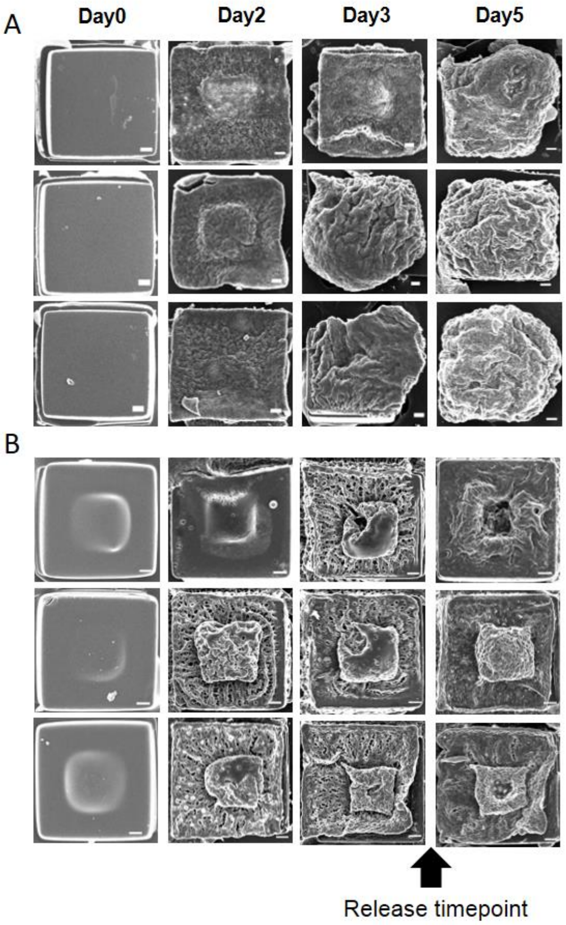

Figure 3.14: Additional SEM images showing pore-formation in PEG/PLGA loaded particles compared to pure PLGA caps.

Additional surface SEM images showing microstructural evolution upon degradation in core-shell microparticles capped with (A) pure PLGA (RG 502H) and (B) a mixture of PEG/PLGA (2 kD PEG:PLGA 50:500) in three particles. Scale bars show 50 µm.

3.3.4 Computational modeling of particle deformation

To reinforce our experimental understanding, a numerical multiphysics model based on theory of poroelasticity was constructed by using COMSOL® Multiphysics. The model coupled solid mechanics formulations to Darcy's law (flow in porous media) (**Figure 3.15**). Subsequently, we modeled 2D geometry of a cubic core-shell microparticle at the central cross section, with the same dimensions as in the experiments. During the simulations, the average vertical displacement in the cap (V_{mean}), as an indicator of cap deformation, was computed and compared (see supplemental method). Boundary conditions were specified as both cap and base made from porous linear elastic materials, with specified material properties such as elastic module (E), porosity (ε), and permeability (κ) (**Figure 3.15 C**). Two types of pressure were considered, external pressure applied on the cap (P_{out}) and an internal pressure in the core (P_{in}). It was also postulated that water enters from the edge of the cap (at a velocity of v_{in}) and enters the core (at a velocity of v_{out}) as qualitatively observed in the experiments. Structure of the meshed model was chosen as physically optimized. Additional assumptions were made to further enable the feasibility of the simulations, as described in the supplemental section.

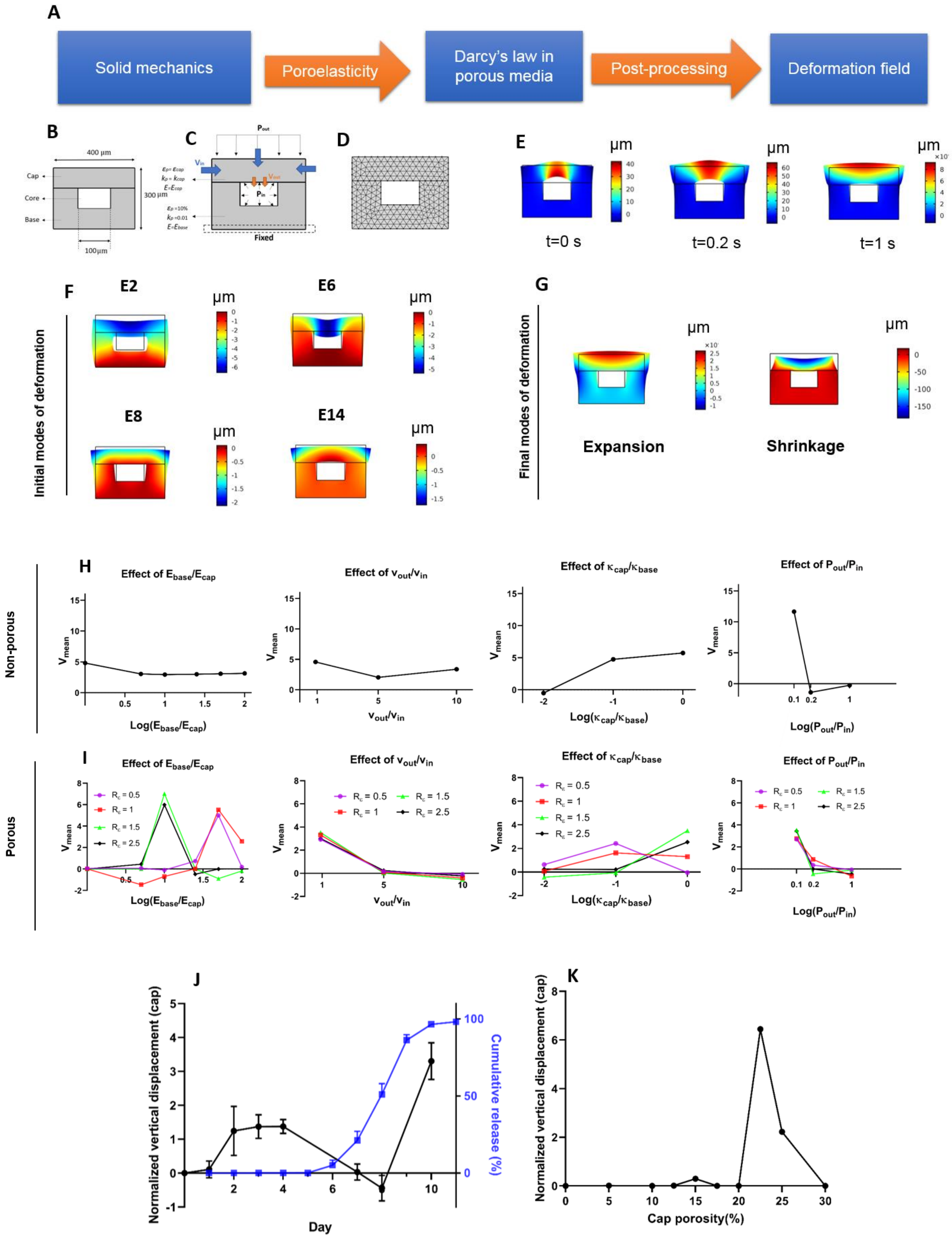

Figure 3.15: Computational modeling of deformation in biodegradable core-shell microparticles.

(A) Conceptual overview of the Multiphysics simulation approach. (B) Dimensions of the microparticle system simulated (C) Boundary conditions in the simulations. (D) Meshed geometry of the numerical model (E) Time snapshot of microparticle deformation. (F) Final modes of deformation for different numerical conditions (noted by E) from the design of experiment table in non-porous model. (G) Two dominant modes of deformation obsserved in the porous model () Effect of the numerical parameters on normalized vertical displacement in the cap in (H) non-porous solid mechanics model and (I) poroelastic model. (J) Experimental vertical displacement of the cap and comparison with cumulative in vitro release of AF647-labeled dextran from core (n=4). Release profile depicted here is averaged among four cargo molecular sizes studied. (K) Normalized vertical displacement of the cap as a function of cap porosity based on simulations. Error bars in J show SEM.

To study the effect of key parameters in poroelasticity on the particle deformation, an L18 orthogonal design of experiment (DOE) array was constructed based on four dimensionless parameters (**Table 3.1**). These parameters include 1) ratio of Young's modulus of base/cap ($R_E = E_{base}/E_{cap}$), 2) ratio of external/internal water velocity ($R_v = v_{out}/v_{in}$), 3) ratio of permeability of cap/base ($R_k = \kappa_{cap}/\kappa_{base}$), and 4) ratio of external/internal pressure ($R_p = P_{out}/P_{in}$). Simulations were performed for four different ratios of cap/base porosity ($R_\varepsilon = \varepsilon_{cap}/\varepsilon_{base}$), resulting in a total of 52 simulations. We investigated the deformed shape and vertical displacement of the cap (V_{mean}) as two main outputs in this study. A purely solid mechanics (non-porous) model and a full multi-physics model (porous) were analyzed. Comparing these models helped us understand how the effect of these parameters would change in absence and presence of pores in the system.

The deformation of the cap started from the center and progressed toward the edge and exterior parts of the cap. The non-porous model yielded multiple different mode shapes depending on simulation conditions. However, all mode shapes in the full poroelastic model followed two classes of deformation patterns, labeled as, shrinkage ($V_{mean} < 0$) or expansion ($V_{mean} > 0$). Next, the effect of the four dimensionless parameters on V_{mean} was investigated. Simulations revealed that non-poroelastic and poroelastic models displayed different deformation behaviors. In the non-poroelastic model, R_p was found as the most important factor, considerably influencing deformation of the cap, particularly going from R_p of 0.1 to 0.2. Simulated cap displacement reached a plateau at R_E of 5, and R_k of 0.1 in the non-porous model. These results could introduce microenvironment pressure (R_p) as the dominant factor controlling deformation of non-porous particles compared to polymer degradation, captured by change in elastic modulus (R_E) In the poroelastic model, the effect of the parameters depended on porosity ratio ($R\varepsilon$). In this model, R_E was found as the dominant factor among all porosity values studied. This could suggest material degradation is the dominant factor on deformation of the particles (compared to the microenvironment factors). Increasing parameters R_v and R_p, capturing the effect of microenvironment conditions affected particle deformation leading to a decrease and increase in V_{mean}, for all porosity ratios, respectively.

As the next step, we calculated the experimental equivalent of the vertical displacement of the cap, Vmean (**Figure 3.15 J**, normalized by mean), in cross sectional SEM images of microparticles over time (n=4). An image processing approach was followed to model cap as a deformed rectangle. Full description of the protocol for calculation of experimental V_{mean} can be found in following sections. The vertical deformation of the cap was found consisted of three phases, 1) an initial expansion (up to day 4), 2) followed by a shrinkage (day 4 to 8), and finally 3) a sudden expansion (day 8 to 10). We then compared cap displacement with the corresponding data on the release kinetic-- averaged across all cargo sizes studied in **Figure 3.8** for 4X core-100 µm cap particle design (**Figure 3.15 J**). It was observed that the secondary jump in the average vertical displacement of the cap (third phase in cap deformation) corresponded to onset of the pulsatile release.

Among 18 conditions simulated for 4 porosity values (**Table 3.1**), case 5 was found the closest to capture the overall behavior of experimental cap expansion (presented in the time domain) but in porosity domain. The criteria and assumptions for comparing simulations and experimental findings are presented in the supplemental file. Interestingly, we found a numerical porosity threshold (22.5%, core excluded) that led to a sudden jump (more than 6 times) in Vmean in agreement with the trend in the experimental observations. While the initial expansion/shrinkage phase observed in the experiments was captured with a lower peak in the numerical model (core excluded), the overall trend of three phases were captured successfully in the numerical model.

Sim. No.	**R_e**	**R_p**	**R_v**	**R_k**
1	**1**	**0.1**	**0.1**	**0.0001**
2	**1**	**1**	**1**	**0.001**
3	**1**	**10**	**10**	**0.01**
4	**5**	**0.1**	**0.1**	**0.001**
5	**5**	**1**	**1**	**0.01**
6	**5**	**10**	**10**	**0.0001**
7	**10**	**0.1**	**1**	**0.0001**
8	**10**	**1**	**10**	**0.001**
9	**10**	**10**	**0.1**	**0.01**
10	**25**	**0.1**	**10**	**0.01**
11	**25**	**1**	**0.1**	**0.0001**
12	**25**	**10**	**1**	**0.001**
13	**50**	**0.1**	**1**	**0.01**
14	**50**	**1**	**10**	**0.0001**
15	**50**	**10**	**0.1**	**0.001**
16	**100**	**0.1**	**10**	**0.001**
17	**100**	**1**	**0.1**	**0.01**
18	**100**	**10**	**1**	**0.0001**

Table 3.1. Details of the DOE used for numerical simulations.

Table of the orthogonal array (L_{18}) used for numerical design of experiment, implemented in simulations. Each condition was simulated for 4 values of cap/base porosity ratios (R_ε = 0.5, 1, 1.5, 2.5), yielding a total of 52 simulations. Case 5 was found as the most experimentally likely simulated condition.

3.4 Discussion

In this work, various tools from experimental and computational approaches were integrated to study the complex mechanism of degradation in biodegradable core-shell microparticles. A comprehensive study was conducted to investigate key factors controlling the mechanism of pulsatile release. It was demonstrated that pore formation and cap deformation were the two governing parameters that control the release kinetics. Due to independence of release profile and particle geometry within the range studied (100-500 µm particles), this approach can be applicable to a wide range of core-shell particle designs. The framework presented here can also be employed to systematically study complex degradation of future biodegradable biomaterials.

PLGA microspheres and their degradation has been studied over the past three decades [73, 75]. Although widely investigated, the underlying mechanism and functional impact of PLGA degradation is often dependent on the specific microstructure of the drug delivery system and cannot be expanded to other PLGA-based systems. In the system described in this work, core-shell microparticles, we observed an erosion behavior that deviated from degradation of emulsion-fabricated PLGA microspheres with pre-existing pores. PLGA has been widely recognized as a hydrolytically bulk degradable polymer in which pores are expected to develop throughout the entire polymer matrix upon hydrolysis [73-77]. For the core-shell particles studied herein, pore-formation was more pronounced on the edge of the cap due to higher interfacial surface area with water, leading to a regional degradation front on the edge of the particles. The locally degraded front eventually progressed throughout the entire particle (or particle cap), reaching the core, but rather slowly in order of days.

Interestingly, the pore formation followed a nonlinear trend, with porosity being similar on days 3 and 7 while drastically increasing on day 10 (**Figure 3.1**) for a particle with in vitro release of day 8 ±1. Interconnected pores led to formation of a path connecting the cargo to the outer environment, leading to pulsatile release. This pronounced degradation pattern near release timepoint was further supported by results from thermal/mechanical analysis showing a sudden drop in T_g, T_d, and E within days 8-10 (particularly at day 10). Formation of a tortuous network of pores within the PLGA matrix, facilitating release of drugs to the medium, has been postulated in the literature [75, 78]. Some studies also experimentally visualized hydrolysis-caused formation of interconnected pores across cross sections of PLGA microspheres, but without demonstrating release of the drug itself [67, 77]. This study further confirms release through path formation by providing direct visual evidence of release of a model macromolecule (10 kD-dextran) through the bulk of the PLGA matrix using EDS-SEM and OM.

This study further suggests particle composition (i. e. polymer molecular weight and end group), as opposed to size/morphology, within the size studied (~100-500 µm), dominates the release timepoint in core-shell microparticles. Uniquely, the delayed-release pulsatile release profile was preserved across all 25 different designs of microparticles studied. Size-independence of release timepoint from particle geometry (within ± 2 days in vitro), within the range studied, provides an advantage over existing drug delivery systems (e. g. hydrogels, microspheres). Accordingly, as long as composition of the cap stays the same, particles with different morphology can follow approximately the same release timepoint (within 2 days of difference). This could potentially allow for the physical design of the core-shell particles to be tailored to specific administration methods or therapeutic applications where a certain particle size or morphology is required.

As one of the key factors leading to release, this study qualitatively assessed microclimate pH change in the cap and base of core-shell microparticles. Various methods have been developed to quantify pH distribution in PLGA microspheres such as laser scanning confocal or two-photon microscopy [79, 80]. However, these techniques suffer from limitations on the detectable acid range (~ pH 2.0), and complexity of the protocol [79, 80]. The method presented here, based on incorporation of thymol blue, is a simple qualitative technique that covers a lower acidic range (≤ 1.2). It also provides visual understanding of pH distribution within relatively large (> 100 µm) PLGA-based particles.

The bi-phasic map of pH, representing higher pH on the edge compared to the center, has also been reported in PLGA microspheres [69]. The higher pH region on the edge, progressing to the center, can be attributed to diffusion-mediated transport of acidic products to the environment [69]. Over time, as the cap surface porosity increased, the portion of the less acidic front (yellow) increased until it covered the entire cap. Further comparison between full cap-base and cap-only microparticles also revealed that degraded PLGA matrix with lower pH tends to accumulate in the core and center of the cap over time. This accumulation of acidic products increases the osmotic pressure inside the particle and leads to expansion of the cap by attracting more and more water into the particle. The progressive swelling facilitated by pore formation in the cap further contributes to pulsatile release of the cargo potentially at a threshold porosity. The association between PLGA swelling and sudden release of the cargo has also been observed in PLGA microspheres [68].

Given the pore-mediated release mechanism, we then postulated that addition of PEG, a widely-used pore-forming agent, can potentially alter the release kinetics and neutralize accumulation of acidic products [79, 81, 82]. We observed that blending PEG as an additive into the cap resulted in earlier release compared to pure PLGA, while blending PEG-b-PLGA block copolymer with PLGA had no effect on the release time. PEG, especially at the molecular weight used (2 kD), when directly blended with PLGA, serves as a porogen [81, 82]. Upon interacting with water molecules, PEG dissolves and leaves the PLGA matrix, creating voids within the cap, as shown by surface SEM. Additionally, the presence of these voids within the matrix creates larger water pathways through the particles which combined with higher hydrophilicity leads to enhanced water uptake and hence faster hydrolysis of PLGA. This enhanced water intake can also justify higher pH range (pale yellow) in PEG-doped PLGA particle groups compared with pure PLGA. Pronounced pore formation can enhance clearance of acidic products out to the buffer by increased water permeation. Conversely, when PEG is tethered to PLGA (PEG-b-PLGA), the degradation would be dominated by swelling and higher water uptake, rather than pore formation. Swelling of PEG segment at 2 kD, used here, is likely not high enough to change the release time. The PEG domains in PEG-b-PLGA are protected against water interactions due to increased protection by hydrophobicity of PLGA.

To study the effect of parameters not captured in the experiments, a multiphysics numerical model was developed. Advanced computational tools are becoming increasingly important in studying biomedical systems in recent years [14, 39, 41,42]. To our knowledge, this is the first study to utilize theory of poroelasticity to numerically model deformation in a polymeric biomaterial. Studying the parameters in dimensionless form enables broader insights into the behavior of the system. The design of experiment approach also has been successfully utilized for studying complex engineering systems [33-39, 83]. This approach helps optimize the number of required experiments to systematically study the model. The numerical results in the porosity domain matched the trend of experiments in the time domain. They both pointed to the presence of three modes of cap deformation: i) an early expansion, followed by subsequent ii) shrinkage, and finally iii) a sudden expansion attributed to onset of the pulsatile release. Interestingly, we also observed decreasing the ratio of elastic modulus of cap to base (increasing R_E) leads to a similar sudden expansion of the cap, after a certain threshold, depending on porosity of the cap. In this study, with the assumption that elastic module of the base remains always greater than the cap, it can be deduced that increasing R_E captures decrease in the elastic modulus of the cap upon hydrolysis. Accordingly, increase in R_E can capture increased degradation of particle cap over time. This agrees with numerical results derived from increasing porosity, indicating a certain threshold for RE after which the cap experiences a sudden expansion.

Numerical results also demonstrated that increasing R_P led to pronounced expansion of the cap (for $R_P>1$). As shown, sudden expansion of the cap was concomitant with the release of cargo, as also reported in PLGA microspheres [68]. Therefore, cargos in which osmotic pressure outweighs hydrostatic pressure ($R_P>1$) are expected to release earlier due to increased cap expansion. The extent and sources of this effect need further examination in future studies. In this regard, water permeation into the core before release timepoint can also contribute to additional pressure in the core, generating a pressure gradient from the core toward the buffer. This pressure gradient can be another cause of cap expansion, in addition to factors already mentioned. As higher molecular weight PLGAs resist water permeation, they are expected to release the cargo at a later timepoint, as also demonstrated in the experiments. The current Multiphysics model can be used to provide a roadmap toward modeling deformation of PLGA-based drug delivery systems in future studies.

Collectively, the mechanism of pulsatile release in biodegradable core-shell microparticles can be triggered by hydrolysis of PLGA molecular chains. The hydrolysis reactions lead to cleavage of PLGA molecular chains, captured by decrease in T_g, T_d, and E of particle cap. Cleavage of PLGA molecular chains over time also leads to pore formation, and accumulation of acidic products at the core or center of the cap. All these factors then contribute to cap deformation through intermediate processes (e.g. osmotic pressure caused by drop in pH or deformations caused by poroelasticity of the cap as shown in **Figure 3.15**). Cap deformation (expansion or shrinkage) and pore formation are two key factors that eventually lead to pulsatile release from core-shell particles at a threshold porosity/expansion ratio.

Overall, this study aimed to use various experimental and computational tools to study mechanism of pulsatile release in biodegradable core-shell microparticles. To the best of our knowledge the current work is the first to integrate multiple tools from experimental and computational models to study pulsatile release kinetics from biodegradable microparticles. Results of this study not only can provide insights into mechanism of pulsatile release, but also enhance general understanding of PLGA-based biomaterials. Further, they can aid in design and fabrication of next-generation biomaterials and drug delivery systems for various drug delivery applications.

3.5 Materials and Methods

3.5.1 Fabrication of biodegradable core-shell microparticles

3.5.1.1. SEAL-method

Core-shell microparticles were fabricated using a slightly modified version of the recently developed multi-layer microfabrication technique termed SEAL [9]. Full description of the fabrication process can be found in [9,10]. Briefly, positive master molds for caps and base were fabricated using SU-8 lithography, made by Front Range Photomask (AZ). Films of pure PLGA or mixed with other additives were pressed into negative molds made from Polydimethylsiloxane (PDMS), (Sigma-Aldrich) for particle caps and bases. An additional Teflon layer was used to cover film in the PDMS to retain PLGA in the molds for the caps array. The bases contained a cubic hollow cavity (core) which was filled in multiple cycles with the cargos of interest by a high-precision piezoelectric picoleter dispensers, namely, BioJet Ultra picoliter dispensing instrument (BioDot, CA, USA) for low viscosity cargos and CellenONE (Scienion AG, Berlin) for high viscosity cargos. Filled array of bases on the glass slide were then aligned and sintered with the corresponding PLGA caps under microscope using a photomask aligner (MA4, Karl SUSS) or a custom-made, lab-developed mask aligner device both equipped with a Peltier heater for simultaneous alignment and sealing. The resulting core-shell microparticles were handled/cut using tweezers and razor blade. Various PLGA powders were purchased from Evonik and PolySciTech. Microparticles in this study were fabricated from different cap and base PLGA Resomers. Details of particle design and the amount of cargos loaded into the core in each experiment can be found in supplemental data 1. Unless otherwise stated, the base layer was made from high MW PLGA Resomer® RG 756S. Microparticles with blended caps studied were fabricated using films made from a mixture of different PLGAs blended at a given ratio (dissolved in acetone). Microparticles studied were fabricated by nano-resolution 3D printing (NanoScribe) at Center for Nanosystems (CNS), Harvard University as described in the following.

3.5.1.2 NanoScribe additive manufacturing (NanoScribe)

Particle geometries were designed using SketchUp and DeScribe software. Prints were made on a Photonic Professional GT Nanoscribe 3D Lithography system using DiLL method with IP-S photoresist. Prints were developed in propylene glycol methyl ether acetate (PGMEA) and isopropanol according to the manufacturer's instructions and dried for 30 min on a hot plate at 90°C.

Nanoscribe prints were coated with silane in a desiccator for 30 min prior to molding. Polydimethylsiloxane (PDMS) was prepared with a 7.3:1 ratio of base-to-crosslinker and centrifuged for 15 min at 5000 rcf. The PDMS was poured over the mold and degassed under vacuum for 60 min. This was cured overnight at 60°C. Some molds were found adequately rigid after these steps, however in some cases additional processing was found necessary described as follows.

The preliminary PDMS mold was again coated with silane under vacuum for 30 min. The mold was filled with NOA Optical Adhesive 61 (Norland Products, Cranbury, NJ). This was degassed under vacuum for 60 min, followed by UV curing for 30 min. The UV mold was then baked at 120°C for an additional 60 min to prevent off-gassing of any residual adhesive that could disrupt the PDMS molding process. Further working PDMS molds were constructed off the UV master using the above PDMS Mold protocol.

3.5.2 Microparticle imaging and image analysis

SEM and EDS-SEM were performed using a JSM-5600LV SEM (JEOL, Tokyo, Japan) with an acceleration voltage of 5 to 10 kV. Samples were initially coated with a thin layer of Au/Pd using a Hummer 6.2 sputtering system (Anatech, Battle Creek, MI) and then imaged. EDS was performed in the dark field, and both SEM and EDS-SEM were performed at high vacuum settings. Samples for cross sectional analysis were first frozen by liquid nitrogen, and then cut under an optical microscope. Iron(II) sulfate heptahydrate (FeSO4. 7H2O) was purchased from Sigma-Aldrich and dispensed (100 ng) into 4X-core particles using cellenOne picolitre dispenser. Nano-resolution x-ray CT reconstructs (resolution: 0.38-0.45 µm) were obtained at the Biotechnology Resource Center of Cornell University. Nano-CT imaging was performed using ZEISS/Xradia Versa 520 X-ray Microscope. The three cross sections depicted in for each particle were selected to be equidistant (50-60 µm apart). Reconstruction of nanoCT scans were performed with software Avizo (Thermo-Fisher, USA). All 2D image analysis including porosity measurements was performed by ImageJ.

3.5.3 Release kinetics measurement

In all release measurements in this study, an individual particle was placed into 125 μL of phosphate-buffered saline (PBS) in a low-bind microcentrifuge tube (Eppendorf, Hamburg, Germany), incubated on a shaker (100 rpm) at 37°C. Before starting the experiments, tubes were micro-centrifuged to make sure particles completely sink inside the buffer in the tubes. All release measurements were performed daily for at least six particles per group (mostly 10), by analyzing the supernatant fluorescence using a Tecan Infinite M200 spectrophotometer (Männedorf, Switzerland). The excitation/emission wavelengths (nm) of 650/680 was used for all AF647-labeled dye detection. Results were normalized to the total cumulative release. For each measurement, 100 μL of supernatant was taken from the tube (after gently resuspending the buffer multiple times). Supernatant was replaced with 125 μL of fresh PBS after each measurement. Release of four different types of AF647-labled fluorescent dyes loaded in the core was analyzed in this study. Dextran-free and 10kD-dextrain groups were purchased (Thermo Fisher Scientific, Waltham, MA). 70kD and 2000 kD groups were manually labeled with AF647. Briefly, dextran was dissolved at 10 mg/mL in a pH 8 buffer and then added 10-fold relative to calculated amines in N-hydroxysuccinimide (NHS)-conjugated AF647 dye. The resulting mixture was left to react 2-4 h at room temperature and then dialyzed with a cassette. The resulting mixture was spin filtered using ZEBA Spin Desalting Columns.

3.5.4 Fabrication of microparticles with PEG-loaded cap

PEG was purchased from Sigma-Aldrich, Inc. (St. Louis, MO). A certain amount of PEG (pure or PEG-b-PLGA) was added to acetone/PLGA mixture. In case of pure PEG, 50 or 100 mg of 2kD PEG was mixed with 500 mg of PLGA and added to acetone subsequently. The resulting PEG/PLGA/acetone mixture was magnetically stirred, sonicated and slightly heated up (up to 40ºC for 30 min) until a homogeneous solution (in acetone) was achieved. Films made from PEG/PLGA were fabricated by first pipetting the solution on a Teflon-coated glass slide, and then sliding the slide under a doctor’s blade, followed by overnight drying on hot plate at 45°C. The resulting films had an average thickness of 40-70 μm. PEG-b-PLGA loaded caps were fabricated similarly except, PEG-b-PLGA (50 mg or 250 mg) was used instead of pure PEG. The resulting films were used to fabricate the microparticle caps using micromolding, as previously described.

3.5.5 Encapsulation of pH indicators

300 ng of universal pH indicator (pH-indicator solution pH 4.0 - 10.0, Sigma-Aldrich, Inc.) was dispensed (at concentration of 1 mg/mL) into the core of microparticles by high-precision picolitre dispenser device, BioDot. 20 mg of Thymol blue (Sigma-Aldrich, Inc.) was added to 1 mL of the PLGA (50% w/v)/acetone solution film precursor. The resulting mixture was sonicated for 1 h, then used to fabricate polymer films, and subsequently microparticle caps, according to the process previously described.

3.5.6 Numerical model in COMSOL and design of numerical simulations

A total of 52 simulations were performed (18 based on numerical DOE for 4 different porosity ratios). All simulations in this study were conducted using COMSOL Multiphysics ® V5.2 (Burlington, MA). Solid mechanics module and poroelasticity module were coupled during simulations. Accordingly, the solution resulted from simulation of the solid mechanics model was the input to the porous model as initial condition. The numerical design of experiment was designed and analyzed by software Minitab (Chicago, USA) based on an L18 Taguchi orthogonal array repeated for various levels of cap/base porosity ratios. Table S1 summarizes the 18 conditions studied. The underlying mathematical formulation for simulations can be found in the supplemental file.

3.5.7 Thermal analysis

Differential scanning calorimetry (DSC) analysis was performed using Perkin Elmer DSC 8000 System under nitrogen flow (50 mL /min). For DSC analysis a heating-cooling-heating cycle was applied from -80oC to 80oC, with heating and cooling rate set at 10oC/min in order to determine the glass transition (T_g) temperature of the tested polymer blends. Furthermore, thermogravimetric analysis (TGA) was conducted in a Pyris 1 Thermogravimetric analyzer with heating rate at 20 °C/min from 50 to 600 °C under nitrogen flow (20 mL/min). Degradation temperatures (T_d) of tested polymer samples were determined at the maximum rate of weight loss. All sample analyses were performed in at least triplicate. Thermal analysis was performed on PLGA 502H films submerged in PBS, incubated at 37°C on shaking incubator (100 rpm) sampled at different timepoints.

3.5.8 Mechanical compression analysis

Samples were subjected to compression testing using a material testing machine (Instron 5943, Norwood, MA). Samples were set up such that a single microparticle was underneath the compression clamp. To evaluate elastic modulus two extension rates were employed – 0.09 mm/min (days 0-8) and 0.015 mm/min (days 9 & 10). Elastic modulus was defined by measuring the slope of the linear portion of the curve immediately prior to maximum load. Mechanical tests was performed on a cubic solid (without core) microparticle (350×350×320 µm) made from the fast-degrading PLGA (RG 502H), incubated at 37ºC in PBS (shaking incubator, 100 rpm) and sampled at different time intervals, to model degradation of the cap in core-shell particles.

3.5.9 Statistical analysis

Statistical test between two groups were performed based on student t-test. A p-value of less than 0.05 was considered statistically significant. Statistical analyses were performed in GraphPad Prism (GraphPad Software, La Jolla, CA).

3.5.10 Mathematical framework

In this study, Poroelasticity multiphysics node was used to capture the effect of fluid flow in porous structure (core-shell particle) on its mechanical deformation. Generalized form of continuity equation combined with Darcy's law yields the following equation:

$$\rho \mathrm{S} \frac{\partial \mathrm{p}}{\partial t} + \nabla \cdot \rho [- \frac{\kappa}{\mu} \nabla p] \; = \; Q_m \qquad \text{(3-1)}$$

Where ρ is the fluid density (kg/m3), p is the pore pressure (Pa), K is the hydraulic conductivity (m/s), ε_{Vol} is the volumetric strain of the porous matrix, Q_m is a mass source term (kg/m^3·s), α_B is the Biot-Willis coefficient (equal to 1 for most soft materials and in this study), k is the permeability of the porous medium (m^2), μ is the fluid's dynamic viscosity (Pa.s) , and S is the poroelastic storage module which can be approximated in the linear form by:

$$S = \epsilon_p x_f \quad (3\text{-}2)$$

In which x_f is the fluid compressibility (equal to 4 ×10^{-10} 1/Pa) and ϵ_p is the matrix porosity (unitless). The porosity is defined as the ratio of the control volume that is occupied by pores, to total control volume. The governing equation for the poroelastic material model is defined as:

$$-\nabla \cdot \sigma = \rho g \quad (3\text{-}3)$$

here, σ is the stress tensor, ρ is the total material density, and g acceleration of gravity (m/s^2). For an isotropic porous material under plane strain condition in 2D (x-y), the components of stress tensor can be simplified as follows:

$$\begin{bmatrix} \sigma_{xx} \\ \sigma_{yy} \\ \sigma_{xy} \end{bmatrix} \equiv \frac{E}{(1+v)(1-2v)} \begin{bmatrix} 1-v & v & 0 \\ v & 1-v & 0 \\ 0 & 0 & 1-2v \end{bmatrix} \begin{bmatrix} e_{xx} \\ e_{yy} \\ e_{xy} \end{bmatrix} - \begin{bmatrix} \alpha_B p & 0 & 0 \\ 0 & \alpha_B p & 0 \\ 0 & 0 & \alpha_B p \end{bmatrix} \quad (3\text{-}4)$$

Where E is the Young's modulus (Pa) and v is the Poisson's ratio of the drained porous matrix. The term $\alpha_B p$ represents the fluid-to-structure coupling expression, which is added by the Poroelasticity multiphysics node. Within small deformations, terms e_{xx}, e_{yy}, and e_{xy} describe planar strains which can be written in terms of vertical (V) and horizontal displacements (U) as:

$$e_{xx} = \frac{\partial U}{\partial x} \quad (3\text{-}5)$$

$$e_{yy} = \frac{\partial V}{\partial y} \quad (3\text{-}6)$$

$$e_{xy} = \frac{1}{2}\left(\frac{\partial U}{\partial y} + \frac{\partial V}{\partial x}\right) \quad (3\text{-}7)$$

$$e_{xy} = e_{yx} \quad (3\text{-}8)$$

$$e_{xz} = e_{yz} = e_{yz} = 0 \quad (3\text{-}9)$$

During simulations, the above equations are simultaneously solved to find the displacement field (*U, V*) within the poroelastic material.

3.5.10.1 Cap vertical displacement calculation

Experimental approach

To calculate the average vertical displacement in cross sectional SEM images a protocol was followed. First, the area of the cap at day i (A_i) was calculated from SEM images (n=4). The cap (deformed or non-deformed) was modeled as a rectangle with width b as wide as particle base (400 µm). The height of the rectangle was then calculated as follows:

$$h_i = \frac{A_i}{b} \quad (3\text{-}10)$$

The height of particle at day 0 (h_0) was then subtracted from the height of the rectangle at each day (h_i) to calculate the vertical cap displacement relative to non-degraded particle:

$$V_{exp,i} = h_i - h_o \quad (3\text{-}11)$$

The resulting number was normalized by average of vertical displacement across all timepoints-particles

$$\overline{V}_{exp,i} = \frac{V_{exp,i}}{V_{mean,exp,i}} \quad (3\text{-}12)$$

3.5.10.2 Numerical approach

A similar procedure was followed for numerical vertical displacement of the cap obtained from simulations. The comparison was done among different ratios of cap/base porosity values (R_ε) instead of timepoints. Numerical vertical displacement for each set of simulated condition (out of 18) was normalized by dividing vertical displacement obtained for each porosity to the average value of vertical displacement across all porosity values, within a given simulation set, as follows:

$$\overline{V}_{num,\varepsilon i} = \frac{V_{num,\varepsilon i}}{V_{mean,num,\varepsilon i}} \quad \text{(3-13)}$$

In which $V_{num,\varepsilon i}$ is the vertical displacement for porosity value $\mathcal{E}_i$ (calculated from simulations), and $V_{mean,num,\varepsilon i}$ represents average vertical displacement across all porosities for a given simulation set (i.e. each row in **Table 3.1**).

3.5.10.3 Assumptions in the numerical modeling

Out of 18 conditions simulated (Table S1) the resulting vertical displacement of the cap was evaluated to find the best condition that mimics the experiments. The condition which could capture all three stages observed in experiments (in the same order) was chosen as the most likely simulation condition. These three phases in cap deformation include 1) initial expansion ($\overline{V}_{exp,i} > 0$), followed by 2) shrinkage ($\overline{V}_{exp,i} < 0$), and eventually 3) sudden jump in expansion of the cap ($\overline{V}_{exp,i} \gg 0$). The order of magnitude in numerical simulations were also taken into consideration. Change in simulated cap displacement of the most likely simulation was mapped as a function of cap/base porosity and compared to experimental cap displacement as a function of time ($\overline{V}_{exp,i}$). Additional assumptions were made to enable convergence of the simulations as follows:

1) Elastic module of base is always greater than cap (base does not degrade within the time scale of cap degradation).
2) Increase in ratio of base/cap Young's module is equivalent to increase in degradation of particles over time.
3) Increase in particle porosity can be equivalent to increase in incubation time and degradation. In other words, porosity of the particles increases over time
4) The following constants were considered: base porosity

- Base Porosity =0.1

- Base Permeability=1×10^{-2} m^2
- Density for both cap and base=1340 kg/m^3 (density of PLGA R:G 50:50)
- Poisson ratio =0.3
- E_{cap} =5 MPa (constant) & E_{base} is variable

CHAPTER

4

VACCINATION-TRACKING MICRONEEDLES

This chapter is mostly reprinted from publication “Biocompatible near-infrared quantum dots delivered to the skin by microneedle patches record vaccination.” cited in [13]. This chapter focuses on a biocompatible technology for on-patient medical record tracking. Such technologies can be particularly advantageous in remote locations with poor access to healthcare providers and countries with low-resource healthcare settings. The technology is based on dissolvable microneedle patches delivering a highly photostable fluorescent dye (quantum dots). The dye is invisible to naked eyes but visible under customized NIR detection devices (attachable to smart phones). Therefore, by encapsulating dyes in various microneedle arrays, it would be possible to achieve various patterns transferred to the skin via microneedle insertion (**Figure 4.1**). Each pattern can therefore be used to decode information on administration of a certain vaccine/dose, co-delivered with the dye through the patch. A special camera can be attached to common smart phones to provide such capability. A schematic illustration of the method is shown in **Figure 4.1**. Encapsulation of the dye inside polymeric microparticles allows for extended signal detection for up to simulated five years. This chapter focuses on two important aspects, namely, 1) computational modeling and optimization of various microneedle designs and 2) development of a machine-learning based algorithm for automated pattern classification.

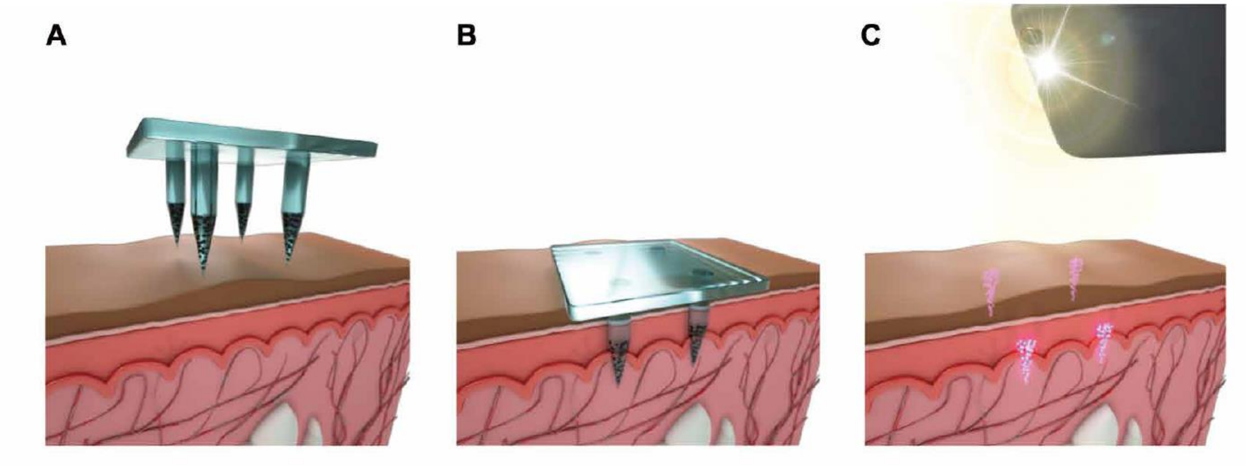

Figure 4.1 Schematic of fluorescent probe delivery and detection.
(A) Fluorescent microparticles are distributed through an array of dissolvable microneedles in a unique spatial pattern. (B) Microneedles are then applied to the skin for two minutes resulting in dissolution of the microneedle matrix and retention of fluorescent microparticles. (C) A near-infrared LED and adapted smartphone are used to image patterns of fluorescent microparticles to determine the treatment previously administered, adapted from [13].

4.1 Computational modeling

4.1.1 Introduction

In recent decade, microneedle-based drug delivery has been recognized as an effective method of transdermal drug delivery and a potential alternative for hypodermis needles, especially for controlled vaccine delivery [84,85]. Despite promises of this new technology, microneedle-based drug delivery to deeper layers of skin such as dermis and hypodermis, is still facing serious challenges [84-86]. Design of microneedles to reach deeper layers of the skin could be challenging, requiring extensive optimizations. In such cases, an excessively long shaft would lead to increased risk of buckling as well as greater maximum bending stress in the microstructure. Fine-tunning the material properties is not always feasible due to limitations in the range of materials that could offer favorable biocompatibility and biodegradation characteristics. As a result, microneedle geometrical parameters such as diameter, and length should be carefully designed to address both efficient drug delivery (e. g. maintaining stability of the vaccine) and mechanical stability, to reach out to deeper layers of skin (e. g. epidermis and dermis).

Despite significant advances in recent microfabrication technologies, less has been done to acquire a systematic understanding of the effect of individual design parameters on mechanical performance of microneedles [87]. Finding the best geometry of the microneedles over a wide range of design options could be challenging. For example, a large microneedle aspect ratio would lead to deeper penetration into the skin, but higher risk of buckling failure and pronounced induced pain at the site of application. A similar trade-off approach should be taken into consideration when thinking about design of flange-like base for improved stability of microneedle shaft. While it could decrease maximum bending stress created in the structure, such components would add to the final cost and manufacturing complexity. Also, it would require revisiting the overall array design as they would change the interspacing pattern between each pair of adjacent microneedles.

One of the most important aspects in design of microneedles, is their ability to resist mechanical stress, deflection and displacement upon insertion into skin layers. An ideal microneedle structure should not mechanically fail under bending and axial stresses acting on the structure when being pierced into epidermis and dermis. Moreover, it should remain structurally stable throughout the entire course of application. Finite element method (FEM) has been emerged as a powerful tool for design and optimization of mechanical structures. Finite element method (FEM) is one of the major tools in design and optimization stages of engineering devices, particularly in detailed design steps. FEM-based simulations have been widely used in micro and macroscale analyses [39, 40]. When coupled with state-of the art statistical tools, importance of FEM simulations become even more considerable. In fact, results from parametric FEM-based analyses could be used as a database for further extensive statistical studies such as sensitivity analysis or multi-objective optimization. Such an approach would add an extra level of reliability and robustness to the design process, as it is based on not only numerical techniques but also strong analytical tools.

In the computational modeling in this chapter, we utilized FEM to optimize geometry of the microneedle used for transdermal drug delivery. We follow two approaches, namely, a) optimization by studying performance of 50 different microneedle designs in terms of various mechanical properties, and b) a parametric study on a more comprehensive microneedle model based on more than 1000 designs.

4.2 Model optimization

The following section is reprinted from publications “Multi-objective Optimization of Microneedle Design for Transdermal Drug Delivery" cited in [90], as well as “Biocompatible near-infrared quantum dots delivered to the skin by microneedle patches record vaccination.” cited in [13].

4.2.1 Theoretical framework

When pierced into the skin, microneedle structures undergo three major types of loading, namely, bending, axial, and buckling loading. To engineer a reliable microneedle structure, therefore, it is necessary to accommodate structural safety considerations in view of all these types of loadings. The criteria for bending and axial loadings are characterized by maximum deflection in the structure as well as maximum stress (usually von Misses stress) under bending and axial loading. To assess stability of the structure under buckling, a factor termed as critical load factor is calculated. This factor is in fact the ratio of the critical load, above which the microneedle will experience instability, to a given applied load. Critical buckling load factor is thus defined as:

$$\lambda = \frac{P_{critical}}{p_{applied}} \quad (4\text{-}1)$$

As a result, it is desirable to design the microneedle geometry and material to maximize the critical load factor for a given applied load. Critical Euler’s load for buckling ($P_{critical}$) is also defined as:

$$P_{critical} = \frac{\pi^2 EI}{(KL)^2} \quad (4\text{-}2)$$

In which *E* is the modulus of elasticity, *I* is the minimum area moment of inertia of cross section of the microneedle structure, *L* is unsupported length of the column, and *K* is the column effective length factor depending on the boundary conditions.

Furthermore, according to Euler–Bernoulli beam theory, bending stress of the microneedle structure, usually modeled as a beam, in each cross section could be described by:

$$\sigma_{bending} = \frac{Mz}{I} \quad (4\text{-}3)$$

Where *M* is the bending moment, *z* is the distance from neutral axis, and *I* is the area moment of inertia of that cross section.

4.2.2 Method

In this study, structural mechanics module from COMSOL Multiphysics ® version 5.3 is utilized to perform the above-mentioned analyses using an FEM approach. Microneedle structure was numerically modeled using a linear elastic constitutive material model with elastic modulus of 1.7 GPa obtained from tensile testing experiments (1.7 ± 0.3 GPa, n=8), and Poisson's ratio of 0.45. To this end, Structural Mechanics Module from COMSOL Multiphysics ® version 5.3 was utilized, and a physically controlled, extra fine mesh size setting was selected for all simulations. Microneedle structure was optimized based on two parameters, namely, the ratio of the cylindrical part to the overall length of the shaft, termed as alpha, as well as the shaft diameter (**Figure 4.2**). Total length of the microneedle shaft (x+y) was considered constant equal to 1500 µm. Parameter alpha was calculated as follows:

$$alpha = \frac{x}{x+y} \quad (4\text{-}4)$$

Subsequently, performance of 50 designs, with diameters ranging from 100 µm to 300 µm, and parameter alpha from 0 to 0.9 was evaluated regarding six criteria. These included maximum microneedle displacement, and maximum von Mises stress induced in the structure under axial, and bending loadings, critical buckling load factor, as well as maximum theoretical deliverable drug volume. A higher critical buckling load factor represented higher stability under a buckling load. Additionally, theoretical deliverable drug volume was calculated equal to the volume of top half of the solid microneedle shaft.

To perform buckling simulations a method based on [88] was used. To this end, microneedle tip was fully constrained, and a total downward load of 5 N was applied to the base center, while microneedle was free to move only along the shaft axis. To perform axial loading simulations, a pressure of 3.18 MPa, equal to the skin penetration stress was applied to the tapered region in axial direction (along the shaft). Bending simulations were conducted by applying a lateral total load of 20mN to the tapered region, similar to the method employed in [89]. All degrees of freedom of the microneedle base were fully constrained in both axial and bending loading analyses. Maximum von Mises stress, and maximum displacement in the structure were obtained from the axial and bending load analyses, whereas the critical buckling load, representing the stability of structure against buckling, was calculated from the buckling analysis. A higher value of critical buckling load represents higher resistance against mechanical instability. An overview of the boundary conditions used for the three loading conditions is depicted in **Figure 4.2** [90].

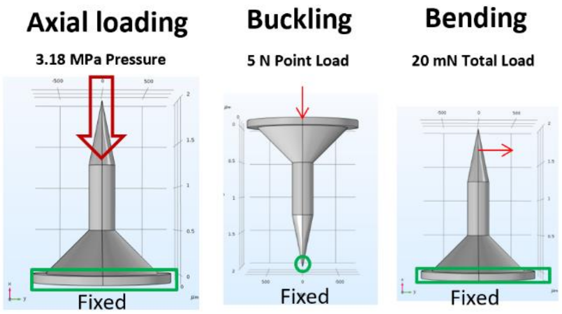

Figure 4.2: Specified boundary conditions for each type of analysis, reprinted from [90].

4.2.3 Results and discussion

Performance of all 50 designs were evaluated in terms of the six objective functions described earlier as demonstrated in **Figure 4.3**. Evidently, increasing needle dimeter decreased both the maximum stress and displacement in the structure. It also improved the critical buckling load factor. Increasing parameter *alpha*, in general, represented mixed trends, but it ultimately contributed to higher deliverable drug volume and improved buckling stability. Nevertheless, increasing *alpha*, led to increased maximum bending stress. Effect of microneedle tip angle, changing with parameter alpha, on pain perception is reported to be insignificant [91]. However, there is no systematic study on the effect of microneedle diameter on pain influence. Studies on hypodermic needles generally pointed out to an inverse relationship between needle diameter and the pain perception [92-94]. Simulations on the other hand pointed out to insufficient mechanical resistance for 100, and 200 µm dimeter designs, both under bending and axial loadings. Considering a trade-off between pain perception and mechanical stability, as well as deliverable drug volume, we selected a microneedle with diameter 300 µm as the optimum design. Increasing parameter *alpha* decreased maximum stress and displacement under axial loading, also increased theoretical deliverable drug volume, however, it increased maximum stress under bending. Moreover, the maximum displacement under axial loading reached a minimum only within alpha 0.3-0.5 and increased with increasing *alpha*. With these considerations, a value of *alpha* equal to 0.5 was selected as the optimum value. Ultimately, a design with a diameter and *alpha* equal to 300 µm, and 0.5, respectively, was considered as the optimum design and further selected for manufacturing.

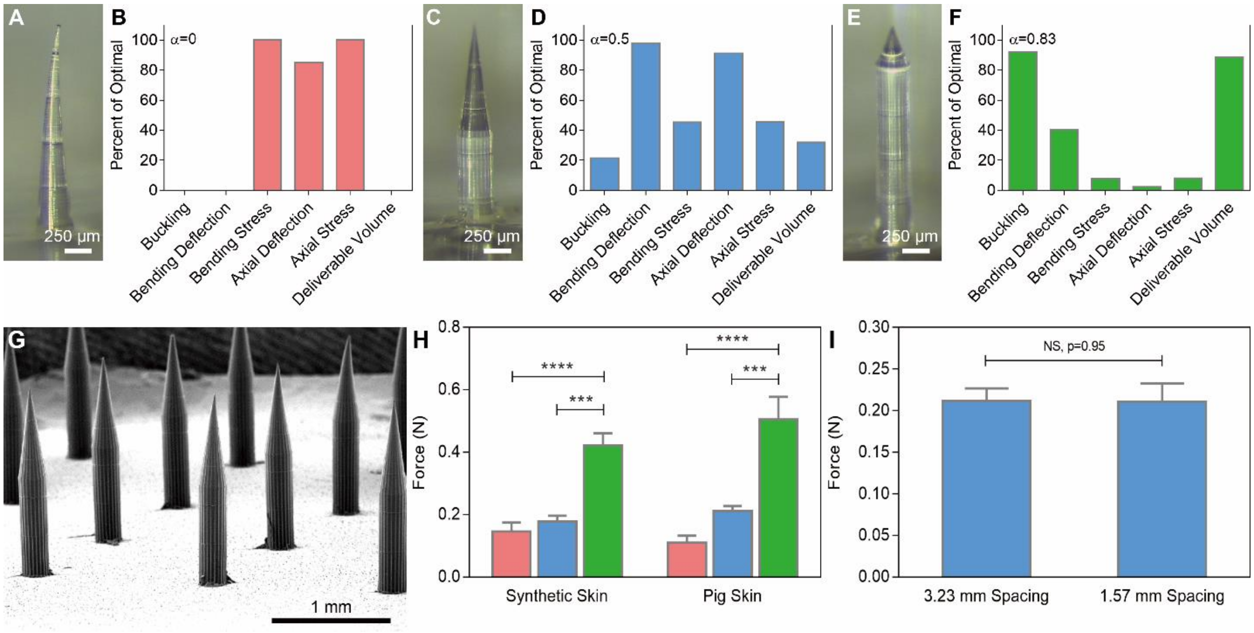

Figure 4.3: Microneedle modeling, fabrication, and evaluation.

Optical images of microneedles and finite element analysis data of (A-B) a conical needle 1500 µm in height and 300 µm at its base, (C-D) a microneedle 300 µm at its base with a 750 µm cone atop a 750 µm cylinder; and (E-F) a microneedle 300 µm at its base with a 250 µm cone atop a 1250 µm cylinder. (G) SEM image of a dissolvable microneedle array based on the geometry shown in (C, H) Ex vivo penetration force per needle based on microneedle geometry, n=3, ***p<0.001, ****p<0.0001 (one-way ANOVA with Tukey's multiple comparisons). (I) Spacing-independent penetration force requirements in pig skin (Student's t-test). In (B, D, & F) zero and one-hundred represent the worst and best values, respectively for each parameter for α between 0 and 1. Adapted from [13].

The maximum von Mises stress in the selected structure under bending, and axial loading were 9.46 MPa, and 8.71 MPa, respectively, and the axial and bending displacement were found to be negligible. The critical load factor in the selected design, obtained as 0.014557, was higher than those reported for carboxymethyl cellulose (CMC) based microneedles, estimated with the same simulation procedure as of this study [88]. Overall, the selected optimum design represented good mechanical performance as well as drug delivery capability. An overview of the stress and deformation fields within the structure of microneedles upon each loading type is provided (**Figures 4.4**). Moreover, **Figure 4.5** provides an understanding of the effect of parameter alpha on various objective functions studied.

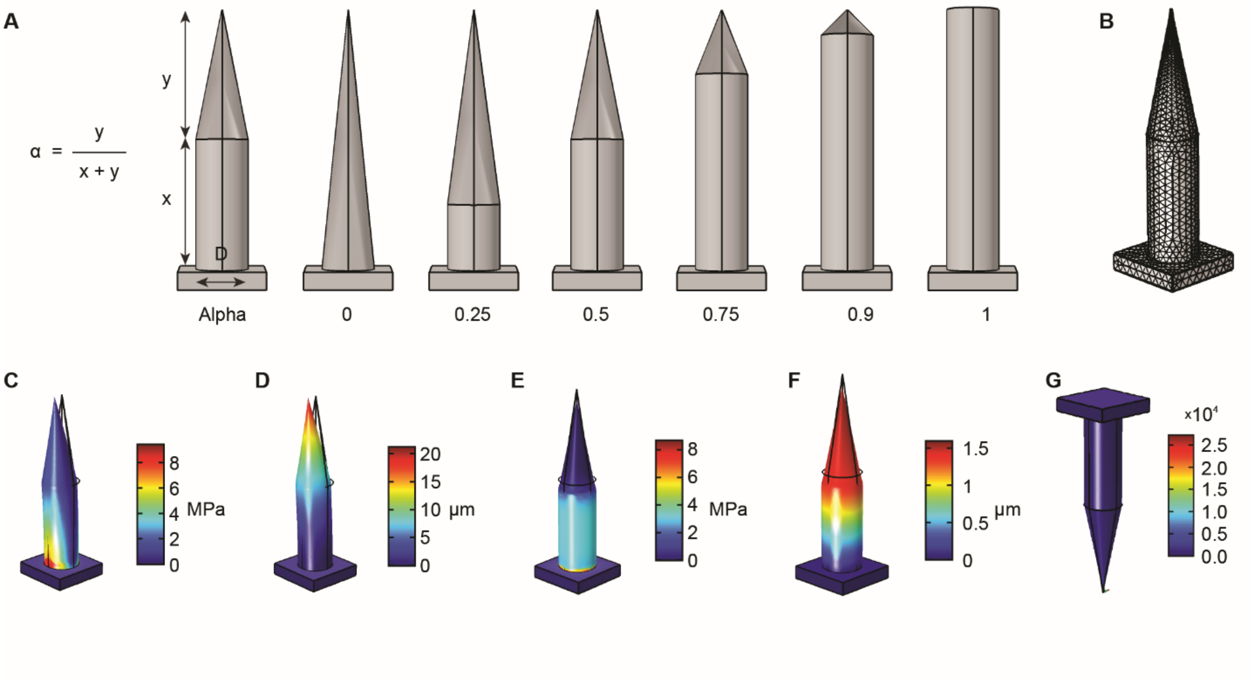

Figure 4.4: Finite element analysis of mechanical forces on microneedles.

(A) Microneedle shape was modeled in silico with shapes ranging from a cone to a cylinder. **(B)** Finite element analysis was used to assess the mechanical forces applied during microneedle penetration. Distribution of **(C)** von Mises stress during bending, **(D)** displacement during bending, **(E)** von Mises stress under axial load, and **(F)** displacement under axial load and **(G)** total displacement for the optimized design (alpha=0.5, D=300 μm). Assuming a fracture strength of PVA-sucrose equal to 13 MPa, the current design provides sufficient resistance against both axial and bending loadings. Overall, the effect of bending on displacement and induced stress was more pronounced than axial loading. Adapted from [13].

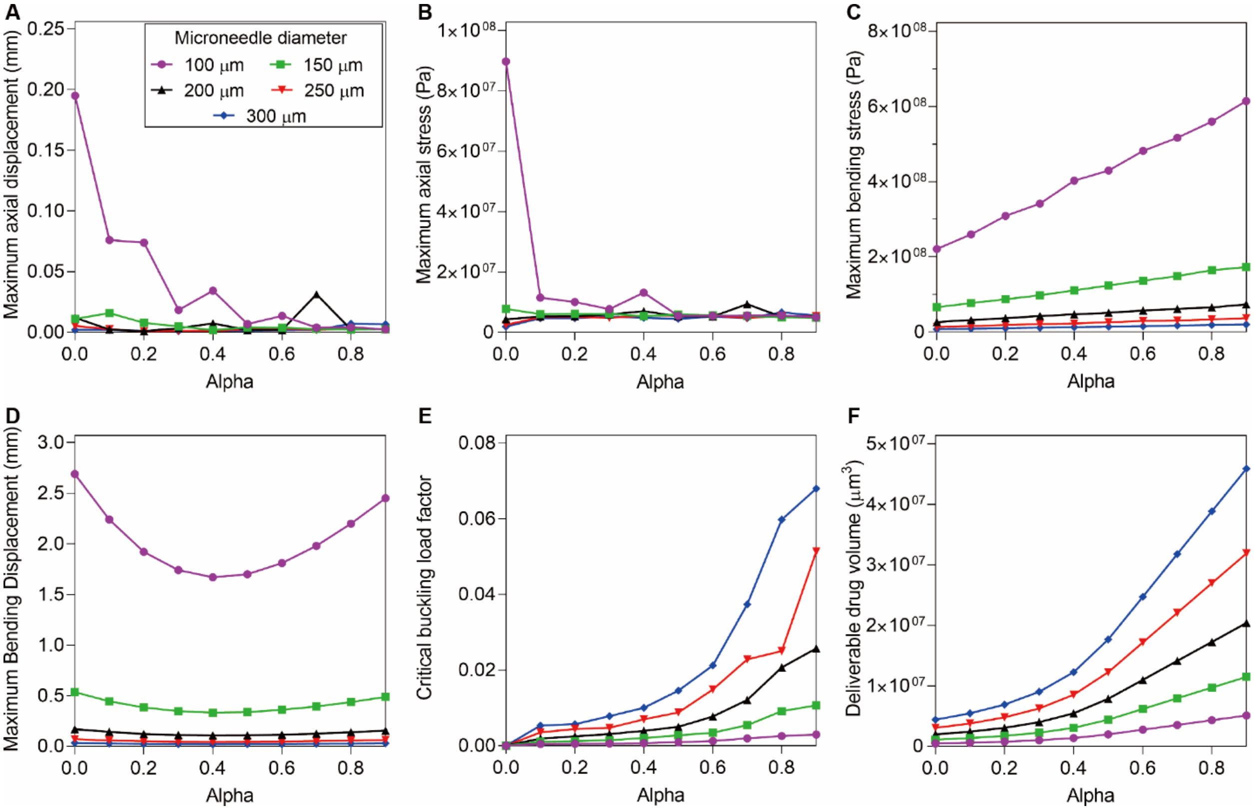

Figure 4.5: Optimization of microneedle geometry using finite element analysis.

FEA-based optimization of the microneedle geometry was performed regarding six criteria based on microneedle diameter and alpha (the proportion of microneedle height that was cylindrical). (A) maximum von Mises stress under axial loading, (B) maximum displacement under axial loading, (C) maximum von Mises stress under bending, (D) maximum displacement under bending, (E) critical load factor under buckling, and (F) theoretical deliverable drug volume, calculated as the volume of top half of the solid microneedle. In total, 50 geometries were evaluated with shaft diameter ranging from 100 to 300 µm, and alpha ranging from 0 to 0.9. Different trends were observed for each objective function but most notably, increasing microneedle diameter significantly improved mechanical performance, as well as theoretical deliverable drug volume. The upper limit of diameter was limited to 300 µm to prevent potential injection pain associated with skin piercing. A design with *alpha*=0.5 and D=300 µm was selected as the optimum geometry. Adapted from [13].

4.3 Parametric study

4.3.1 Method

A more comprehensive microneedle model was developed to provide a more systemic insight into the effect of various designs parameters (e. g. length, diameter, etc.) on mechanical resistance of the microneedles. The current microneedle model is considered solid, made from PMMA (Polymethyl methacrylate), with properties imported from Material Library module. Parametric Sweep study is used to evaluate effect of various design parameters indicated in **Figure 4.6**.

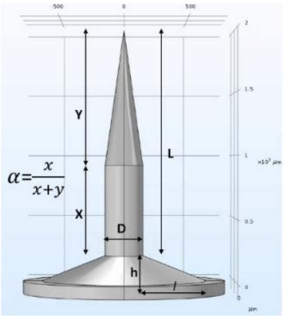

Figure 4.6: Illustration of the design parameters considered in this study. Adapted from [90].

These parameters include total length of the needle (*L*), diameter of the needle (*D*), diameter of the flange base (l), height of the base (h*)*, and the ratio of cylindrical to conical section of the needle noted as *alpha*. Different levels are considered for each design parameter as tabulated in **Table 4.1**.

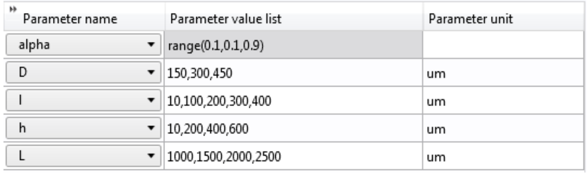

Parameter name	Parameter value list	Parameter unit
alpha	range(0.1,0.1,0.9)	
D	150,300,450	um
l	10,100,200,300,400	um
h	10,200,400,600	um
L	1000,1500,2000,2500	um

Table 4.1: Considered levels for each design parameter. Adapted from [90].

Accordingly, total length of the microneedle changes between 1000 µm to 2500 µm to be sufficiently long to reach the dermis layer. This is crucially imperative for transdermal delivery of macromolecules, such as vaccine delivery using microneedles. The same boundary conditions previously described is followed here in parametric studies.

In the next step, parametric sweep feature in COMSOL Multiphysics ® is utilized to first build up an extensive database obtained from combinational simulations of all parametric levels shown in **Table 4.1** (~2100 simulations). This database, which outputs the above mentioned five objective functions for each combination of design factors, is then used to perform a six-objective optimization study using Duckstein's method fully described in [57]. The sixth objective function is the maximum deliverable drug volume equal to total volume of the cylindrical and conical parts of the needle, excluding the base. Briefly, in this method a collective function incorporating all objective function is defined. This function represents distance of each design point from an ideal point having the best characteristics in terms of all objective functions. Design points therefore will be ranked depending how close they are to this ideal point. This collective function normalizes the corresponding values for each objective function and is defined by [57]:

$$L_p(x) = \sum_{i=1}^{k} [w_i^P \left[\frac{f_i(x)-f_i{}^0}{f_{i,max}-f_i{}^0}\right]^p]^{1/p} \qquad (4\text{-}5)$$

Where k is the total number of objective functions, w_i is the weight for the ith objective function, f_i is the value of objective function for a given design point, $f_{i,max}$ is the maximum value of objective function in the design space , and f_i^0 is the optimum (maximum or minimum) value for the ith objective function. The choice of p and w can vary. In this paper, these values are 2, and 1, respectively.

Finally, results of simulations are employed to study the order of significance of each design parameter on overall performance of the collective objective function L_p defined by Duckstein method. Statistical analyses via ANOVA were performed using software Minitab ®.

4.3.2 Results

Results of single-variable parametric study for bending and axial loading analyses are provided in Figure 3, while Figure 4 represents the results of buckling analysis. For evaluation of effect of *alpha*, *D*, and *L*, the parameter of interest varied between the values indicated in Table 1 while the other non-changing parameters remained constant as D=150 µm, L=1000 µm, h=10 µm, l=10 µm, *alpha*=0.1. The same set of parameters was employed for evaluation of effect of l and h with the exception that, for l, h was 200 µm, and for studying effect of varying h, l was considered 100 µm. All the stress contours in **Figure 4.7** represent von Misses stresses. As observed in **Figure 4.7**, bending stress and bending deflection becomes the major point of concern in these long (1000-2500 µm) microneedles, while generated maximum axial stress and axial deflection remains significantly smaller in most cases. Furthermore, the overall deflection and maximum stress, particularly in case of bending loading follows a non-linear trend.

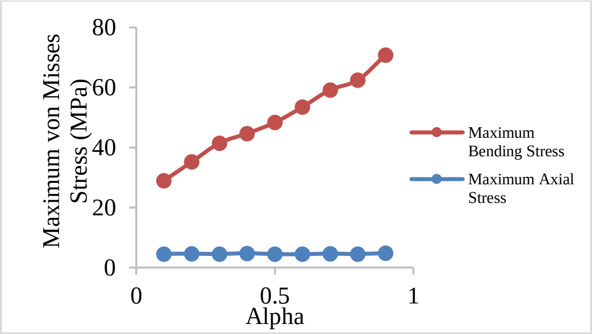
Maximum von Misses Stress (MPa)
80
60
40
20
0
0
0.5
1
Alpha
Maximum Bending Stress
Maximum Axial Stress

A

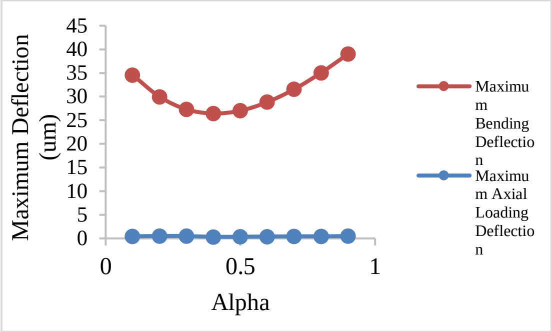
Maximum Deflection (um)
45
40
35
30
25
20
15
10
5
0
0
0.5
1
Alpha
Maximum Bending Deflection
Maximum Axial Loading Deflection

B

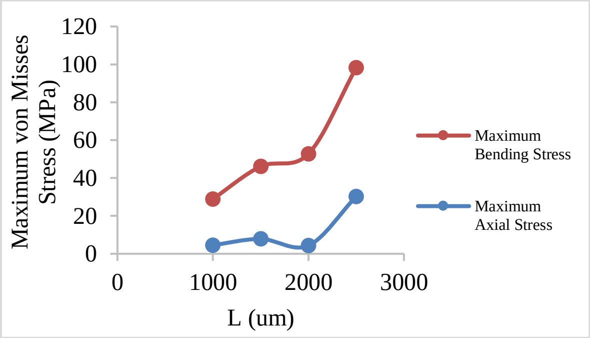
Maximum von Misses Stress (MPa)
120
100
80
60
40
20
0
0
1000
2000
3000
L (um)
Maximum Bending Stress
Maximum Axial Stress

C

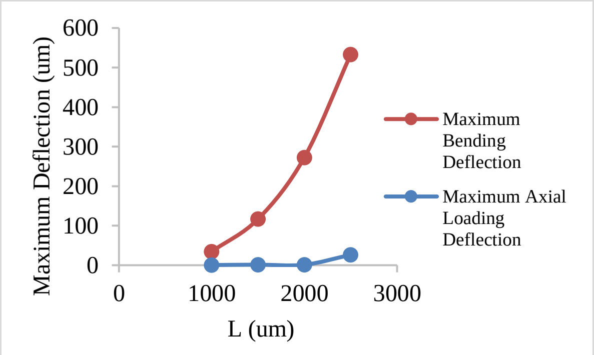
Maximum Deflection (um)
600
500
400
300
200
100
0
0
1000
2000
3000
L (um)
Maximum Bending Deflection
Maximum Axial Loading Deflection

D

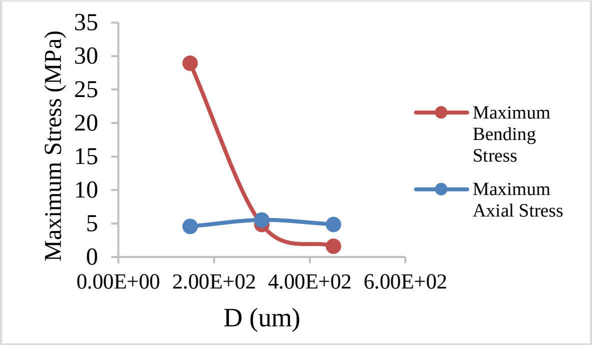

Maximum Stress (MPa)
35
30
25
20
15
10
5
0
0.00E+00
2.00E+02
4.00E+02
6.00E+02
D (um)
Maximum Bending Stress
Maximum Axial Stress

E

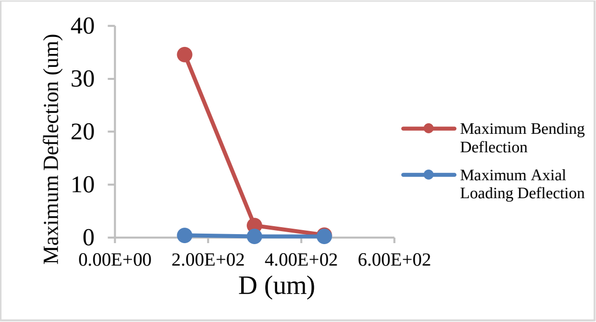

Maximum Deflection (um)
40
30
20
10
0
0.00E+00
2.00E+02
4.00E+02
6.00E+02
D (um)
Maximum Bending Deflection
Maximum Axial Loading Deflection

F

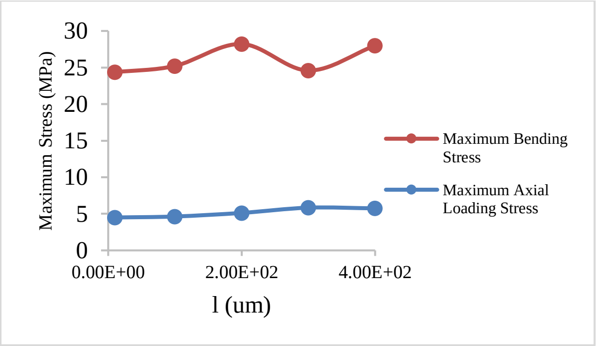

Maximum Stress (MPa)
30
25
20
15
10
5
0
0.00E+00
2.00E+02
4.00E+02
l (um)
Maximum Bending Stress
Maximum Axial Loading Stress

G

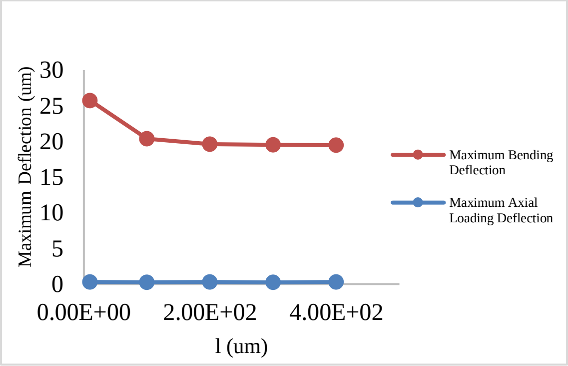

Maximum Deflection (um)
30
25
20
15
10
5
0
0.00E+00
2.00E+02
4.00E+02
l (um)
Maximum Bending Deflection
Maximum Axial Loading Deflection

H

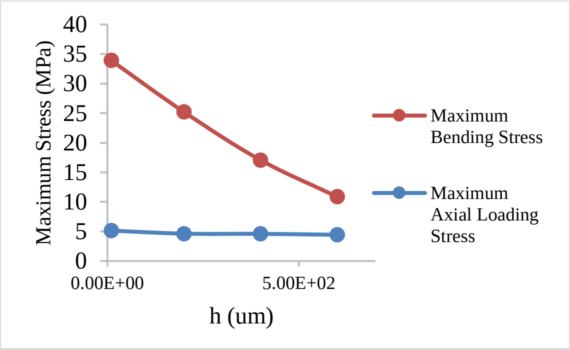

I

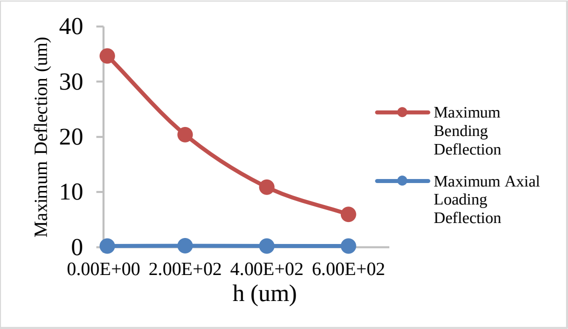

J

Figure 4.7: The effect of the considered design parameters on maximum von Misses stress (A,C,E,H,J) and maximum deflection (B,D,F,H,J) in the microneedle structure [90].

It was also evident that a value of alpha equal to 0.4 provided the optimum bending deflection behavior. Addition of the flange base reflected by increasing parameters l and h also generally decreased both types of stresses as well as deflections, enhancing mechanical stability of the structure. It was also observed that changing the microneedle diameter from 150 to 300 µm significantly improved bending behavior by decreasing both maximum bending stress and deflection, 6 times more pronounced compared to going from 300 to 450 µm. This could be of high importance for physiological aspects of drug delivery since larger needle diameter could induce more pain at injection site.

The same consideration should be made when designing the length of the needle. As deduced from **Figure 4.7**, length of the needle generally increased the maximum deflection and stress. A larger needle length might be favorable in terms of maximum deliverable drug, but it reduced mechanical stability particularly under bending, it also increased chance of touching sensory receptors beneath the dermis layer.

Results of the buckling analysis are also depicted in **Figure 4.8**. As observed, increasing length of the needle (L) increased chance of instability, conversely, increasing diameter significantly increased the loading factor thus stability under buckling.

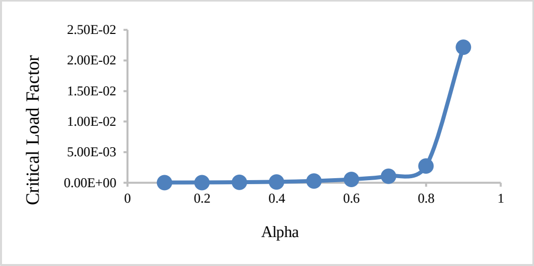

A

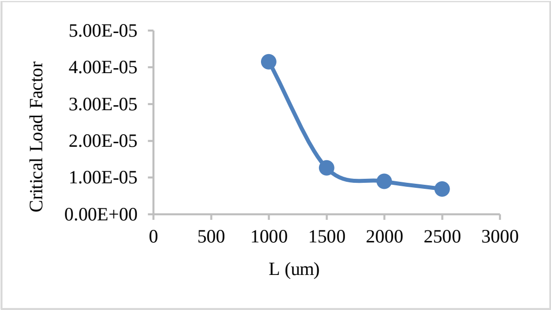

B

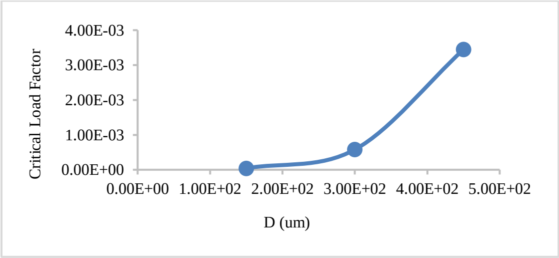

C

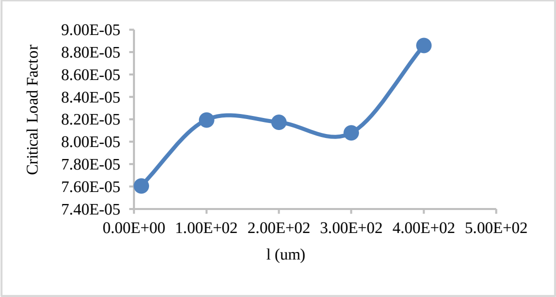

D

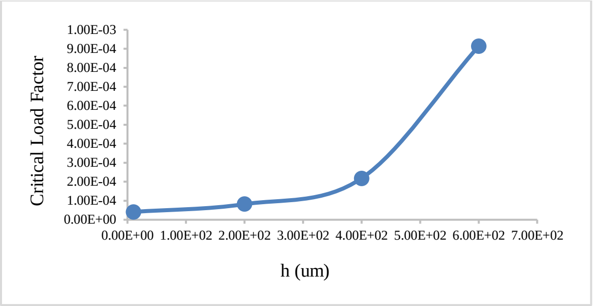

E

Figure 4.8: Effect of design paramters on cirtical buckling load, A-E corresponds to, effect of *alpha,L,D,l*, and h, respectively [90].

As presented in **Figure 4.9**, illustrating contours for the deflection and von Misses stress in the three types of analyses, maximum deflection occurred at the tip of the microneedle, both under bending and axial loading. Evidently, maximum stress was seen at the base of the needle highlighting the necessity for employing additional structural improvement at the interface of microneedle axis and base.

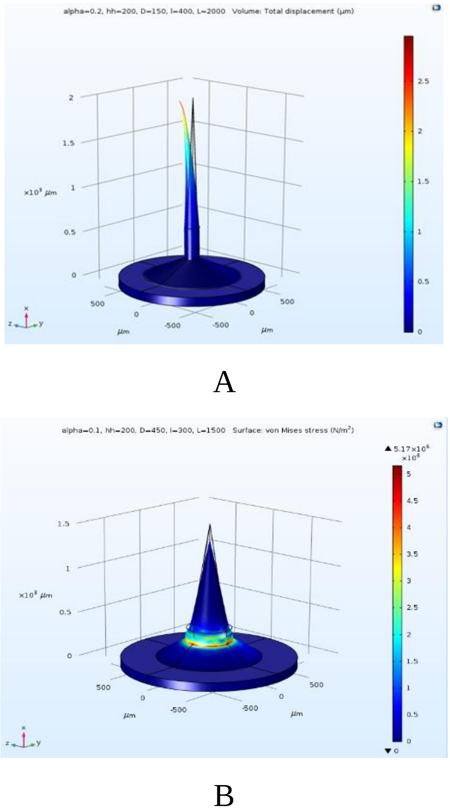

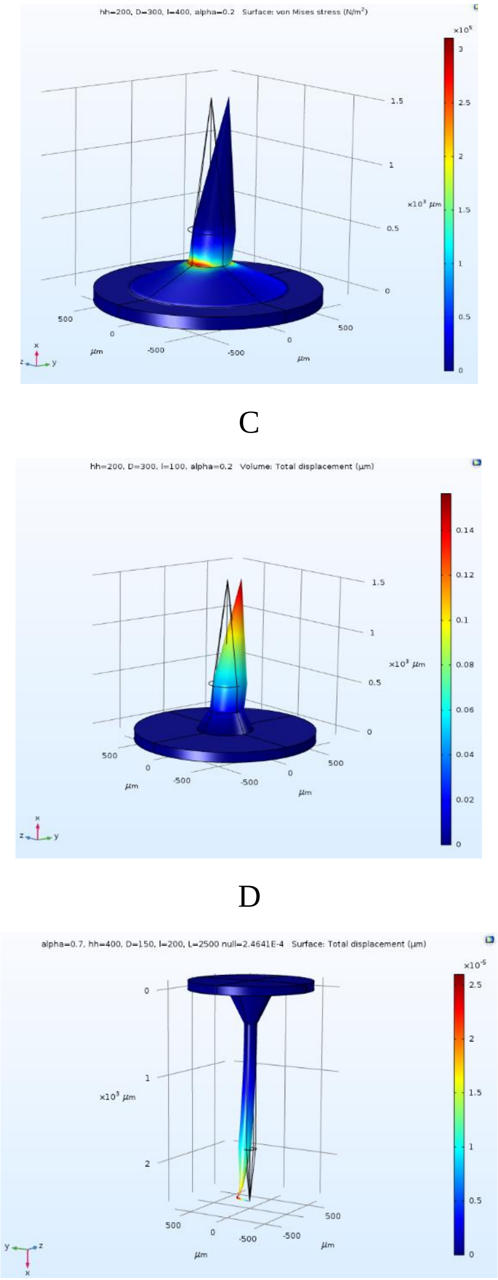

C

D

E

Figure 4.9: Contours of von Misses stress for different microneedle designs, under (A) axial, and (C) bending, and maximum deflection for different designs under (B) axial, (D) and bending loading (D), as well as (E) deflection mode under buckling [90].

Moreover, as indicated in the results of single-variable parametric study, importance of each of these design parameters could vary and sometimes lead to conflicting trends in objective functions. This would be particularly essential when taking the maximum deliverable drug into consideration. For instance, smaller *alpha* values in general provide more reliability in terms of maximum bending and axial stress, however, this would also decrease the cylindrical portion of the needle leading to smaller deliverable drug volumes. The same conflicting trend will be the case when increasing height and diameter of the base.

These conflicting behaviors thus necessitate employing a multi-objective optimization method to find the best trade-offs optimizing all objective functions simultaneously. Accordingly, result of the Duckstein normalized multi-objective optimization approach [57] are provided in **Table 4.2.** In this table, the top 10 best points based on their ranking, are represented for each of the considered needle diameters, which could be a toolbox for design engineers.

Ranking out of 2160 points	**Alpha**	**h (um)**	**D (um)**	**l (um)**	**L (um)**
1	0.9	4.00E+02	4.50E+02	1.00E+01	1.00E+03
2	0.9	4.00E+02	4.50E+02	1.00E+02	1.00E+03
3	0.9	4.00E+02	4.50E+02	2.00E+02	1.00E+03
4	0.9	4.00E+02	4.50E+02	3.00E+02	1.00E+03
5	0.8	6.00E+02	4.50E+02	2.00E+02	1.00E+03
6	0.9	1.00E+01	4.50E+02	1.00E+01	2.00E+03
7	0.9	4.00E+02	4.50E+02	1.00E+01	2.50E+03
8	0.8	6.00E+02	4.50E+02	3.00E+02	1.00E+03
9	0.9	4.00E+02	4.50E+02	1.00E+02	2.50E+03
10	0.8	6.00E+02	4.50E+02	1.00E+02	1.00E+03
437	0.9	6.00E+02	3.00E+02	1.00E+01	1.00E+03
440	0.9	6.00E+02	3.00E+02	3.00E+02	1.00E+03
445	0.9	6.00E+02	3.00E+02	4.00E+02	1.00E+03
504	0.9	6.00E+02	3.00E+02	1.00E+02	1.00E+03
639	0.1	2.00E+02	3.00E+02	1.00E+01	2.50E+03
641	0.1	4.00E+02	3.00E+02	1.00E+01	2.50E+03
644	0.1	6.00E+02	3.00E+02	1.00E+01	2.50E+03
646	0.9	4.00E+02	3.00E+02	1.00E+01	2.50E+03
649	0.1	1.00E+01	3.00E+02	1.00E+01	2.50E+03

1441	0.9	6.00E+02	1.50E+02	1.00E+02	1.00E+03
1442	0.9	6.00E+02	1.50E+02	2.00E+02	1.00E+03
1443	0.9	6.00E+02	1.50E+02	3.00E+02	1.00E+03
1444	0.9	6.00E+02	1.50E+02	4.00E+02	1.00E+03
1445	0.1	6.00E+02	1.50E+02	1.00E+02	1.50E+03
1446	0.2	6.00E+02	1.50E+02	1.00E+02	1.50E+03
1447	0.1	6.00E+02	1.50E+02	2.00E+02	1.50E+03
1448	0.1	6.00E+02	1.50E+02	1.00E+02	2.00E+03
1449	0.9	6.00E+02	1.50E+02	1.00E+01	1.00E+03
1450	0.1	4.00E+02	1.50E+02	1.00E+02	1.50E+03

Table 4.2: Ranking of the top10 optimum points for each needle diameter (150 µm, 300 µm, and 450 µm). Adapted from [90].

Furthermore, results of one-way ANOVA with or without consideration of maximum deliverable drug volume as an objective function are provided in **Tables 4.2 & 4.3**, respectively. F-value and p-value are statistical tools that could provide insight into importance of each design parameter on the overall function representing the 6 or 5 objective functions. As observed, in the former case (**Table 4.3**), all design parameters had a significant influence on the objective functions ($p<10^{-6}$), in which needle diameter had the highest percentage of contribution equal to 81%.

Source	**DF**	**Adj SS**	**Adj MS**	**F-Value**	**P-Value**	**Percentage of contribution**	**Ranking**
Alpha	8	0.3918	0.049	7.82	0.00000	0.466507989	3
h	3	0.929	0.3097	49.46	0.00000	1.106140688	2
D	2	68.8091	34.4046	5494.37	0.00000	81.92954277	1
l	4	0.292	0.073	11.66	0.00000	0.347678236	4
L	3	0.1697	0.0566	9.03	0.00001	0.202058208	5
Error	2139	13.394	0.0063				
Total	2159	83.9857					

Table 4.3: Result of ANOVA considering maximum deliverable drug volume.

Source	DF	Adj SS	Adj MS	F-Value	P-Value	Percentage of contribution	Ranking
Alpha	8	1.6454	0.20568	24.03	0.00000	3.330250	3
h	3	1.6356	0.5452	63.69	0.00000	3.310415	4
D	2	18.0386	9.01929	1053.69	0.00000	36.50969383	1
l	4	0.0418	0.01045	1.22	0.30000	0.084602198	5
L	3	9.7372	3.24573	379.19	0.00000	19.7078593	2
Error	2139	18.3092	0.00856				
Total	2159	49.4077					

Table 4.4: Result of ANOVA without consideration of maximum deliverable drug volume [90].

On the other hand, without considering the maximum deliverable volume, effect of parameter *l* became negligible (**Table 4.4**), and needle diameter (*D*), total needle length (*L*), parameter *alpha*, and height of the base (*h*) became the 1st to 4th important design factors, respectively. In both cases, needle diameter appears to be the most important design factor. These results could be used to gain insight into the parameters that could be compensated when considering other aspect of functionality of microneedles such as reduced pain induction, or manufacturing cost.

4.3.3 Conclusions

In this study, for the first-time unique feature of parametric sweep study in COMSOL was coupled with statistical tools to gain a fundamental understanding of the mechanics of microneedles in transdermal drug delivery. Subsequently, a multi-objective approach was employed to find the optimum design points within more than 2000 simulation results. Obtained results were then utilized to study the significance of each design parameter on the overall performance of the microneedle mechanics. Results indicated needle diameter as the most important geometrical factor. Results of this study could find wide application in design and development procedures of microneedle for macromolecule delivery such as vaccination.

4.4 Machine learning based image classification

4.4.1 Method

Recently, transfer learning-based machine learning has been emerged as a successful method for image classification [95,96], particularly when there is a lack of sufficient training data. In this paper, a transfer learning approach is utilized in which a pretrained AlexNet image classifier neural network with 25 layers is fine-tuned to incorporate classification of the three new patterns of interest. AlexNet convolutional neural network is one of the most successful image classification neural networks, originally trained on more than 1 million images and can classify 1000 categories, thus possessing rich feature extraction capabilities [97]. Input to the network is an image and the output is a set of image labels, and the probabilities, or the level of detection confidence, associated with each label. Accordingly, Deep Learning Toolbox™ model for AlexNet in MATLAB® was utilized for all steps involving image classification. Subsequently, all layers of AlexNet, except the last three, were directly transferred into a modified AlexNet deep convolutional neural network (CNN). The last three layers (i. e. 23-25) were modified during the training to include the new patterns. The rest of the layers (i. e. 1-22), directly transferred from the original AlexNet, represented image segmentation and feature extraction properties already trained in the original network.

To generate the training dataset, 30 images per pattern, called source image, were selected from group#9 and the abbreviated group. Image augmentation was then performed on each source image, containing an individual pattern, by applying a set of modifications using a preprocessing code called “ImagePrepare.m”. The code involved a series of functions which cropped around the pattern, randomly flipped and rotated each source image, normalized brightness intensity, turned the image into greyscale, and lastly, resized it to the input image size required for AlexNet. Subsequently, the resulting modified image, generated from a source image, was saved as an input training image. Overall, 100 augmented images were generated per each source image (3000 per pattern). Using this approach, 70% of the generated images were used for training of the last three layers of the network, and 30% for validation. Rectified Linear Unit (ReLu) was employed as the activation function. In addition, a maximum Epoch number of 20, minibatch size of 10, and initial learning rate of 10^{-4} were selected during the training. An overview of the procedure performed during image preparation and classification are shown in **Figure 4.10**. Moreover, **Figure 4.11** shows an example of augmenting in vivo images to synthetic samples used for the training/validation (pattern "X'). The training approach was based on labeled and supervised data, and a validation accuracy of 100% was achieved after the 20th epoch (**Figure 4.12**). Training was performed on a single GPU.

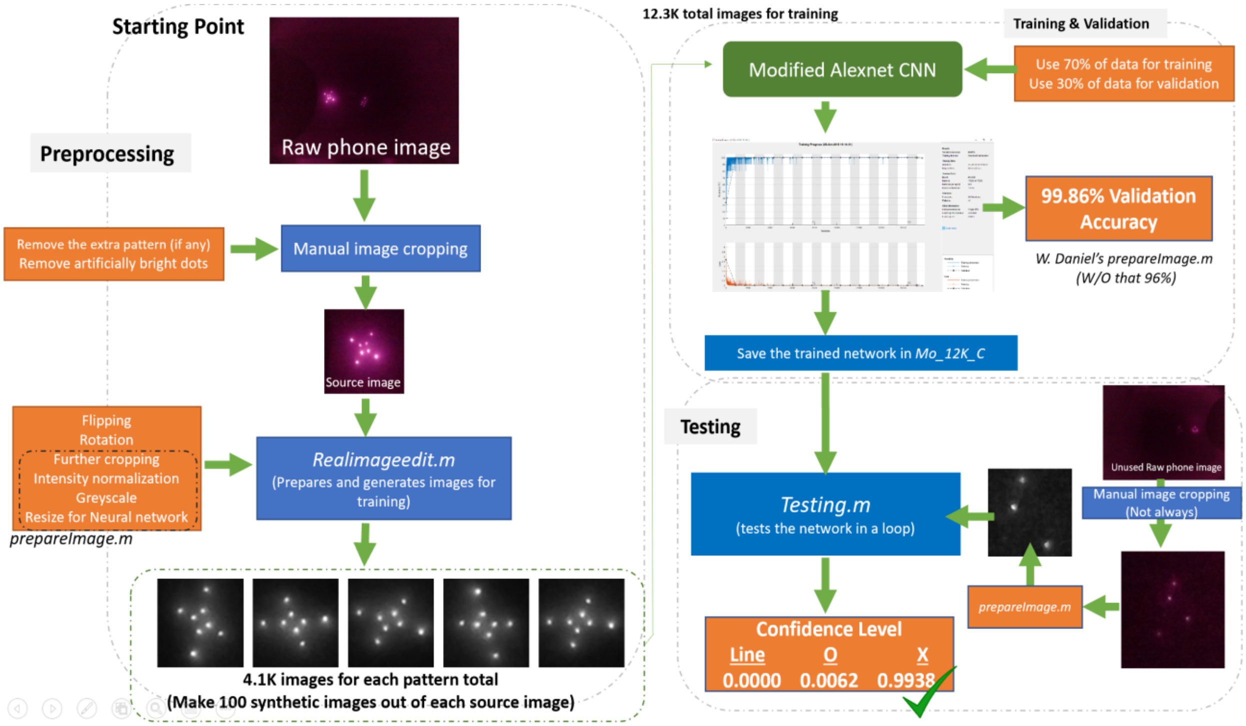

Figure 4.10: An overview of the procedure from data collection to training the image classifier and testing the algorithm with unseen data.

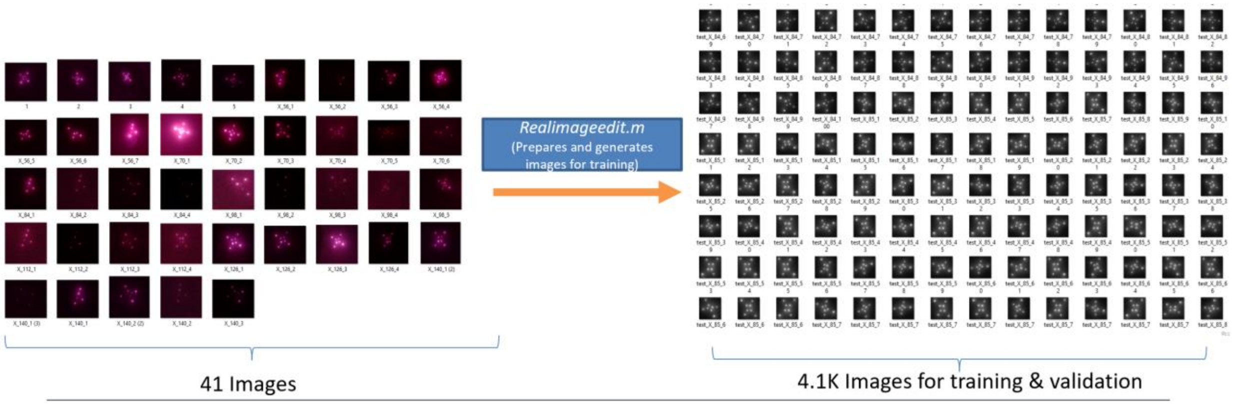

Figure 4.11: An example of image augmentation using the script "realimageedit.m" to expand in vivo source images and provide enough samples for training the machine learning algorithm [13].

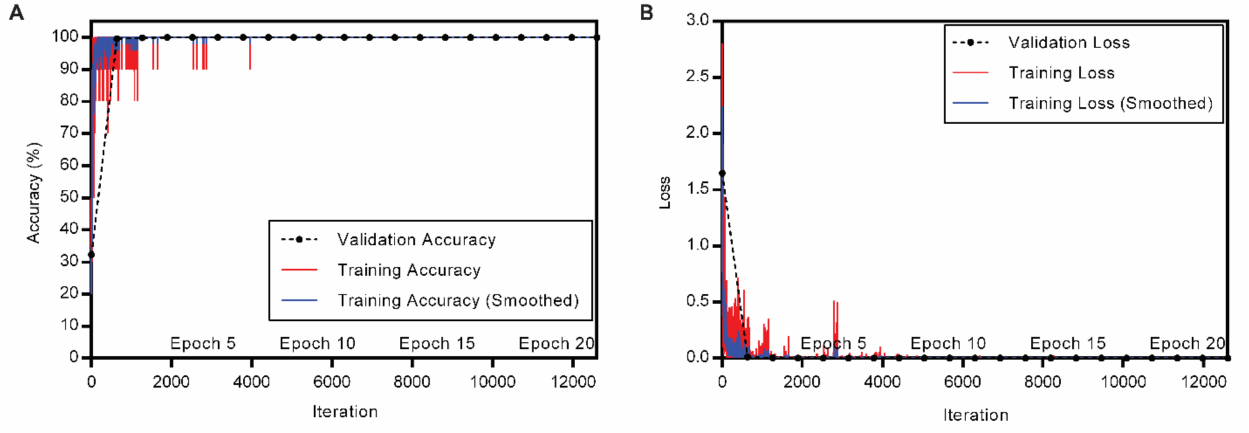

Figure 4.12: Machine learning training and validation.

Example of training and validation results from a modified AlexNet network. The resulting validation accuracy after 20 epochs was obtained as 100%, and the loss went to 0, reprinted from [13].

Unseen in vivo images were selected to test performance of the modified AlexNet in the automated pattern classification algorithm. In agreement with the training, a similar preprocessing was performed on the test images. Accordingly, the corresponding image for the testing, was first cropped around the pattern, then turned into greyscale, resized to the dimensions suitable for AlexNet and its intensity was subsequently normalized. Next, the preprocessed image was incorporated into the modified AlexNet neural network for testing the accuracy of classification into either of three patterns. A real example of images taken in vivo (rats) for three different patterns at different timepoints is shown in **Figure 4.13** [13].

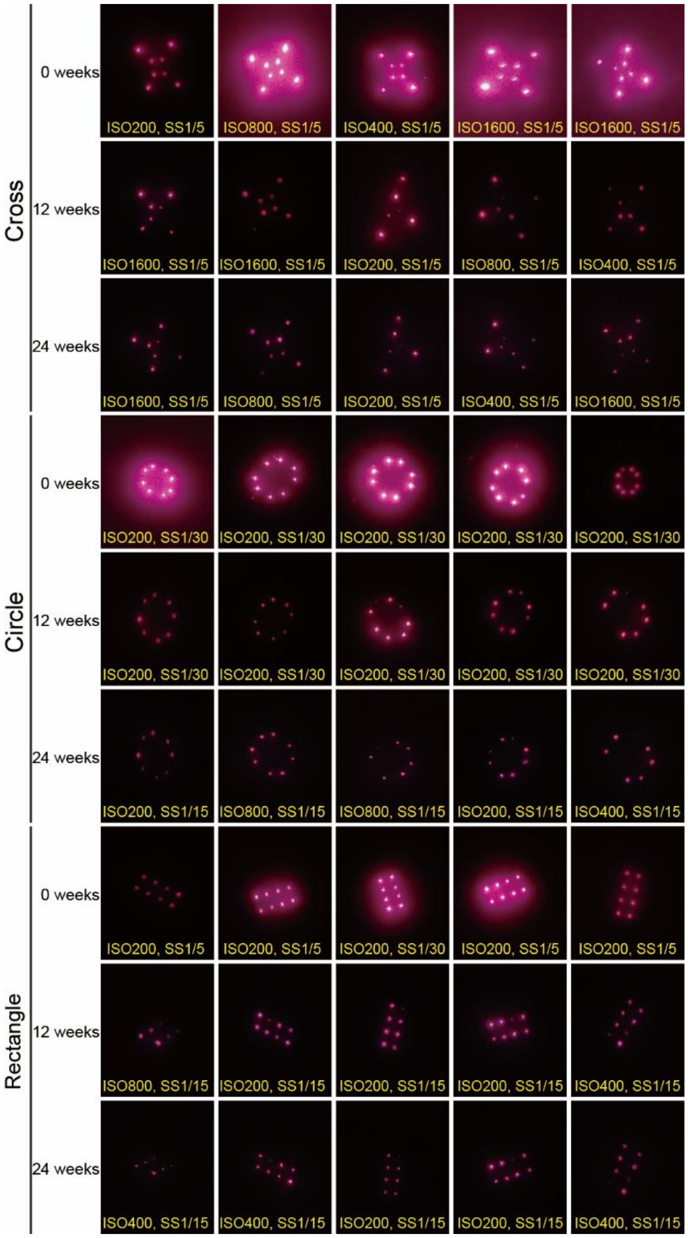

Figure 4.13. Longitudinal imaging of NIR markings in vivo.

Cropped, but otherwise raw smartphone images showing NIR patterns on rats 0-, 12-, and 24-weeks post-administration, reprinted from [13].

The input to the modified network was the preprocessed image, and the output was a 3 by 1 array representing probability associated with classification of a certain image with the each of the three patterns. For both training and testing, each image contained an individual pattern.

4.4.2 Results & Discussion

The resulting confidence levels categorized by each pattern and day, during the entire tracking period, is plotted in **Figure 4.14**. The confidence level is an output of the network indicating the probability associated with a certain pattern classification. Overall, 80 images were tested for the pattern circle, 70 for pattern “X”, and 60 for pattern line. The modified transfer-based CNN network using AlexNet provided extremely accurate detection confidence over all days and patterns (**Figure 4.14**). All 210 images tested were accurately detected with a confidence level of more than 99.0%.

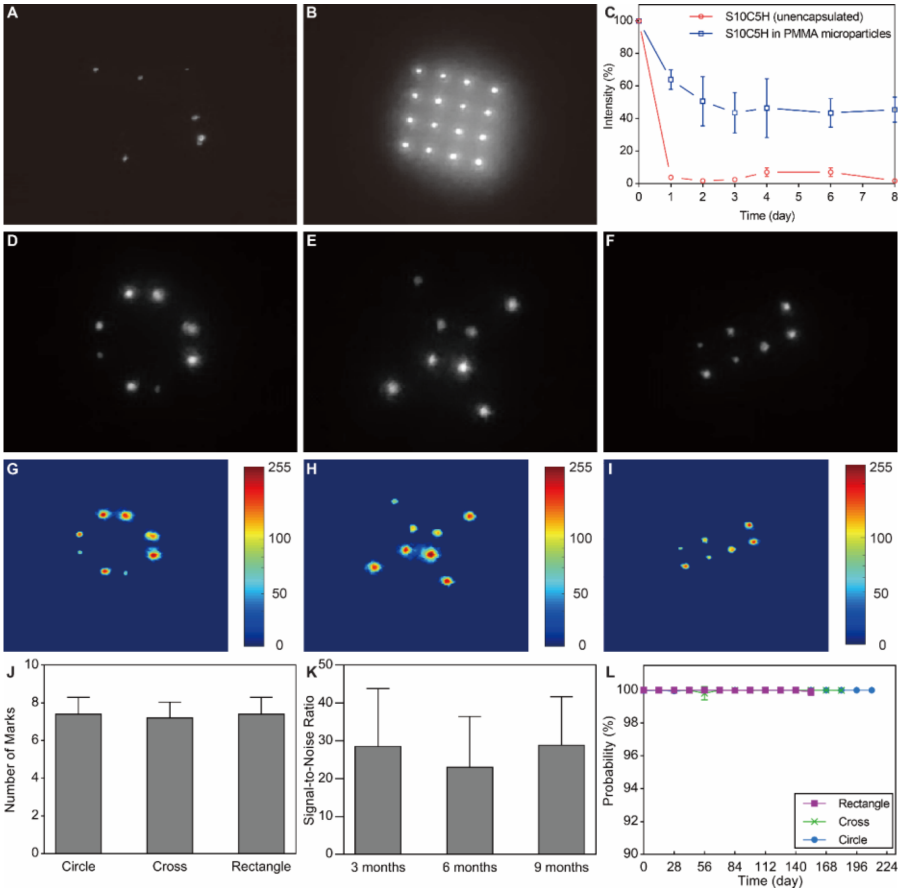

Figure 4.14: In vivo imaging of NIR patterns. Administration site after the delivery of a 4x4 microneedle patch containing various loads listed. Reprinted from [13].

(A) Unencapsulated QDs or (B) PMMA-encapsulated QDs. (C) Short-term study showing that the encapsulation of hydrophobic QDs is necessary to retain a large amount of signal and that a majority of signal loss occurs in the days immediately following application, n=4. Images of (D) circle, (E) cross, and (F) rectangle patterns imaged 24 weeks after administration. Log-scale color maps of the same (G) circle, (H) cross, and (I) rectangle patterns emphasizing the low amount of background relative to signal. (J) Number of markings remaining 24 weeks post-administration, n=5. (K) Quantification of signal-to-noise ratio for the circle pattern showing no statistically significant changes between 12, 24, and 36 weeks, n=15 (one-way ANOVA with Tukey's multiple comparisons). (L) Graph showing the average probability of the machine learning algorithm (all patterns correctly detected), n=5. Grayscale images extracted from red channel of the adapted smartphone-generated RGB image. Adapted from [13].

The current machine learning approach based on AlexNet method provides a highly robust automated pattern classification approach that cannot be provided by a human healthcare worker. Under a real case application, factors such as lack of enough training, visual deviation from the ideal pattern, and stressful environment (e. g. in a fully congested healthcare center) would make it extremely hard for a human healthcare worker to reliably detect and distinguish between different patterns within a short time. The described deep learning-based approach on the other hand can address various types of uncertainties in the pattern, such as missed dots, image light intensity distortion, and change in angle or orientation of imaging just in fractions of seconds. Furthermore, the current capability could be conveniently expanded to more than three patterns just by expanding the size of the classes in the training dataset.

CHAPTER

5

CONCLUSIONS AND FUTURE WORK

5.1 Conclusions

In this thesis, we analyzed two next generation platforms for controlled vaccine delivery developed based on microfabrication of biodegradable polymers. The first technology, core-shell microparticles, can provide considerable value to patients by minimizing the number of visits required to obtain subsequent vaccination shots. This is especially a critical challenge in low-income countries, remote locations, and developing world with lack of advanced healthcare infrastructure. We specifically focused on two aspects in translation of core-shell microparticles, namely, improving injectability and understating the unique mechanism of pulsatile release.

To study injectability of microparticles, a multi-disciplinary approach was used to establish a comprehensive design framework. Injection of microparticles have been found to be a critical factor in clinical translation of biomedical products [98-100]. This framework is based on particle shape and thus can be extended to applications beyond core-shell microparticles and include emulsion-based or micromolded drug delivery systems (such as works described in [18, 101]). Computational tools including multiphysics simulations and design of experiment were further employed to simulate and systemically study design parameters affecting injection of microparticles. This study is the first to simulate flow of microparticles in a hypodermic syringe-needle system using integration of fluid dynamics and particle tracing modules. State-of-art tools such as machine learning and SLS 3D-printing provided a roadmap to improve design of existing syringes. Improving design of existing hypodermic syringes can be another method to significantly improve parenteral injection of microparticles. Results of this study can be useful for studying/engineering other complex drug delivery systems, providing a roadmap for future studies.

In the second part of thesis, we focused on a more fundamental aspect in design of core-shell microparticles, namely, mechanism of pulsatile release. The present core-shell microparticles is the only injectable drug delivery system capable of providing a delayed pulsatile release kinetics. Despite this unique feature, the mechanism of action in these particles is poorly understood. We combined computational and experimental tools to provide a multi-faceted insight into degradation of polymer upon incubation in vitro. Various design parameters (based on composition and morphology) were investigated in view of affecting the release timepoint. Experimental and computational tools both pointed out to porosity as a dominant factor in governing the release timepoint. The impact of composition was found to be more important than the geometry, therefore making the release kinetics independent of the particle size, for the scale of the particles studied. This study was the first to visualize path formation in the PLGA matrix, confirming previous speculations on degradation of PLGA-based biomaterials. A color-based, simple and qualitative method was further introduced to map changes in the pH over particle microstructure. Computational results supported experimental observations pointing out to the fact that pulsatile release occurs subsequent to sudden expansion of the cap in core-shell particles. Overall, extensive experimental and computational techniques were utilized to study various aspects of particle degradation, namely, pore-formation, deformation (swelling), change in the pH of the cap and core, and visualization of the release kinetics from core-shell particles. Results of this study can potentially contribute to understanding the complex behavior of biodegradable biomaterials beyond core-shell particles such as microspheres, micromolded particles, and implants.

In the next phase of this thesis, we focused on a transdermal drug delivery platform for controlled vaccine delivery. These microneedles were capable of transferring a fluorescent dye into the skin, invisible to naked eyes but visible under smart phone camera. The pattern could be used as an encoding scheme for on-patient medical record tracking. These microneedles were able to successfully co-deliver vaccines in addition to fluorescent patterns encapsulated in the microneedle array. As a result, this platform technology could be widely applicable to single administration of vaccines and on-patient medical recording in remote geographic areas and developing countries with limited infrastructure.

More specifically, we investigated two aspects of the technology, namely, computational modeling/optimization as well as machine learning based automated detection algorithm. We studied 50 different microneedle designs with respect to various mechanical loads imposed on microneedles upon insertion into the skin. Later, during the parametric study, we developed a more comprehensive model of an individual microneedle. More than 2000 designs were studied to find the best trade-off designs in terms of all objective functions simultaneously. The selected microneedle design represented desirable mechanical characteristics upon application ex vivo and in vivo.

Next, an automated classification algorithm was introduced to facilitate pattern detection for various microneedle arrays transferred to skin. The goals were to minimize potential human error caused by manual classification. The automated algorithm showed strong reliability, with all testing patterns being detected correctly with a relative confidence of 98% on average. This shows great promise of using machine learning for successfully automating tasks involved in on-patient medical record. The image processing algorithm was successfully integrated into the machine learning algorithm to augment the existing data for patterns. Results showed that this approach significantly improved training/validation accuracy, without leading to overfitting. The custom image processing algorithm further improved the classification accuracy for the testing set by reducing noise and zooming on the patterns.

Overall, this thesis aimed to further develop two platform technologies for controlled vaccine delivery. In particular, results of this thesis show feasibility of integrating computational tools, especially machine learning into studying complex drug delivery devices. This study, for the first time, validates machine learning as a reliable tool for prediction, automation and understanding the behavior of drug delivery systems.

5.2 Future works

The work presented in this thesis highlights several tools that can be used to translate and develop controlled drug delivery formulations beyond vaccine delivery. The following summarizes six areas that are extensions of this work.

1) Using microparticles for areas beyond vaccination, namely, cancer research, local intratumoral treatments, gene delivery, and pulsatile hormone release. Given the unique encapsulation process compatible with biologics, there could be considerable potential for the core-shell platform to be used for extended delivery of cargos otherwise undeliverable with existing drug delivery systems. Some of these cargos include antibodies, genes, small hydrophilic molecules, and cytokines. Given the unique mechanism of degradation in these particles there is also opportunity for co-delivery of multiple agents simultaneously from an individual particle.

2) Predictive models for release kinetics from core-shell particles. There are opportunities to use machine learning algorithm or other tools to predict the release timepoint for a given microparticle design. This can be of high interest to the drug delivery and medicine community to be able to design an optimized delivery system tailored to a specific release kinetics.

3) Core-shell microparticles for oral drug delivery. The protective nature of the core shell platform provides opportunities for encapsulation/protection of therapeutics against the acidic gastric fluid. Further, by fine-tuning the material properties used in core shell particles, it would be desirable to coat a layer of mucoadhesive polymers to the particles to enhance local resident and adhesion to the gastrointestinal wall. The underlying polymer can also be fabricated from pH-responsive polymers to further localize release of cargo to specific locations within the intestine.

4) Microneedle patches with time-changing patterns. These microneedles follow the same principles used in the current design with the exception that patterns are designed to degrade and disappear after a certain period. This approach could be helpful to determine the timing after administration of a given medication be assessing the intensity of the pattern as a potential indicator.

5) On-demand portable device for automated manufacturing of microneedles. A portable device which can provide local manufacturing capability would be particularly beneficial in case of future pandemics and outbreaks. Such a device could be used to produce a certain number of microneedle patches in an embedded manufacturing device which would minimize human interventions for maintaining a sterilized environment. Moreover, the microneedle manufacturing could be automated to enhance throughput and make the device useable for

workers without wet lab training. Such a device could be particularly important for on-demand applications in pharmacy (e. g. flu shots) or in battlefield (certain vaccinations for healing soldiers).

6) Machine learning algorithms for synthetic pattern generation/optimization for long-term medical record tracking. In this study, we successfully demonstrated feasibility of using machine learning for automated pattern detection. Training the detection algorithms was done from in vivo data from application in rats. However, there is also opportunity to develop synthetic patterns which do not depend on the abundance of in vivo data and find the best encoding arrays to minimize potential errors involved in application of patches (lost needles, non-transferred needle, scars, etc). This approach can further provide a library of patterns that can be reliably used to transfer critical data for medical record tracking.

REFERENCES

1. Black, Robert E., et al. "Global, regional, and national causes of child mortality in 2008: a systematic analysis." *The lancet* 375.9730 (2010): 1969-1987.
2. https://www.un.org/en/desa/covid-19-slash-global-economic-output-85-trillion-over-next-two-years#:~:text=The%20global%20economy%20is%20expected,of%20the%20previous%20four%20years.&text=The%20report%20estimates%20that%20GDP,to%20%2D5.0%25%20in%202020.
3. https://www.who.int/data/stories/the-true-death-toll-of-covid-19-estimating-global-excess-mortality
4. McHugh, Kevin J., et al. "Single-injection vaccines: Progress, challenges, and opportunities." *Journal of Controlled Release* 219 (2015): 596-609.
5. E. Legesse, W. Dechasa, An assessment of child immunization coverage and its determinants in Sinana District, Southeast Ethiopia. BMC Pediatr. 15, 31 (2015).
6. Hou, Xucheng, et al. "Lipid nanoparticles for mRNA delivery." *Nature Reviews Materials* (2021): 1-17.
7. Oyston, Petra, and Karen Robinson. "The current challenges for vaccine development." *Journal of medical microbiology* 61.7 (2012): 889-894.
8. P. G. Szilagyi, L. E. Rodewald, Missed opportunities for immunizations: A review of the evidence. J. Public Health Manag. Pract. 2, 18–25 (1996).
9. McHugh, Kevin J., et al. "Fabrication of fillable microparticles and other complex 3D microstructures." *Science* 357.6356 (2017): 1138-1142.
10. Lu, Xueguang, et al. "Engineered PLGA microparticles for long-term, pulsatile release of STING agonist for cancer immunotherapy." Science translational medicine 12.556 (2020).
11. Tran, Khanh TM, et al. "Transdermal microneedles for the programmable burst release of multiple vaccine payloads." Nature Biomedical Engineering (2020): 1-10.

12. Tzeng, Stephany Y., et al. "Stabilized single-injection inactivated polio vaccine elicits a strong neutralizing immune response." Proceedings of the National Academy of Sciences 115.23 (2018): E5269-E5278.
13. McHugh, Kevin J., et al. "Biocompatible near-infrared quantum dots delivered to the skin by microneedle patches record vaccination." *Science translational medicine* 11.523 (2019).
14. Sarmadi, Morteza, et al. "Modeling, design, and machine learning-based framework for optimal injectability of microparticle-based drug formulations." Science advances 6.28 (2020): eabb6594.
15. R. Langer, Drug delivery and targeting. Nature, 5-10 (1998).
16. K. E. Uhrich, et al. Polymeric systems for controlled drug release. Chem. Rev. 99, 3181-3198 (1999).
17. D. A. Lavan, T. McGuire, and R. Langer. Small-scale systems for in vivo drug delivery. Nat. Biotech. 21, 1184-1191 (2003).
18. J. P. Rolland, et al., Direct fabrication and harvesting of monodisperse, shape-specific nanobiomaterials., *J. Am. Chem. Soc.* **127**, 10096-10100 (2005).
19. S. Freiberg, and X. X. Zhu, Polymer microspheres for controlled drug release. *Int. J. Pharm.* **282**, 1-18 (2004).
20. B. K. Kim, et al., Preparation and characterization of drug-loaded polymethacrylate microspheres by an emulsion solvent evaporation method. *J. Microencapsul.* **19**, 811-822 (2002).
21. A. Shamloo, et al., Accelerated full-thickness wound healing via sustained bFGF delivery based on a PVA/chitosan/gelatin hydrogel incorporating PCL microspheres. *Int. J. Pharm.* **537**, 278-289 (2018).
22. J. A. Champion, Y. K. Katare, and S. Mitragotri. Particle shape: a new design parameter for micro-and nanoscale drug delivery carriers. *J Control Release* **127,** 3-9 (2007).
23. P. L. Ritger, and N. A. Peppas. A simple equation for description of solute release I. Fickian and non-fickian release from non-swellable devices in the form of slabs, spheres, cylinders or discs. *J Control Release* **5**, 23-36 (1987).

24. S. Mitragotri, P. A. Burke, and R. Langer., Overcoming the challenges in administering biopharmaceuticals: formulation and delivery strategies. *Nat. Rev. Drug Discov.* **13**, 655-672 (2014).
25. L. Arendt-Nielsen, H. Egekvist, and P. Bjerring. Pain following controlled cutaneous insertion of needles with different diameters. *Somatosens Mot. Res.* **23,** 37-43 (2006).
26. M. Iwanaga, and K. Kamoi. Patient perceptions of injection pain and anxiety: a comparison of NovoFine 32-gauge tip 6mm and Micro Fine Plus 31-gauge 5mm needles. *Diabetes. Technol. The.* **11**, 81-86 (2009).
27. F. Cilurzo, et al., Injectability evaluation: an open issue. *AAPS Pharm. Sci. Tech.* **12**, 604-609 (2011).
28. C. Berteau, et al., Evaluation of the impact of viscosity, injection volume, and injection flow rate on subcutaneous injection tolerance. *Med. Dev. (Auckland, NZ)* **8**, 473 (2015).
29. E. L. Giudice, and J. D. Campbell. Needle-free vaccine delivery. *Adv. Drug Deliv. Rev.* **58**, 68-89 (2006).
30. G. D. Chitnis, et al., A resistance-sensing mechanical injector for the precise delivery of liquids to target tissue. *Nat. Biomed. Eng.* **3**, 621-631 (2019).
31. J. A. Champion, and Samir Mitragotri. Role of target geometry in phagocytosis. *Proc. Natl. Acad. Sci. U.S.A.* **103**, 4930-4934 (2006).
32. J. A. Champion, A. Walker, and S. Mitragotri, Role of particle size in phagocytosis of polymeric microspheres. *Pharm. Res.* **25**, 1815-1821(2008).
33. M. Forouzandehmehr, and A. Shamloo, Margination and adhesion of micro-and nanoparticles in the coronary circulation: a step towards optimised drug carrier design. *Biomech. Model Mechan.* **17**, 205-221 (2018).
34. T. Küme, et al., The effects of different syringe volume, needle size and sample volume on blood gas analysis in syringes washed with heparin. Biochem. Medica **22**, 189-201 (2012).
35. Nkanga, Christian Isalomboto, et al. "Clinically established biodegradable long acting injectables: An industry perspective." *Advanced drug delivery reviews* (2020).
36. H. Zhong, et al. A comprehensive map of FDA-approved pharmaceutical products. *Pharmaceutics* **10**, 263 (2018).
37. S R. Langer, New methods of drug delivery. Science 249, 1527-1533 (1990).

38. A. Khalkhali, H. Noraie, and M. Sarmadi, Sensitivity analysis and optimization of hot-stamping process of automotive components using analysis of variance and Taguchi technique, P. I. MECH. ENG. E-J. PRO. 231, 732-746 (2017).
39. R. D. Firouz-Abadi, et al., A modified molecular structural mechanics model for the buckling analysis of single layer graphene sheet. Solid State Commun. 225, 12-16 (2016).
40. M. H. Shojaeefard, et al., Investigation on the optimal simplified model of BIW structure using FEM. Lat. Am. J. Solids Stru. 12, 1972-1990 (2015).
41. M. Sarmadi, A. Shamloo, and M. Mohseni. Utilization of Molecular Dynamics Simulation Coupled with Experimental Assays to Optimize Biocompatibility of an Electrospun PCL/PVA Scaffold. *PloS one* **12**, e0169451 (2017).
42. A. Shamloo, Amir, and Morteza Sarmadi. "Investigation of the adhesive characteristics of polymer–protein systems through molecular dynamics simulation and their relation to cell adhesion and proliferation. *Integr Biol-UK* **8**, 1276-1295 (2016).
43. X. Luo, et al., CAD based design sensitivity analysis and shape optimization of scaffolds for bio-root regeneration in swine. *Biomaterials* **57**, 59-72 (2015).
44. C. Rungsiyakull, et al. Surface morphology optimization for osseointegration of coated implants. *Biomaterials* **31**, 7196-7204 (2010).
45. Li, W., et al. Fibre reinforced composite dental bridge. Part II: numerical investigation. *Biomaterials* **25**, 4995-5001(2004).
46. M. O. Wang, et al., Evaluating 3D-Printed biomaterials as scaffolds for vascularized bone tissue engineering. *Adv. Mater.* **27**, 138-144 (2015).
47. M. Bohner, et al., Theoretical and experimental model to describe the injection of a polymethylmethacrylate cement into a porous structure. *Biomaterials* **24**, 2721-2730 (2003).
48. M. S. Yeoman, et al., A constitutive model for the warp-weft coupled non-linear behavior of knitted biomedical textiles. Biomaterials **31**, 8484-8493 (2010).
49. R. S. Rao, et al., The Taguchi methodology as a statistical tool for biotechnological applications: a critical appraisal. Biotechnol. J. Healthcare Nutrition Technology 3, 510-523 (2008).
50. K. Yu, A. L. Beam, and I. S. Kohane. Artificial intelligence in healthcare. Nat. Biomed. Eng. 2, 719-731 (2018).

51. C. U. Oramasionwu, et al. Estimated cost of injectable medication waste attributable to syringe dead space. *Jama. Intern. Med.* **176**, 1025-1027 (2016).
52. R. Darby, R. P. Chhabra, and R. Darby. *Chemical engineering fluid mechanics, revised and expanded*. CRC Press, 2001.
53. H. Wadell, Volume, shape, and roundness of quartz particles. *J. Geol.* **43**, 250-280 (1935).
54. X. Liu, et al., Ciprofloxacin-loaded sodium alginate/poly (lactic-co-glycolic acid) electrospun fibrous mats for wound healing. Eur. J. Pharm. Biopharm., **123**, 42-49 (2018).
55. O. Qutachi, et al., Injectable and porous PLGA microspheres that form highly porous scaffolds at body temperature. *Acta Biomet.* **10**, 5090-5098 (2014).
56. T. WJ. Steele, et al., The effect of polyethylene glycol structure on paclitaxel drug release and mechanical properties of PLGA thin films. *Acta Biomet.* **7**, 1973-1983 (2011).
57. G. Chiandussi, et al., Comparison of multi-objective optimization methodologies for engineering applications. Comput. Math. Appl. **63**, 912-942 (2012).
58. Sarmadi, M., et al. "A Multiphysics Model for Microparticle Transport through Hypodermic Needles." COMSOL Annual conference 2019, Boston.
59. Khalkhali, Abolfazl, et al. "Probabilistic multi-objective optimization of a corrugated-core sandwich structure." *Geomechanics and Engineering* **10.6** (2016): 709-726.
60. McHugh, Kevin J., et al. "Determining vaccination status in the developing world using microneedle-delivered fluorescent microparticles." *42nd Society for Biomaterials Annual Meeting and Exposition 2019: The Pinnacle of Biomaterials Innovation and Excellence*. Society for Biomaterials, 2019.
61. Tan, Hiangkiat, et al. "Impact of adherence to disease-modifying therapies on clinical and economic outcomes among patients with multiple sclerosis." Advances in therapy 28.1 (2011): 51-61.
62. Osterberg, Lars, and Terrence Blaschke. "Adherence to medication." New England journal of medicine 353.5 (2005): 487-497.
63. Puts, M. T. E., et al. "Factors influencing adherence to cancer treatment in older adults with cancer: a systematic review." Annals of Oncology 25.3 (2014): 564-577.

64. Hobson, Julia, et al. "Acute inflammation induced by the biopsy of mouse mammary tumors promotes the development of metastasis." Breast cancer research and treatment 139.2 (2013): 391-401.
65. Hansen, Nora M., et al. "Manipulation of the primary breast tumor and the incidence of sentinel node metastases from invasive breast cancer." Archives of surgery 139.6 (2004): 634-640.
66. Estourgie, S. H., O. E. Nieweg, and B. B. R. Kroon. "High incidence of in-transit metastases after sentinel node biopsy in patients with melanoma." British journal of surgery 91.10 (2004): 1370-1371.
67. Gu, Bing, et al. "Seeing is believing, PLGA microsphere degradation revealed in PLGA microsphere/PVA hydrogel composites." Journal of controlled release 228 (2016): 170-178.
68. Gasmi, H., et al. "Does PLGA microparticle swelling control drug release? New insight based on single particle swelling studies." Journal of Controlled Release 213 (2015): 120-127.
69. Fu, Karen, et al. "Visual evidence of acidic environment within degrading poly (lactic-co-glycolic acid)(PLGA) microspheres." Pharmaceutical research 17.1 (2000): 100-106.
70. Santini, John T., Michael J. Cima, and Robert Langer. "A controlled-release microchip." Nature 397.6717 (1999): 335-338.
71. Grayson, Amy C. Richards, et al. "Multi-pulse drug delivery from a resorbable polymeric microchip device." Nature materials 2.11 (2003): 767-772.
72. Yoshida, Ryo, et al. "Pulsatile drug delivery systems using hydrogels." Advanced drug delivery reviews 11.1-2 (1993): 85-108.
73. Tamada, J. A., and R. Langer. "Erosion kinetics of hydrolytically degradable polymers." Proceedings of the National Academy of Sciences 90.2 (1993): 552-556.
74. Fredenberg, Susanne, et al. "The mechanisms of drug release in poly (lactic-co-glycolic acid)-based drug delivery systems—a review." International journal of pharmaceutics 415.1-2 (2011): 34-52.
75. Versypt, Ashlee N. Ford, Daniel W. Pack, and Richard D. Braatz. "Mathematical modeling of drug delivery from autocatalytically degradable PLGA microspheres—A review." Journal of Controlled Release 165.1 (2013): 29-37.

76. Von Burkersroda, Friederike, Luise Schedl, and Achim Göpferich. "Why degradable polymers undergo surface erosion or bulk erosion." Biomaterials 23.21 (2002): 4221-4231.
77. Mylonaki, Ioanna, et al. "Imaging the porous structure in the core of degrading PLGA microparticles: the effect of molecular weight." Journal of controlled release 286 (2018): 231-239.
78. Zhu, Xiaoxiang, and Richard D. Braatz. "A mechanistic model for drug release in PLGA biodegradable stent coatings coupled with polymer degradation and erosion." Journal of Biomedical Materials Research Part A 103.7 (2015): 2269-2279.
79. Ding, Amy G., and Steven P. Schwendeman. "Acidic microclimate pH distribution in PLGA microspheres monitored by confocal laser scanning microscopy." Pharmaceutical research 25.9 (2008): 2041-2052.
80. Washington, Michael A., et al. "Monomer sequence in PLGA microparticles: Effects on acidic microclimates and in vivo inflammatory response." Acta biomaterialia 65 (2018): 259-271.
81. Ruan, Gang, Si-Shen Feng, and Qiu-Tian Li. "Effects of material hydrophobicity on physical properties of polymeric microspheres formed by double emulsion process." Journal of controlled release 84.3 (2002): 151-160.
82. Sadeghi, Ilin, Hyunmin Yi, and Ayse Asatekin. "A method for manufacturing membranes with ultrathin hydrogel selective layers for protein purification: Interfacially Initiated Free Radical Polymerization (IIFRP)." Chemistry of Materials 30.4 (2018): 1265-1276.
83. Khalkhali, Abolfazl, Morteza Sarmadi, and Ehsan Sarikhani. "Investigation on the best process criteria for lap joint friction stir welding of AA1100 aluminum alloy via Taguchi technique and ANOVA." Proceedings of the Institution of Mechanical Engineers, Part E: Journal of Process Mechanical Engineering 231.2 (2017): 329-342.
84. Prausnitz, Mark R. "Microneedles for transdermal drug delivery." *Advanced drug delivery reviews* 56.5 (2004): 581-587.
85. Kim, Yeu-Chun, Jung-Hwan Park, and Mark R. Prausnitz. "Microneedles for drug and vaccine delivery." *Advanced drug delivery reviews* 64.14 (2012): 1547-1568.
86. Ita, Kevin. "Dissolving microneedles for transdermal drug delivery: Advances and challenges." *Biomedicine & Pharmacotherapy* 93 (2017): 1116-1127.

87. Park, Jung-Hwan, Mark G. Allen, and Mark R. Prausnitz. "Biodegradable polymer microneedles: fabrication, mechanics and transdermal drug delivery." Journal of controlled release 104.1 (2005): 51-66.
88. Loizidou, Eriketi Z., et al. "Structural characterisation and transdermal delivery studies on sugar microneedles: Experimental and finite element modelling analyses." European Journal of Pharmaceutics and Biopharmaceutics 89 (2015): 224-231.
89. Rad, Zahra Faraji, et al. "High-fidelity replication of thermoplastic microneedles with open microfluidic channels." Microsystems & nanoengineering 3.1 (2017): 1-11.
90. Sarmadi, M., et al. "Multi-objective Optimization of Microneedle Design for Transdermal Drug Delivery." *Stress* 10 (2019): 15.
91. Gill, Harvinder S., et al. "Effect of microneedle design on pain in human subjects." The Clinical journal of pain 24.7 (2008): 585
92. Alam, Murad, et al. "Effect of needle size on pain perception in patients treated with botulinum toxin type A injections: a randomized clinical trial." JAMA dermatology 151.11 (2015): 1194-1199.
93. Gill, Harvinder S., and Mark R. Prausnitz. "Does needle size matter?." Journal of diabetes science and technology 1.5 (2007): 725-729.
94. Arendt-Nielsen, Lars, Henrik Egekvist, and Peter Bjerring. "Pain following controlled cutaneous insertion of needles with different diameters." Somatosensory & motor research 23.1-2 (2006): 37-43.
95. Raina, Rajat, et al. "Self-taught learning: transfer learning from unlabeled data." Proceedings of the 24th international conference on Machine learning. ACM, 2007.
96. Quattoni, Ariadna, Michael Collins, and Trevor Darrell. "Transfer learning for image classification with sparse prototype representations." Computer Vision and Pattern Recognition, 2008. CVPR 2008. IEEE Conference on. IEEE, 2008
97. Krizhevsky, Alex, Ilya Sutskever, and Geoffrey E. Hinton. "Imagenet classification with deep convolutional neural networks." Advances in neural information processing systems. 2012.
98. Nkanga, Christian Isalomboto, et al. "Clinically established biodegradable long acting injectables: An industry perspective." *Advanced drug delivery reviews* (2020).

99. Kashkooli, Farshad Moradi, et al. "Nexus between in silico and in vivo models to enhance clinical translation of nanomedicine." *Nano Today* 36 (2021): 101057.
100. Bhujel, Ripesh, et al. "Practical quality attributes of polymeric microparticles with current understanding and future perspectives." *Journal of Drug Delivery Science and Technology* (2021): 102608.
101. Perry, Jillian L., et al. "PRINT: a novel platform toward shape and size specific nanoparticle theranostics." *Accounts of chemical research* 44.10 (2011): 990-998.